Electromagnetic Properties of Low-Latitude Plasma Irregularities

A Dissertation

Presented to the Faculty of the Graduate School

of Cornell University

in Partial Fulfillment of the Requirements for the Degree of

Doctor of Philosophy

by

Eugene Vinh Dao

August 2013

Electromagnetic Properties of Low-Latitude Plasma Irregularities

Eugene Vinh Dao, Ph.D.

Cornell University 2013

We derive and employ an algorithm for the three-dimensional fluid treatment of ionospheric plasma, including the complete set of electromagnetic fields. Explored are the three-dimensional electric and magnetic fields resulting from current divergence, current flows, and Alfvén waves associated with low-latitude plasma irregularity dynamics. We investigate both dynamic and static electromagnetic properties. Simulated are the Alfvénic dynamics generated by low-latitude plasma depletions that map electric fields along Earth's magnetic field lines. The time scales of Alfvénic dynamics to settle into an approximately electrostatic state is on the order of seconds to tens of seconds. Presented are the electrostatic three-dimensional electromagnetic characteristics of the gravitational Rayleigh-Taylor mode. Current divergence resulting from plasma depletions generate a current circulation from the bubble to the E region where transverse conductivity is the greatest. Despite high parallel conductivities along Earth's magnetic field lines, we show that magnetic field lines are not exactly equipotential as often approximated. Simulated diamagnetic currents associated with plasma bubbles produce significant perturbation magnetic field parallel to Earth's magnetic field consistent with *Stolle et al.* (2006). We find that three dimensional ambipolar electric fields are overestimated by one-dimensional theory. The gravitational Rayleigh-Taylor produces zonal polarization electric fields, while zonal winds can add additional meridional electric fields, resulting in a tilted fields. Observed tilted electromagnetic signatures in nature suggests a prevalence of neutral wind influence on low-latitude plasma irregularities. Given a zonal drift, perturbations of certain zonal wavelength can have polarization electric fields resonate due to Alfvén resonance. A bubble upwelling at supersonic speeds is simulated. The bubble developed strong negative and positive meridional magnetic fields on the northern and southern edge, respectively, on the order of 100 nT.

Biographical Sketch

Eugene Vinh Dao was born in Ypsilanti, Michigan on September 7, 1986. He attended Acton-Boxborough Regional High School in Acton, Massachusetts, and graduated in 2005. He then attended Cornell University where he received a Bachelors of Science in Electrical and Computer Engineering in 2009. He then continued to study at Cornell University to study space plasma physics. In 2013, he received a Doctor of Philosophy in Electrical Engineering from Cornell University.

Dedicated to my parents, Phan and Bachyen, who have always supported me.

Acknowledgments

First and foremost, I thank Professor Michael C. Kelley for the invaluable guidance and advice starting from when I was an undergraduate and throughout my graduate studies. Mike introduced me to space physics and the space physics community for which I am grateful. I want to thank Professor Charles E. Seyler for his deep insight in plasma physics and mathematics, which was integral to the development of the numerical model presented in this dissertation. I want to thank Professor David L. Hysell for his advice and for sharing his insight in Aeronomy. Dave is always open to discuss research. I thank Dr. Wesley E. Swartz for taking me under his wing and giving me the opportunity to assist him in teaching. I would like to thank the Air Force Research Lab for supporting my research and integrating me into the space physics community. More specifically, I thank Odile de La Beaujardiere for accepting me as a lab member, giving guidance, and introducing me to as many members of our scientific community whenever the chance presents itself. I want to thank Yi-Jiun Su for her support and guidance in my research endeavors. I want to thank John Retterer, who is always open for collaboration and sharing his expertise. I would like to thank Robert Pfaff, who is always eager to share data and ideas for research topics. I thank Bill Burke Bill Burke for enlightening discussions throughout the course of this research endeavor. I cannot express enough thanks to Laurie Shelton, who kept everything in order for me and always found ways to improve my writing. Part of the analysis was supported in part by NASA grants NNH09AK05I and NNH09AM20I to the Air Force Research Laboratory. Work at Cornell was funded in part by the Office of Naval Research under grant N00014-09-1-0975 and by OSD's Science, Mathematics, and Research Transformation (SMART) Program under grant N002440910081.

Contents

List of Figures

Nomenclature

ϵ_0	permittivity of free space
μ_0	permeability of free space
ν_{ie}, ν_{in}	ion-(electron, neutral) collision frequency
ν_i	total ion collision frequency ($\nu_{ie} + \nu_{in}$)
ν_{ei}, ν_{en}	electron-(ion, neutral) collision frequency
ν_e	total electron collision frequency ($\nu_{ei} + \nu_{en}$)
$\perp$, $\parallel$	denotes (perpendicular, parallel) components to the total magnetic field
$\mathbf{B}$, $\mathbf{B}_0$, $\mathbf{B}_1$	(total, background, perturbation) magnetic field vector
B_0	magnitude of Earth's magnetic field
c	speed of light
e	electron charge
$\mathbf{E}$, $\mathbf{E}_0$, $\mathbf{E}_1$	(total, background, perturbation) electric field vector
$\mathbf{g}$	Earth's gravity vector
$\mathbf{J}$, $\mathbf{J}_1$	(total, perturbation) current density vector
k_b	Boltzmann constant
M, m	(ion, electron) mass
n_i, n_e	(ion, electron) density
p_i, p_e	(ion, electron) pressure
$\mathbf{v}_i$, $\mathbf{v}_e$, $\mathbf{v}_n$	(ion, electron, neutral) velocity vector

Chapter 1

Introduction

On the bottomside of the F region, the equatorial ionosphere is unstable at night due to sharp post-sunset bottomside gradients when photoionization ceases and recombination sharpens the density gradient below the F layer. These sharp bottomside gradients are conducive to plasma instabilities (*Dungey*, 1956; *Balsley et al.*, 1972; *Haerendel*, 1973; *Sultan*, 1996) that take the form of plasma density structures (often referred to as spread F, plasma irregularities, or plasma bubbles) in an otherwise smooth and uniform layer of plasma around the Earth. These equatorial irregularities have been observed regularly with satellites such as the Communications/Navigation Outage Forecasting System (C/NOFS) (*Dao et al.*, 2011). Such irregularities can disrupt satellite-to-ground communication and navigation systems such as the global positioning system (GPS). Observing, identifying, and understanding the physics behind these plasma irregularities are essential to forecasting satellite-to-ground outages.

In past studies, several satellites observed these plasma irregularities, such as the Atmosphere Explorer (see *Hanson and Sanatani*, 1973; *McClure et al.*, 1977; *Tsunoda et al.*, 1982), Defense Meteorological Satellite Program (DMSP), Challenging Minisatellite Payload (CHAMP) (*Reigber et al.*, 2002), and C/NOFS (*de La Beaujardiere et al.*, 2004) satellites. Associated with these plasma

irregularities are perturbations in electric and magnetic fields. These fields result from current systems associated with the the irregularities' growth driven by gravity, dynamo electric fields and global wind systems. The electromagnetic signatures of these current systems not only can identify plasma irregularities, but can also give insight to underlying physics.

In Figure 1.1, presented are ion density measurements spanning $\sim$ 700 km at low-latitudes as measured in situ by C/NOFS' Planar Langmuir Probe (PLP) instrument. Raw ion density measurements (black line) and estimated ambient ion density (red line) are presented on the first panel on a log scale. We take interest in the smaller scale fluctuations ($<$ 100 km) that deviate from the ambient density n_0. The absolute difference between the ambient density and the raw measurements ($\Delta n_i = n_i - n_0$) is presented in the second panel. To better represent all the small fluctuations as seen on the top panel's log scale, the ion depletion is often normalized by the ambient density ($\Delta n_i / n_{i0}$), which is plotted on the third panel. The solar local time (solid-line) and altitude (dotted-line) are plotted on the fourth panel. Significant small scale density irregularities are observed during the local nighttime for this particular orbit.

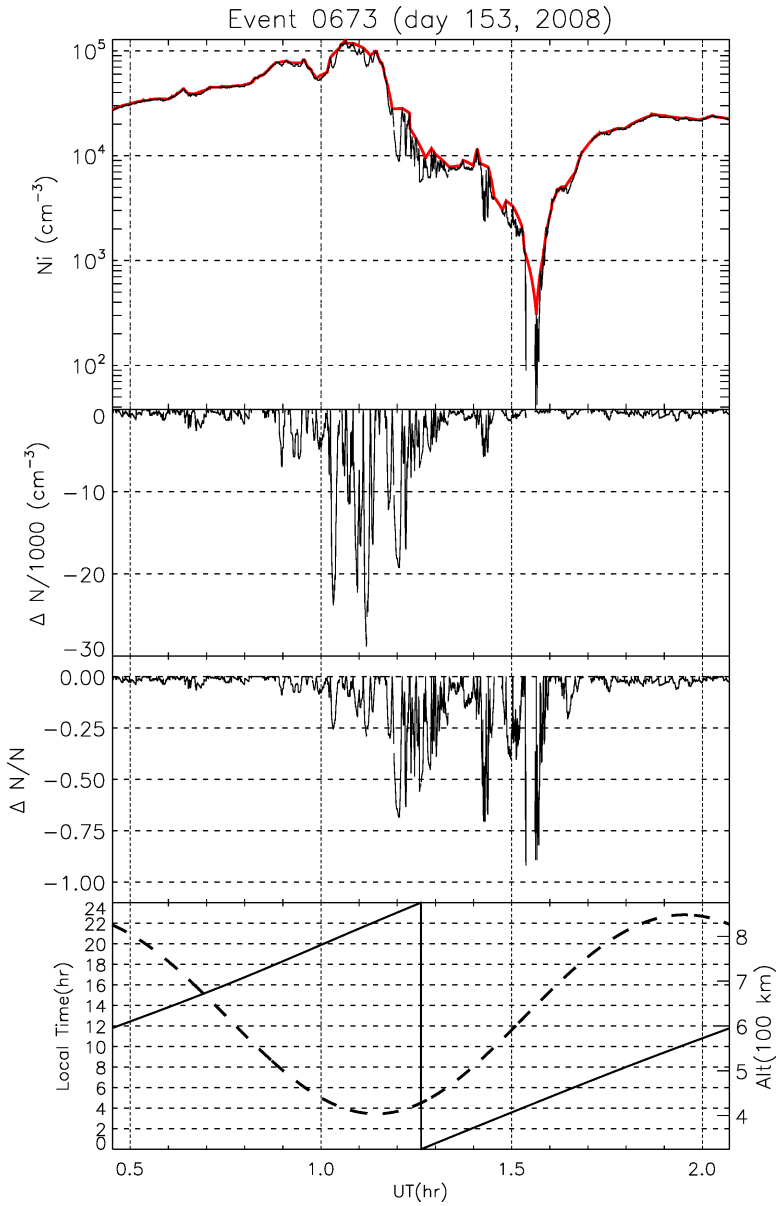

Figure 1.1: C/NOFS observation of plasma irregularities on the nighttime side of the Earth.

Associated with these plasma irregularities are electric field signatures such as those observed globally at low-latitudes by *Rodrigues et al.* (2009), *Huang et al.* (2010), and *Yokoyama et al.* (2011). In Figure 1.2, $\Delta n_i/n_{i0}$ density fluctuations (in black) and electric field fluctuations (in

red) are presented. Here, $\Delta n_i/n_{i0}$ is measured by C/NOFS' PLP and electric field fluctuations are measured by C/NOFS' Vector Electric Field Instrument (VEFI) on June 3rd, 2008. ΔE_{zon} refers to electric field fluctuations perpendicular to the Earth's magnetic field ($\mathbf{B}_0$) in the zonal (magnetic east) direction. ΔE_{mer} refers to electric field fluctuations in the meridional direction (zonal cross $\mathbf{B}_0$ direction which is vertical at the magnetic equator). Superimposed on the electric field fluctuations (red) is $\Delta n_i/n_{i0}$ (black), showing the correspondence of electric field fluctuations with plasma density fluctuations. These electric field fluctuations are often interpreted as polarization electric fields that result from plasma irregularities.

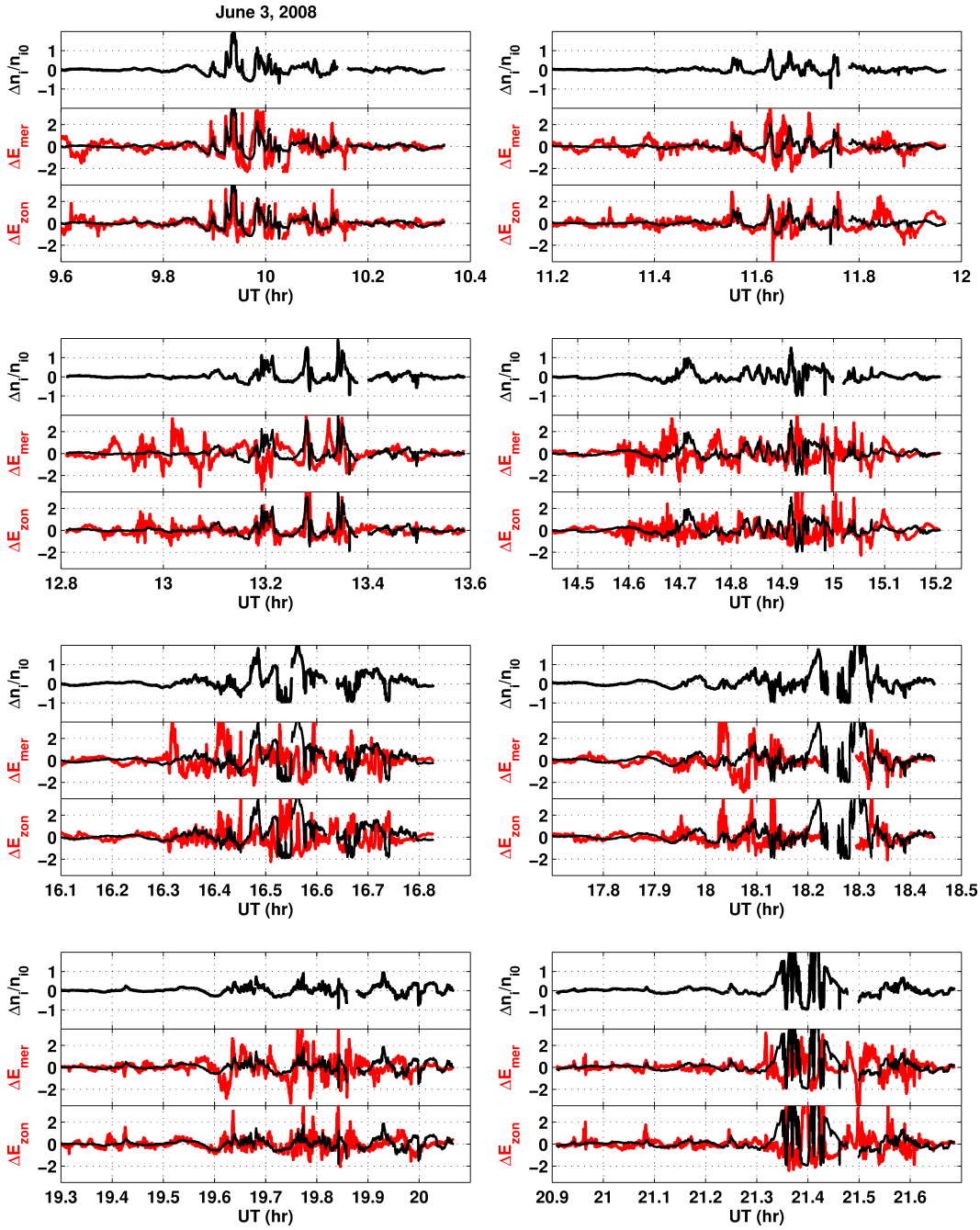

Figure 1.2: Plasma irregularities (normalized units) and associated electric field fluctuations (mV/m). In black are plasma density fluctuations and in red are electric field fluctuations signature to the plasma density fluctuations.

Until recently, experimental work has focused on by the plasma density, electric field, and plasma velocity measurements made possible by rocket, satellite and ground-based radar and radio-wave measurement techniques developed in the period between 1950-2000. However, in more recent times, magnetic field measurements have been developed to the point that very small low-latitude magnetic fields can be reliably detected (e.g. *Lühr et al.*, 2003; *Stolle et al.*, 2006). Upper atmosphere magnetic measurements have been made for decades, of course, even before electric field instruments were developed, but were designed for auroral zone and polar cap current systems. The associated magnetic field perturbations are several orders of magnitude larger than near the equator (except for the equatorial electrojet which is well below the F-Region of interest here). Development of sensitive magnetic field measurements was made jointly with scientists interested in microscale anomalies in the crustal magnetic field. These measurements have inspired the theoretical developments described here.

In Figure 1.3, plasma density and AC magnetic field measurements made by the CHAMP satellite are presented. These examples were first presented in *Stolle et al.* (2006). For each day, the two large increase in density in the top panels at around -15 and 15 degrees magnetic latitude are ambient density enhancements known as the Appleton anomalies. The smaller scale structures in magnetic field are apparently associated with plasma fluctuations. *Stolle et al.* (2006) attributed magnetic perturbations parallel to Earth's magnetic field to diamagnetic currents flowing along the walls of the plasma bubbles. However, questions of what resulted in magnetic perturbations perpendicular to Earth's magnetic field remained. It was postulated that perpendicular perturbations in magnetic field result from Alfvén wave generators inside ion density bubbles that carry field-aligned currents, an idea earlier described by *Bhattacharyya and Burke* (2000). *Bhattacharyya and Burke* (2000) described how plasma density bubbles at the magnetic equator generate Alfvén waves that propagate poleward, resulting in poleward Poynting fluxes. *Stolle et al.* (2006) did not reach a definitive conclusion about the observed perpendicular magnetic field perturbations because, at times, the

Poynting fluxes pointed towards the supposed wave generator at the equator, contrary to what *Bhattacharyya and Burke* (2000) described.

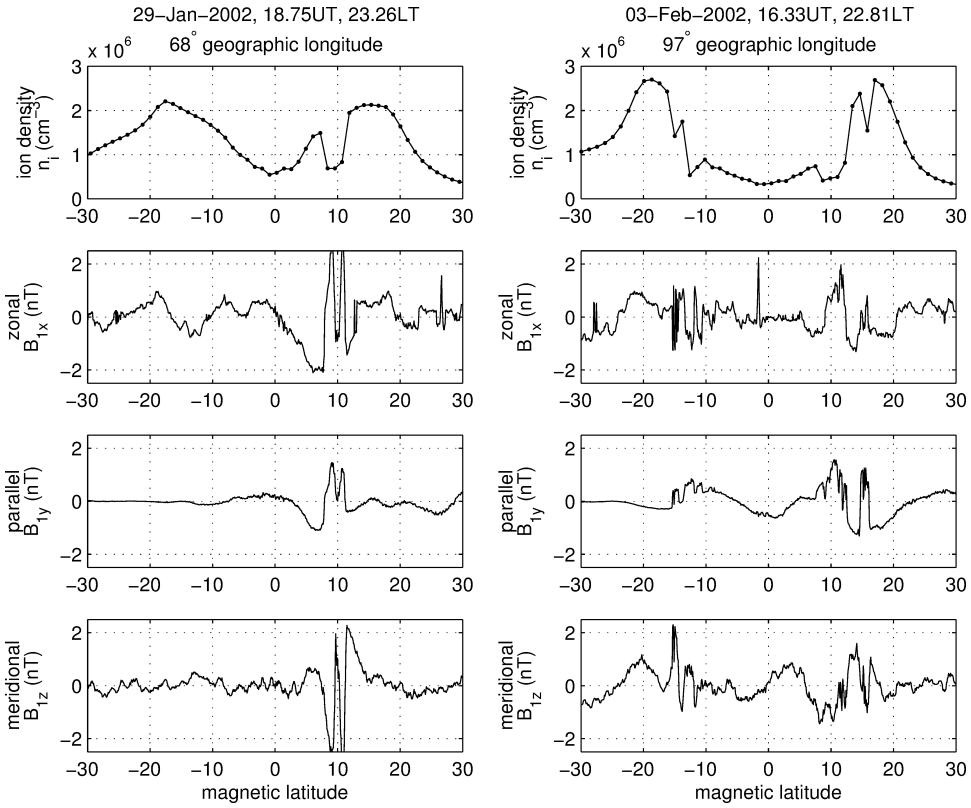

Figure 1.3: The ion density, and vector magnetic field measured along CHAMP satellite passes through the ionosphere at low-latitudes. Adapted from *Stolle et al.* (2006).

Prior to these sensitive magnetic field data, one example of a very large magnetic perturbation was observed in the equatorial F region (*Aggson et al.*, 1992) using conventional instrumentation. *Aggson et al.* (1992) were among the first to observe evidence of perpendicular magnetic field perturbations associated with equatorial plasma irregularities. They observed magnetic field intensity of 150 nano-Tesla (nT) at the edge of a strongly upwelling plasma depletion drifting vertically at supersonic speeds of $\sim$ 2 km/s. The magnetic field signatures were interpreted as propagating Alfvén waves. Alfvénic characteristics of equatorial bubbles have been more recently discussed in

Bhattacharyya and Burke (2000), *Basu* (2005), and *Burke et al.* (2012).

While there is a large variety of techniques to observe the electromagnetic signatures of plasma irregularities, there is an inherent limitation to observing and interpreting these signatures. Plasma bubbles are large three-dimensional (3-D) phenomena that can span hundreds of kilometers. Due to a limited field of view, neither satellites nor radars can determine the electromagnetic characteristics of a whole plasma bubble at a given time. Not only are plasma bubbles large, their current systems couple to the E region at higher latitudes. However, in this dissertation, a numerical three-dimensional electromagnetic model of equatorial plasma bubbles is developed to investigate and explore the electromagnetic characteristics of whole bubble systems (including coupling with the E region). We will refer to this model as the Electro-Magnetic Ionosphere (EMI) model for its ability to model electromagnetic physics in the ionosphere. For many decades and with good reason, theoretical emphasis has been directed to the electrostatic nature of the plasma instabilities associated with these irregularities. While there are several recent advances in low-latitude ionospheric numerical modeling (see *Huba et al.*, 2000, 2008; *Retterer*, 2005, 2010; *Aveiro and Hysell*, 2010), these models typically assume electrostatic conditions, where electric fields are irrotational ($\nabla \times \mathbf{E} = 0$, where $\mathbf{E}$ is the vector electric field) and can be completely described using scalar potential, Φ, such that $\mathbf{E} = -\nabla\Phi$. With potential solvers, these models determine a solution for Φ such that currents are divergent free ($\nabla \cdot \mathbf{J} = 0$, where $\mathbf{J}$ is the vector current density). While these models provide great insight into the development of low-latitude plasma irregularities, they do not resolve dynamic electromagnetic processes. Electric field associated with electromagnetic waves (such as Alfvén waves discussed earlier) are rotational and thus cannot be fully described using a scalar potential. For a more complete set of electromagnetic signatures, EMI is developed to include dynamic electromagnetic physics in addition to electrostatic physics. A thorough description of EMI is presented in Chapters 3 and 4. Inclusion of electrodynamics will allow for the investigation of the processes that relay information throughout the system of a plasma irregularity.

The goal of this dissertation is to derive a model and numerically simulate the full set of electromagnetic fields (electrostatic and electrodynamic) associated with low-latitude plasma irregularities and investigate the electromagnetic characteristics of low-latitude plasma irregularities. The phenomena responsible for the observed perturbed electric and magnetic field signatures associated with low-latitude plasma irregularities will be interrogated. In Chapter 7, Alfvén waves that carry information through the system of the Rayleigh-Taylor mode (as theorized in *Bhattacharyya and Burke*, 2000, *Basu*, 2005) are analyzed. In Chapter 8, electrostatic electromagnetic fields associated low-latitude bubbles are explored. More specifically, the electromagnetic fields for the electrostatic gravitational Rayleigh-Taylor, diamagnetic, ambipolar, and wind-driven current circulations are analyzed. In Chapter 9, we explore Alfvén resonance in the context of low-latitude plasma irregularities that electrostatic theory cannot describe. In Chapter 10, a supersonic bubble similar to that observed by *Aggson et al.* (1992) is simulated.

Chapter 2

Background

2.1 General plasma equations

Before discussing the electromagnetic theory associated with plasma irregularities, we must first establish the fundamental equations that describe the physics of plasmas in the ionosphere. First, the motion of ions and electrons can be described by the ion momentum, and electron momentum equations,

$$\frac{d\mathbf{v}_i}{dt} = \frac{e}{M}\left(\mathbf{E} + \mathbf{v}_i \times \mathbf{B}\right) + \mathbf{g} - \frac{\nabla p_i}{n_i M} - \nu_{in}\left(\mathbf{v}_i - \mathbf{v}_n\right) - \nu_{ie}\left(\mathbf{v}_i - \mathbf{v}_e\right) \tag{2.1}$$

$$\frac{d\mathbf{v}_e}{dt} = -\frac{e}{m}\left(\mathbf{E} + \mathbf{v}_e \times \mathbf{B}\right) + \mathbf{g} - \frac{\nabla p_e}{n_e m} - \nu_{en}\left(\mathbf{v}_e - \mathbf{v}_n\right) - \nu_{ei}\left(\mathbf{v}_e - \mathbf{v}_i\right), \tag{2.2}$$

where $\mathbf{v}_i$ is the ion velocity, $\mathbf{v}_e$ is the electron velocity, d/dt is the advective derivative ($\partial_t + \mathbf{v}_i \cdot \nabla$ for ions and $\partial_t + \mathbf{v}_e \cdot \nabla$ for electrons where ∂_t is the partial time-derivative), e is the elementary positive charge, M is the ion mass, m is the electron mass, $\mathbf{E}$ is the electric field vector, $\mathbf{B}$ is the magnetic field vector, $\mathbf{g}$ is the gravitational acceleration vector, p_i is the ion pressure, p_e is the electron pressure, ν_{ie} is the ion-electron collision frequency, ν_{in} is the ion-neutral collision frequency, ν_{ei} is the electron-ion collision frequency, and ν_{en} is the electron-neutral collision frequency. Here,

we deal with single ion species for simplicity. The conservation of ions is expressed by the plasma continuity equation,

$$\partial_t n_i = -\nabla \cdot (n_i \mathbf{v}_i)\,, \tag{2.3}$$

where n_i is ion density and we neglect ion production and loss. The density of electrons, n_e, can be solved for by considering the quasi-neutrality of plasmas,

$$n_e \simeq n_i, \tag{2.4}$$

for single species singly charged ions. Throughout this dissertation, we deal only with singly charged ions (O^+, H^+, He^+, O_2^+, NO^+). Hence, n_e and n_i are interchangeable throughout. The electromagnetism of plasmas are dictated by Maxwell's equations,

$$\nabla \cdot \mathbf{B} = 0 \tag{2.5}$$

$$\nabla \cdot \mathbf{E} = \frac{e}{\epsilon_0}\,(n_{i-} n_e) \tag{2.6}$$

$$\partial_t \mathbf{B} = -\nabla \times \mathbf{E} \tag{2.7}$$

$$\partial_t \mathbf{E} = c^2\,(\nabla \times \mathbf{B} - \mu_0 \mathbf{J})\,, \tag{2.8}$$

where ϵ_0 is the permittivity of free space, μ_0 is the permeability of free space, and $\mathbf{J}$ is the current density, defined as

$$\mathbf{J} = e n_e (\mathbf{v}_i - \mathbf{v}_e). \tag{2.9}$$

We can write $\mathbf{J}$, first solving equations (2.1) for $\mathbf{v}_i$ and (2.2) for $\mathbf{v}_e$,

$$\mathbf{v}_i = \tilde{\mathbf{A}}_i \cdot \left[\frac{e}{M}\mathbf{E} + \mathbf{g} - \frac{\nabla p_i}{n_i M} + \nu_{in}\mathbf{v}_n + \nu_{ie}\mathbf{v}_e - \frac{d\mathbf{v}_i}{dt}\right] \tag{2.10}$$

$$\mathbf{v}_e = \tilde{\mathbf{A}}_e \cdot \left[-\frac{e}{m}\mathbf{E} + \mathbf{g} - \frac{\nabla p_e}{n_e m} + \nu_{en}\mathbf{v}_n + \nu_{ei}\mathbf{v}_i - \frac{d\mathbf{v}_e}{dt}\right], \tag{2.11}$$

where $\tilde{\mathbf{A}}_i$ and $\tilde{\mathbf{A}}_e$ are tensors, defined as

$$\tilde{\mathbf{A}}_{(\sigma=i,e)} = \begin{bmatrix} \nu_\sigma & -\Omega_{\sigma z} & \Omega_{\sigma y} \\ \Omega_{\sigma z} & \nu_\sigma & -\Omega_{\sigma x} \\ -\Omega_{\sigma y} & \Omega_{\sigma x} & \nu_\sigma \end{bmatrix}^{-1}, \tag{2.12}$$

where $\nu_i = \nu_{in} + \nu_{ie}$, $\nu_e = \nu_{en} + \nu_{ei}$, and gyrofrequency components are defined as

$$\begin{bmatrix} \Omega_{ix} \\ \Omega_{iy} \\ \Omega_{iz} \end{bmatrix} \equiv \frac{e\mathbf{B}}{M}, \begin{bmatrix} \Omega_{ex} \\ \Omega_{ey} \\ \Omega_{ez} \end{bmatrix} \equiv -\frac{e\mathbf{B}}{m}. \tag{2.13}$$

Taking the difference of equation (2.10) and (2.11) and multiplying the difference by en_e yields

$$\mathbf{J} = \tilde{\boldsymbol{\sigma}}\mathbf{E} + en_e\tilde{\mathbf{A}}_i\left(\mathbf{g} - \frac{\nabla p_i}{n_i M} + \nu_{in}\mathbf{v}_n + \nu_{ie}\mathbf{v}_e - \frac{d\mathbf{v}_i}{dt}\right) - en_e\tilde{\mathbf{A}}_e\left(\mathbf{g} - \frac{\nabla p_e}{n_e m} + \nu_{en}\mathbf{v}_n + \nu_{ei}\mathbf{v}_i - \frac{d\mathbf{v}_e}{dt}\right), \tag{2.14}$$

where $\tilde{\boldsymbol{\sigma}}$ is the conductivity tensor such that

$$\begin{aligned} \tilde{\boldsymbol{\sigma}} &= \begin{bmatrix} \sigma_p & 0 & \sigma_h \\ 0 & \sigma_0 & 0 \\ -\sigma_h & 0 & \sigma_p \end{bmatrix} \\ \sigma_0 &= e^2 n_e\left(\frac{1}{m\nu_e} + \frac{1}{M\nu_i}\right) \\ \sigma_p &= e^2 n_e\left(\frac{\nu_e}{m\left(\nu_e^2 + \Omega_e^2\right)} + \frac{\nu_i}{M\left(\nu_i^2 + \Omega_i^2\right)}\right) \\ \sigma_h &= e^2 n_e\left(\frac{|\Omega_e|}{m\left(\nu_e^2 + \Omega_e^2\right)} - \frac{\Omega_i}{M\left(\nu_i^2 + \Omega_i^2\right)}\right), \end{aligned} \tag{2.15}$$

for a coordinate system where $\hat{\mathbf{y}}$ is parallel to $\mathbf{B}$. The conductivities σ_0, σ_p and σ_h are commonly referred to as the parallel, Pedersen, and Hall conductivities, respectively. Typical values for these conductivities are shown below (from *Kelley*, 2009).

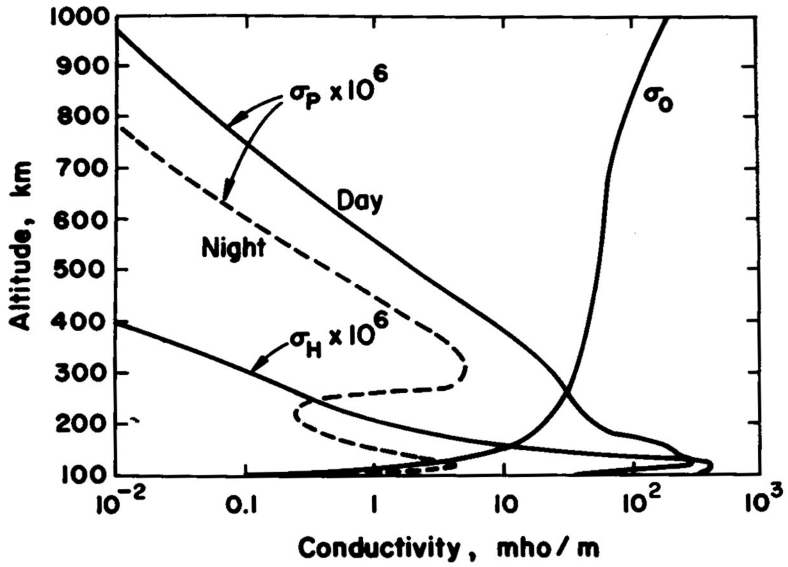

Figure 2.1: Typical parallel, Pedersen, and Hall conductivities in ionosphere (*Kelley*, 2009).

In the electrostatic regime, an important relation is that the current converges to zero divergence,

$$\nabla \cdot \mathbf{J} = 0. \tag{2.16}$$

This is derived from taking the divergence of equation Ampere's law (2.8) after setting the time derivative (which is electrodynamic) to zero.

2.2 Classic linear theory of the gravitational Rayleigh-Taylor mode

The gravitational Rayleigh-Taylor instability is classically simplified by making several approximations. Firstly, the problem is made one-dimensional (1-D) by neglecting any physics in the parallel

or meridional direction and only consider currents that flow in the x-direction (zonal). There are serious implications when making this simplification. However, the 1-D approximation is much easier to analytically solve than the three-dimensional (3-D) problem. We further simplify the analysis by neglecting pressure forces (cold plasma analysis), neglecting a background electric field $\mathbf{E}_0$, and neglecting neutral winds, $\mathbf{v}_n$. Their effects will be discussed later. Furthermore, restricting our analysis to the F region where plasmas are weakly collisional, we neglect electron collisional terms. With all of these simplifications, the current density (2.14) reduces to

$$\mathbf{J} = \left(\sigma_p E_{x1} + \frac{n_i M g}{B}\right) \hat{\mathbf{x}}. \tag{2.17}$$

By equation (2.16), $\nabla \cdot \mathbf{J} = 0$, the current must be divergent free. Hence,

$$\partial_x \left(\sigma_p E_x\right) = -\partial_x \left(\frac{n_i M g}{B}\right). \tag{2.18}$$

Let us break $\mathbf{E}$ into a sum of a background electric field, $\mathbf{E}_0$, plus a perturbation value, $\mathbf{E}_1$, such that $\mathbf{E} = \mathbf{E}_0 + \mathbf{E}_1$. Likewise, let us break n_i into a sum of a background ion density, n_{i0}, plus a perturbation value, n_{i1}, such that $n_i = n_{i0} + n_{i1}$. We treat background values $\mathbf{E}_0$ and n_{i0} as constant in all spatial directions, where variations are represented by $\mathbf{E}_1$ and n_{i1}, respectively. Substituting $\mathbf{E}$ and n_i into equation (2.18) yields

$$\sigma_p \partial_x E_{x1} + E_{x1} \partial_x \sigma_p = -\frac{Mg}{B} \partial_x n_{i1}. \tag{2.19}$$

In the F region, where the plasma is weakly collisional ($\Omega_i^2 \gg \nu_i^2$, $\Omega_e \gg \nu_e$, and $\nu_e \sim 0$), the Pedersen conductivity, σ_p, from (2.15) can be expressed as

$$\sigma_p = \frac{M n_i \nu_{in}}{B^2}. \tag{2.20}$$

Thus, equation (2.19) can be rewritten as

$$\sigma_p \partial_x E_{x1} + \frac{\sigma_p}{n_i} E_{x1} \partial_x n_i = -\frac{Mg}{B} \partial_x n_i. \tag{2.21}$$

Assuming plane wave solutions, where $E_{x1} \propto n_{i1} \propto e^{i(\omega t - kx)}$ and where k is the zonal wave vector, equation (2.21) becomes

$$\frac{\sigma_p}{n_i} E_{x1} \left(n_i + n_{i1}\right) = -\frac{Mg}{B} n_{i1}. \tag{2.22}$$

Assuming $n_i \gg n_{i1}$, as part of this linear analysis, we solve for E_{x1} as

$$E_{x1} = -\frac{Mg}{\sigma_p B} n_{i1}, \tag{2.23}$$

where E_{x1} is the polarization electric field that develops due to a perturbation in ion density, n_{i1}. One can interpret this polarization field as a simple circuit presented in Figure 2.2. Given a gravity-driven current source across a plasma resistor, the voltage across that resistor is simply the current ($-Mgn_{i1}/B$) times the resistance or current divided by the conductance (σ_p). Such polarization electric fields are inherently signature of equatorial plasma irregularities. A density depletion will result in a zonal electric field.

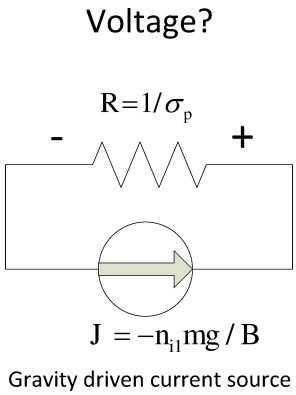

Figure 2.2: Polarization electric field circuit analogy diagram.

Not only are polarization electric fields signature of plasma irregularities, polarization electric fields impose forces on plasma irregularities that are key to the Rayleigh-Taylor instability. The drift velocity due to gravity and an electric field can be calculated from equation (2.10) in the weakly collisional limit, $\Omega_i^2 \gg \nu_i^2$, resulting in the following drift velocity

$$\mathbf{v}_i = \overbrace{\frac{M\mathbf{g}\times\mathbf{B}}{eB^2}}^{\text{gravity}} + \overbrace{\frac{\mathbf{E}\times\mathbf{B}}{B^2}}^{\text{electric field}}, \tag{2.24}$$

where the first term is the gravitational drift and the second term is the $\mathbf{E}\times\mathbf{B}$ drift. Substituting $\mathbf{E}$ with the polarization electric field (2.23) yields

$$\mathbf{v}_i = \frac{M\mathbf{g}\times\mathbf{B}}{eB^2} - \frac{gB}{\nu_{in}n_i}n_{i1}\hat{\mathbf{x}}\times\frac{\mathbf{B}}{B^2} = \frac{Mg}{eB}\hat{\mathbf{x}} - \frac{gn_{i1}}{\nu_{in}n_i}\hat{\mathbf{z}}, \tag{2.25}$$

where $\hat{\mathbf{x}}$ is in the magnetic zonal direction, $\hat{\mathbf{y}}$ is in the direction parallel to $\mathbf{B}$, and $\hat{\mathbf{z}}$ is meridional. In order to interrogate how these drifts affects the plasma density, we consider the continuity equation

$$\partial_t n_i = -\nabla\cdot(n_i\mathbf{v}_i). \tag{2.26}$$

In the F region, plasmas are approximately incompressible ($\nabla\cdot\mathbf{v}_\perp \simeq 0$). Thus we can simplify the continuity equation as

$$\partial_t n_i = -\mathbf{v}_i\cdot\nabla n_i = -v_{ix}\partial_x n_i - v_{iz}\partial_z n_i, \tag{2.27}$$

where ∂_x and ∂_z are the spatial partial derivatives in the x and z directions, respectively. The partial derivative in the parallel direction does not appear because $v_{iy} = 0$ in this 1-D analysis, but we must consider the vertical gradient in ion density, which is essential to the Rayleigh-Taylor

instability. Substituting v_{ix} and v_{iz} with (2.25) yields

$$\partial_t n_i = -\frac{Mg}{eB}\partial_x n_i + \frac{g n_{i1}}{\nu_{in} n_i}\partial_z n_i. \tag{2.28}$$

Now let us consider plane wave solution in the zonal direction assume where both n_{i1} and E_{x1} are proportional to $e^{i(\omega t - k_x x)}$, as illustrated below.

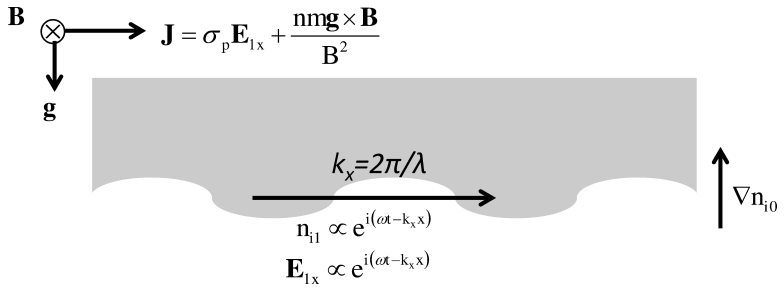

Figure 2.3: Diagram of Rayleigh Taylor instability.

Substituting n_i with the zonal plane wave solution into the continuity equation (2.28) yields

$$i\omega n_{i1} = ik_x \frac{Mg}{eB} n_{i1} + \frac{g n_{i1}}{\nu_{in} n_i}\partial_z n_{i0}$$

$$\omega n_i = k_x \frac{Mg}{eB} n_{i1} - i\frac{g n_{i1}}{\nu_{in} n_i}\partial_z n_{i0}$$

$$\omega = k_x \frac{Mg}{eB} - i\frac{g}{\nu_{in} n_i}\partial_z n_{i0} \tag{2.29}$$

Substituting ω back into the plane wave solution yields the description of how the density wave drifts and grows,

$$n_{i1} \propto e^{i(\omega t - k_x x)} = \left| e^{\frac{g}{\nu_{in} n_i}\partial_z n_{i0} t} \right| \cdot e^{ik_x\left(\frac{Mg}{eB}t - x\right)}. \tag{2.30}$$

This solution is a plane wave that moves in the x-direction at the velocity of the gravitational drift, with an amplitude that exponentially decays for $\partial_z n_i < 0$ and exponentially grows for $\partial_z n_i > 0$. On

the bottom-side of the F layer (where $\partial_z n_i > 0$) irregularities will grow. Because $\partial_z n_i$ is greatest at night when recombination decays the bottom of the F layer and sharpens the F layer's edge, these plasma irregularities are most violent at night. During the day, photoionization dominates bottom-side recombination and decreases both $\partial_z n_i$ and the irregularities' growth rate drastically. This is why equatorial plasma irregularities are typically nighttime phenomena.

2.3 Generalized classic Rayleigh-Taylor instability

In the previous section we described the gravitational Rayleigh-Taylor instability neglecting the background electric field and neutral winds. We will now generalize the classic Rayleigh-Taylor instability. Again, in the F region, the plasma is weakly collisional ($\Omega_i^2 \gg \nu_i^2$, $\Omega_e \gg \nu_e$, and $\nu_e \sim 0$). Neglecting ion momentum and the dimension parallel to $\mathbf{B}$, the cold plasma ($T_i = 0$ and $T_e = 0$) ion velocity equation (2.10) becomes

$$\mathbf{v}_i = \frac{1}{\Omega_i^2}\left[\nu_i\left(\frac{e}{M}\mathbf{E} + \mathbf{g} + \nu_{in}\mathbf{v}_n\right) + \Omega_i\left(\frac{e}{M}\mathbf{E} + \mathbf{g} + \nu_{in}\mathbf{v}_n\right) \times \frac{\mathbf{B}}{B}\right], \tag{2.31}$$

In the F region, electrons are highly magnetized ($\Omega_e \gg \nu_e$). Hence, neglecting the dimension parallel to $\mathbf{B}$, the cold plasma electron velocity equation (2.11) simplifies to

$$\mathbf{v}_e = \left(\frac{\mathbf{E}}{B} + \frac{m\mathbf{g}}{eB}\right) \times \frac{\mathbf{B}}{B}, \tag{2.32}$$

where we neglect electron-neutral collisions. Taking the difference of the ion and electron velocities and multiplying the difference by en_i yields

$$\mathbf{J} = \frac{en_i}{\Omega_i^2}\left[\nu_i\left(\frac{e}{M}\mathbf{E} + \mathbf{g} + \nu_{in}\mathbf{v}_n\right) + \Omega_i\left(\frac{e}{M}\mathbf{E} + \mathbf{g} + \nu_{in}\mathbf{v}_n\right) \times \frac{\mathbf{B}}{B}\right] - en_i\left(\frac{\mathbf{E}}{B} + \frac{m\mathbf{g}}{eB}\right) \times \frac{\mathbf{B}}{B} \tag{2.33}$$

The **E** cross **B** terms cancel and the electron gravitational term is negligible compared to the ion gravitational term, because $M \gg m$. Thus, the current density becomes

$$\mathbf{J} = \frac{en_i}{\Omega_i^2}\left[\nu_{in}\left(\frac{e}{M}\mathbf{E} + \mathbf{g} + \nu_{in}\mathbf{v}_n\right) + \Omega_i\left(\mathbf{g} + \nu_{in}\mathbf{v}_n\right) \times \frac{\mathbf{B}}{B}\right]$$

$$\begin{aligned}\mathbf{J} = &\frac{en_i}{\Omega_i^2}\left[\nu_{in}\left(\frac{e}{M}E_x + \nu_{in}v_{nx}\right) + \Omega_i\left(g_z - \nu_{in}v_{nz}\right)\right]\hat{\mathbf{x}} \\ &+ \frac{en_i}{\Omega_i^2}\left[\nu_i\left(\frac{e}{M}E_z - g_z + \nu_{in}v_{nz}\right) + \Omega_i\left(\nu_{in}v_{nx}\right)\right]\hat{\mathbf{z}}.\end{aligned} \tag{2.34}$$

By equation (2.16) the current must be divergent free, $\nabla \cdot \mathbf{J} = 0$. Hence, neglecting currents in the y and z directions in this 1-D analysis, $\partial_x J_x = 0$. Focusing our attention to J_x, the x components of equation (2.34) is

$$J_x = \frac{en_i}{\Omega_i^2}\left[\nu_{in}\left(\frac{e}{M}E_x + \nu_{in}v_{nx}\right) + \Omega_i\left(g_z - \nu_{in}v_{nz}\right)\right]. \tag{2.35}$$

Setting $\partial_x J_x = 0$ yields

$$\frac{e\partial_x n_i}{\Omega_i^2}\left[\nu_{in}\left(\frac{e}{M}E_x + \nu_{in}v_{nx}\right) + \Omega_i\left(g_z - \nu_{in}v_{nz}\right)\right] + \frac{e^2 n_i \nu_{in}}{M\Omega_i^2}\partial_x E_x = 0$$

$$e\partial_x n_i \Omega_i\left[g_z + \frac{\nu_{in}}{B}E_x - \nu_{in}v_{nz} + \frac{\nu_{in}^2}{\Omega_i}v_{nx}\right] + \frac{e^2 n_i \nu_{in}}{M}\partial_x E_x = 0. \tag{2.36}$$

Defining an effective gravity

$$g' \equiv g \cdot \cos\left(D\right) + \frac{\nu_{in}}{B}E_{x0} - \nu_{in}v_{nz} + \frac{\nu_{in}^2}{\Omega_i}v_{nx}, \tag{2.37}$$

where E_{x0} is the background zonal electric field and D is the dip angle (angle between $\mathbf{B}$ and the horizon), allows us to express the polarization electric field resulting from n_{i1} as

$$e\partial_x n_i \Omega_i g' + \frac{e^2 n_i \nu_{in}}{M} \partial_x E_x = 0$$

$$E_{x1} = -\frac{n_{i1}\Omega_i M g'}{e n_i \nu_i} = \frac{B^2}{M n_i \nu_{in}} \frac{M n_{i1} g'}{B} = -\frac{M g'}{\sigma_p B} n_{i1}, \tag{2.38}$$

where the Pedersen conductivity is defined by equation (2.20). Note the similarity to the polarization electric field in equation (2.23). The only difference is that g is replaced with the effective gravity, g', expressed by equation (2.37). The generalized Rayleigh-Taylor instability will operate in the same way as the simpler gravitational Rayleigh-Taylor instability, but with a different gravity. Similarly to equation (2.30), the wave solution with the effective gravity, g', becomes

$$n_{i1} \propto e^{i(\omega t - k_x x)} = \left| e^{\frac{g'}{\nu_{in} n_i} \partial_z n_{i0} t} \right| \cdot e^{i k_x \left(\frac{M g'}{eB} t - x \right)}, \tag{2.39}$$

a plane wave that moves in the x-direction at the speed of the effective gravitational drift speed, with an amplitude that exponentially decays or grows with the $\left| e^{\frac{g'}{\nu_{in} n_i} \partial_z n_{i0} t} \right|$ term.

2.4 Polarization electric field derived from field-line integrated quantities

The simplistic linear analysis of the Rayleigh-Taylor instability in Subsections 2.2 and 2.3 is a great stepping stone to understand the root of the plasma instabilities in the F region. However, it is a gross simplification. More realistically, parallel currents play an important role on how much polarization electric fields develop given a perturbation in ion density. Magnetic field lines are approximately equipotential and act like wires that can extend as far as the E region. The Pedersen conductivity, σ_p, is far greater in the E region than it is in the F region (refer to Figure 2.1). The F

region's connection to the E region's greater σ_p can significantly decrease the polarization electric field because currents have a path to lesser resistance. In turn, the weaker polarization electric field significantly reduces the Rayleigh-Taylor growth rate. In this section we attempt to derive the weaker polarization fields, approximating Earth's magnetic field lines as equipotential with field line integrated quantities similar to those found in *Perkins* (1973).

Combining the zonal current density equation (2.35) and the effective gravity (2.37), the zonal current density can be expressed as

$$J_x = \sigma_p E_{x1} + \frac{n_i M g'}{B}, \tag{2.40}$$

where E_{x1} is the zonal electric field perturbation, and the Pedersen conductivity is $\sigma_p = e^2 n_i \nu_{in}/M\Omega_i^2$ in this section. Here, we refer to x as being in the magnetic zonal direction, y as being parallel to the magnetic field, and z as being perpendicular to the magnetic field and in the meridional plane. The problem with (2.40) alone is that we must recognize that all of the points along a field line are approximately equipotential, as discussed earlier, and thus are effectively tied together. Every point along a field line has the same net zonal current as any other point on the line. Note that current observed at any specific point is not necessarily produced at that point locally. For instance, electric field-induced currents will flow through the paths of least resistance and not necessarily where the electric field is generated. Regardless of how electric fields map along magnetic field lines, most of the current will flow through where the Pedersen conductivity is greatest. A more comprehensive current equation must be formulated.

Take the circuit analogy of several current sources tied together in parallel. The output current of the parallel sources is the sum of all the sources. In our case, the current sources are driven by electric fields and effective gravity tied together in parallel (in a circuit sense) by magnetic field lines. The total zonal current driven by any of the two drivers is a field-line integral of its current contribution. Dividing this integral by the length of the line yields the effective zonal current

density. Using the electric field mapping for a dipole magnetic field (B.1), derived in the appendix, the effective zonal current driven by electric fields is formulated as

$$J'_{x\,E} = \frac{\int \frac{\sigma_p}{\cos^3\theta} dy}{\int dy}\, E_{x1}|_{\theta=0}\,, \tag{2.41}$$

where $E_{x1}|_{\theta=0}$ is the electric field perturbation at the magnetic equator, θ is the magnetic latitude, and the integration in the y direction is along the magnetic field line. Turning to the gravitational current contributions, we note that *Perkins* (1973) treats gravity currents as a varying value along the field line. However, similar to the formulation of Pedersen currents, gravity-driven currents are also tied together by magnetic field lines. The effective zonal currents should not differ from point to point along equipotential field lines. All points on a field line must be subjected to the same net zonal current, regardless of how much current is produced locally. Similar to the formulation of (2.41), we formulate the effective current density driven by gravity in equations (2.42), as a field-line integral divided by the length of the field line:

$$J'_{x\,gravity} = \frac{\int \frac{nMg'}{B} dy}{\int dy} \tag{2.42}$$

where one has to be careful that D, the dip angle, is embedded in g'. Combining the effective current densities yields

$$J'_x = \frac{\int \frac{\sigma_p}{\cos^3\theta} dy}{\int dy}\, E_{x1}|_{\theta=0} + \frac{\int \frac{n_i M g'}{B} dy}{\int dy}, \tag{2.43}$$

where the first and second terms are the effective current densities driven by electric field and gravity, respectively. The new current equation (2.43) is similar to the equation of the locally produced current (2.40) except that all of the points along a field line are properly tied together and are actually common values to all points on equipotential field lines.

By equation (2.16), the current divergence must be zero, $\nabla \cdot \mathbf{J} = 0$. Assume the plane wave solutions $E_{x1} = \delta E_x e^{i(\omega t - kx)}$ and $n_{i1} = \delta n_i e^{i(\omega t - kx)}$ where k is the zonal wave number and n_{i1} is

the ion density perturbation from the ambient density, n_0. Taking the divergence of (2.43), setting it to zero, using the plane wave solutions, dropping second-order terms, and using the electric field mapping for dipole magnetic fields (B.1) derived in the appendix, the linearization of the zonal current divergence equation yields

$$\delta E_x|_{\theta=0} = \frac{-\int \frac{Mg'}{B}\delta n_i dy}{\int \frac{\sigma_p}{\cos^3\theta} dy}$$

$$E_{x1} = \frac{-\int \frac{Mg'}{B} n_1 dy}{\cos^3(\theta) \cdot \int (dy \cdot \sigma_p / \cos^3\theta)} = -\frac{1}{\sigma_p'} \frac{\int \frac{Mg'}{B} n_1 dy}{\int dy} \tag{2.44}$$

where $\delta E_x|_{\theta=0}$ is δE_x, evaluated at the magnetic equator, and we define an effective Pedersen conductivity as $\sigma_p' \equiv \cos^3(\theta) \cdot \int \left(dy \cdot \sigma_p / \cos^3\theta\right) / \int dy$. We neglect the second-order term involving the change in σ_p due to density perturbations for two reasons. For cases where n_{i1} and E_{x1} are small compared to the ambient density and ambient zonal electric field, respectively, the second-order term is negligible. Second-order terms are often neglected in linear analysis. Even if n_{i1} and E_{x1} are not small, the change in the effective Pedersen conductivity, σ_p', is negligible. Depletions are found in the F region and, while they affect σ_p in the F region, they will not significantly affect σ_p at lower altitudes. Since the effective Pedersen conductivity is dominated by σ_p in the minimally affected lower altitudes, neglecting the changes of σ_p due to density perturbations is justified. Equation (2.44) describes the polarization electric field that develops to relieve any current divergence due to density perturbations along a field line. A circuit analogy to E_{x1} as formulated by (2.44) is the voltage that results from several current sources and conductors in parallel with one another. The voltage across such a circuit would be the total current sources divided by the total conductance. In our case, the divergences of gravity-driven currents are current sources and the Pedersen conductivities are conductors, both of which are tied together in parallel by magnetic field lines.

Let us compare the polarization electric field neglecting the parallel dimension (2.38),

$$E_{x1} = \frac{-\frac{Mg'}{B} n_{i1}}{\sigma_p} \tag{2.45}$$

and the polarization electric field assuming equipotential magnetic field lines,

$$E_{x1} = \frac{-\int \frac{Mg'}{B} n_1 dy}{\cos^3(\theta) \cdot \int (dy \cdot \sigma_p / \cos^3 \theta)}. \tag{2.46}$$

Equation (2.46) reduces to equation (2.45) if integrated over an infinitesimal length along the Earth's magnetic field line. However, extending the integration along the whole field line, equation (2.46) decreases drastically because of the integral in the denominator. Magnetic field lines extend into the E region at lower altitudes where the Pedersen conductivity, σ_p, is extremely high (much higher than in the F region), resulting in an increased denominator and subsequently decreased polarization electric field. Deriving the analytical growth rate considering the parallel dimension is complicated. This is because the continuity equation coupled with the polarization electric field,

$$\partial_t n_i = -\partial_z n_{i0} \cdot \frac{E_{x1}}{B}, \tag{2.47}$$

varies along the magnetic field line because $\partial_z n_{i0}$ varies. Furthermore, this complicates the integral of the numerator in equation (2.46). However, when considering the parallel dimension, it can be said that polarization electric fields will be decreased due to current flow through the high Pedersen conductivity in the E region. In turn this drastically reduces the growth of the Rayleigh-Taylor mode that relies on polarization electric field to grow. A full derivation of the growth rate considering the parallel dimension can be found in *Rappaport* (1996).

2.5 Alfvén wave generator

In Section 2.4, we described how polarization electric fields that develop withing plasma bubbles interact with the Pedersen conductivity in the E region. The question remains: what processes allow for the communication between the bubble and the E region? Previously, equatorial plasma bubble dynamics have been assumed to be electrostatic; that is, $d\mathbf{B}/dt = 0$. This is a fair approximation in the interest of typical bubble growth with growth rates on the order of tens of minutes to hours, whereas Alfvénic (or electromagnetic) dynamics are on the scale of seconds to tens of seconds (*Basu*, 2005). However, it is the electromagnetic dynamics (where $d\mathbf{B}/dt \neq 0$) that are responsible for carrying information from the bubble to the E region (*Bhattacharyya and Burke*, 2000; *Basu*, 2005). Specifically, shear Alfvén waves carry electromagnetic information from the bubble to the E region, where a bubble in the F region acts as an Alfvén wave generator as illustrated in Figure 2.4. A bubble in the F region creates a divergence in gravity-driven currents that generates polarization electric fields and Alfvén waves that are transmitted along Earth's magnetic field lines to the E region at higher magnetic latitudes and lower altitudes

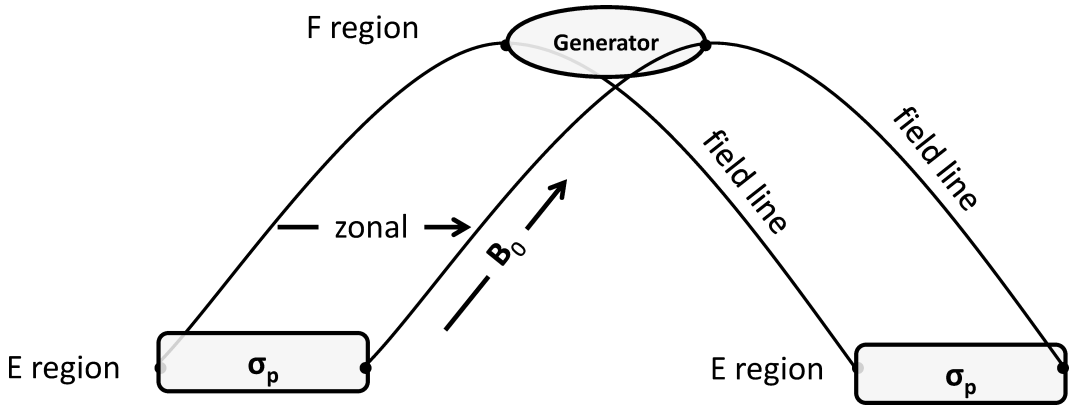

Figure 2.4: Alfvén wave generator diagram. A bubble in the F region creates a divergence of current that generates a polarization electric field that is transmitted to the E region via Earth's magnetic field lines. Information is carried by Alfvén waves.

The Alfvénic nature of the Raleigh-Taylor mode is analytically shown first by simplifying the

problem into a 2-D problem where the bubble generates a divergence of current that flows freely along Earth's magnetic field lines (equipotential field line approximation) and eventually closes through the E region where the Pedersen conductivity is highest, illustrated as σ_p conductors in Figure 2.4. In this problem we only consider currents driven by static electric field (A.10), gravity-driven currents (A.13), and polarization currents (A.21). For this problem, the currents density (2.14) associated with the bubble can be expressed as

$$\mathbf{J} = J_{x1}\hat{\mathbf{x}} + J_{y1}\hat{\mathbf{y}}, \tag{2.48}$$

where $\hat{\mathbf{x}}$ is zonal, $\hat{\mathbf{y}}$ is parallel to Earth's magnetic field, and

$$J_{x1} = \sigma_p E_{x1} + \frac{Mg}{B} n_{i1} + \frac{Mn_e}{B^2}\partial_t E_{x1} \tag{2.49}$$

$$J_{y1} = -\partial x B_{z1}, \tag{2.50}$$

where we can determine the parallel currents (J_{y1}) from the y-component of Ampere's law. Satisfying the rest of Ampere's law (specifically the x-component of Ampere's law),

$$\partial_y B_{z1} = \mu_0 \left(\sigma_p E_{x1} + \frac{Mg}{B} n_{i1} + \frac{Mn_e}{B^2}\partial_t E_{x1} \right). \tag{2.51}$$

We can solve equation (2.51) for $\partial_t E_{x1}$,

$$\partial_t E_{x1} = V_a^2 \cdot \left(\partial_y B_{z1} - \mu_0 \sigma_p E_{x1} - \mu_0 \frac{Mg}{B} n_{i1} \right), \tag{2.52}$$

where we define the Alfvén speed, $V_a = B/\sqrt{\mu_0 n_e M}$. Equation (2.52) describes how E_{x1} develops in order for the system to reach an electrostatic state (where $\nabla \cdot \mathbf{J} = 0$). By taking the partial time

derivative of equation (2.52),

$$\partial_t^2 E_{x1} = V_a^2 \cdot \left(\partial_y \partial_t B_{z1} - \mu_0 \sigma_p \partial_t E_{x1}\right), \tag{2.53}$$

we can show that the developing E_{x1} is Alfvénic in nature. Recall that by Faraday's law, $\partial_t B_{z1} = \partial_y E_{x1}$. Hence, equation (2.53) can be expressed as

$$\partial_t^2 E_{x1} = V_a^2 \cdot \left(\partial_y^2 E_{x1}^2 - \mu_0 \sigma_p \partial_t E_{x1}\right), \tag{2.54}$$

Substituting E_{x1} with the plane wave solution,

$$E_{x1} \propto e^{j(\omega t - k_y y)}, \tag{2.55}$$

(where k_y is 2π divided by the parallel wave length and ω is the wave frequency) solving equation (2.54) for ω yields the dispersion relation,

$$\omega = \left[\pm\sqrt{1 - \left(\frac{V_a \mu_0 \sigma_p}{2k_y}\right)^2} + i\frac{V_a \mu_0 \sigma_p}{2k_y}\right] \cdot V_a k_y, \tag{2.56}$$

which is the dispersion of the Alfvén wave mode through a medium with finite transverse conductivity. Hence, we deem the developing polarization electric field to be Alfvénic. These particular Alfvén waves are shear Alfvén waves that propagate in the parallel direction with a phase and group speed,

$$\frac{\omega}{k_y} = \frac{d\omega}{dk_y} = \left[\pm\sqrt{1 - \left(\frac{V_a \mu_0 \sigma_p}{2k_y}\right)^2} + i\frac{V_a \mu_0 \sigma_p}{2k_y}\right] \cdot V_a. \tag{2.57}$$

Note that the phase and group speed are equal to the Alfvén speed in the collisionless regime, where $\sigma_p = 0$.

2.6 Diamagnetic currents

Now let us consider warm plasmas (finite T_i and T_e). Weakly collisional and collisionless magnetized plasmas develop diamagnetic currents in the presence of pressure gradient forces across Earth's magnetic field. As derived in the appendix, the current density for a weakly collisional plasma ($\nu_i^2 \ll \Omega i^2$, $\nu_e \ll \Omega e$, $\nu_e \sim 0$) driven solely by pressure gradients perpendicular to $\mathbf{B}$ is expressed by equation (A.15),

$$\mathbf{J}_{diamagnetic} = -\nabla \left(p_i + p_e\right) \times \frac{\mathbf{B}_0}{|\mathbf{B}_0|^2}, \tag{2.58}$$

where p_i is ion pressure, p_e is electron pressure, and $\mathbf{B}_0$ is Earth's magnetic field. For a magnetized plasma blob as illustrated in Figure 2.5, currents will flow with a curl in the opposite direction as $\mathbf{B}_0$. By Ampere's law, this current loop results in a perturbation $\mathbf{B}_1$ in the opposite direction of $\mathbf{B}_0$. The opposing $\mathbf{B}_1$ is the reason why these currents are called diamagnetic. Balancing pressure perturbations due to a perturbation in ion density (n_{i1}) with magnetic pressure perturbations, *Lühr et al.* (2003) derived the first-order approximation of the parallel perturbation magnetic field due to diamagnetic currents,

$$B_1 = -n_{i1} k_b \left(T_i + T_e\right) \frac{\mu_0}{B_0}, \tag{2.59}$$

where k_b is the Boltzmann constant.

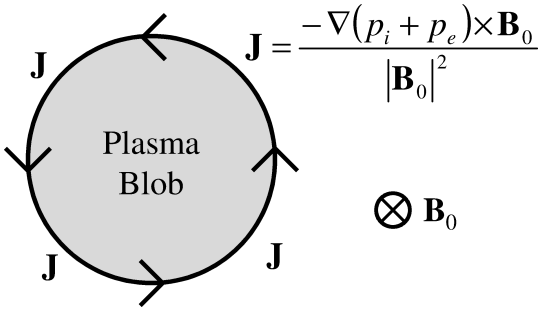

Figure 2.5: Diamagnetic diagram. Given a plasma blob in the presence of a magnetic field, $\mathbf{B}_0$, pressure gradient forces drive diamagnetic currents that flow along the edge of the plasma in the plane perpendicular to $\mathbf{B}_0$.

Note that the diamagnetic currents associated with plasma bubbles do not affect the Rayleigh-Taylor mode. The Rayleigh-Taylor instability feeds off current divergence that result in polarization electric fields that impose a force on the bubble. However, the divergence of diamagnetic current is

$$\begin{aligned} \nabla \cdot \mathbf{J}_{diamagnetic} &= \nabla \cdot \left[-\nabla \left(p_i + p_e \right) \times \frac{\mathbf{B}_0}{|\mathbf{B}_0|^2} \right] \\ &= \frac{\mathbf{B}_0}{|\mathbf{B}_0|^2} \cdot \left[\nabla \times -\nabla \left(p_i + p_e \right) \right] - \nabla \left(p_i + p_e \right) \cdot \left[\frac{\nabla \times \mathbf{B}_0}{|\mathbf{B}_0|^2} \right]. \end{aligned} \tag{2.60}$$

The first term on the right-hand side is zero, because the curl of a gradient is always zero. The second term is approximately zero because Earth's magnetic field lines are effectively straight lines and thus $\nabla \times \mathbf{B}_0 \simeq 0$. Hence, diamagnetic currents are nearly divergence-free and do not result in polarization electric fields that impose electromagnetic forces on the plasma bubble. Diamagnetic currents are passive.

2.7 Ambipolar currents

Previously in Section 2.6, we considered pressure gradients across $\mathbf{B}$ and neglected pressure gradients parallel to $\mathbf{B}$. As illustrated in Figure 2.6a, pressure gradients parallel to $\mathbf{B}$ impose a force on both electrons and ions that result in diffusion. Because electrons are lighter, electrons would initially diffuse faster than ions. However, this results in charge separation and development of ambipolar electric fields as illustrated in Figure 2.6b. Ambipolar electric fields develop to keep the electrons from diffusing faster than ions to maintain quasi-neutrality.

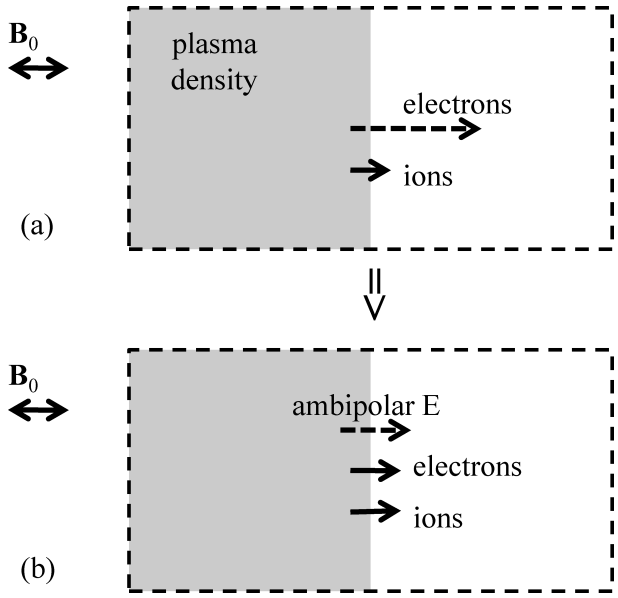

Figure 2.6: Diagram of the development of ambipolar electric fields. Given a pressure gradient, both electrons and ions initially want to diffuse to lower densities. Since electrons are lighter, they would diffuse faster than ions without the presence of electric fields. However this difference of diffusion induces a separation of charges and results in an ambipolar electric field that reduces the electron diffusion until it matches the ion diffusion and maintains quasi-neutrality.

In one dimension (1-D), quasi-neutrality implies that electron and ion velocities are equal. Neglecting gravity and collisions between ion and electrons ($\nu_{ie} = 0$ and $\nu_{ei} = 0$), setting the electrostatic ($d\mathbf{v}_i/dt = 0$) parallel ion velocity (2.10) equal to the electrostatic ($d\mathbf{v}_e = dt = 0$) parallel electron velocity (2.11) yields

$$\frac{1}{\nu_i}\left(\frac{eE_y}{M} - \frac{\partial_y p_i}{n_i M}\right) = \frac{1}{\nu_e}\left(-\frac{eE_y}{m} - \frac{\partial_y p_e}{n_e m}\right). \tag{2.61}$$

Considering that $\nu_i M \gg \nu_e m$, we can solve for E_y, the 1-D ambipolar electric field:

$$E_{ambipolar} = -\frac{\partial_y p_e}{e n_e}. \tag{2.62}$$

Note that this 1-D ambipolar electric field does not apply in two or more dimensions when current

loops can form to maintain quasi-neutrality. With current loops, ion velocity isn't necessarily equal to electron velocity, as in this derivation of the 1-D ambipolar electric field. We will later model 3-D ambipolar currents and electric fields and show that ambipolar electric fields are less than 1-D theory suggests.

Chapter 3

Formulation

In this chapter, we will describe the model formulation of EMI. Traditional low-latitude ionospheric models assume electrostatic conditions (*Huba et al.*, 2000, 2008; *Retterer*, 2005, 2010; *Aveiro and Hysell*, 2010). Under the electrostatic approximation, electric fields are irrotational ($\nabla \times \mathbf{E} = 0$). Thus, electric fields can be completely described using scalar potential Φ such that $\mathbf{E} = -\nabla\Phi$. With potential solvers, these models determine a solution for Φ such that currents are divergent free ($\nabla \cdot \mathbf{J} = 0$). *Huba et al.* (2008) and *Retterer* (2010) simplify the potential solve by approximating Earth's magnetic field lines to be equipotential and simplifying the 3-D potential problem into a 2-D potential problem. *Aveiro and Hysell* (2010) solves the 3-D potential problem. While the 2-D potential problem take significantly less computational time than the 3-D potential problem, there can be significant implications when approximating Earth's magnetic field lines to be perfectly equipotential (*Aveiro and Hysell*, 2010, 2012). All of these models provide great insight into the development of low-latitude plasma irregularities. However, with the electrostatic approximation, the dynamic electromagnetic processes cannot be resolved. The electric fields that carry electromagnetic waves are not irrotational and thus are not electrostatic. In the interest of exploring a larger set of electromagnetic characteristics than the electrostatic approximation allows, we devel-

oped EMI, an electromagnetic model that makes use of Maxwell's equations to include dynamic electromagnetic wave physics. Inclusion of electrodynamics allows us to resolve the Alfvénic characteristics previously discussed in *Bhattacharyya and Burke* (2000), *Basu* (2005), and *Burke et al.* (2012).

3.1 Formulation

EMI's model equations are based on Maxwell's equations, the current density equation, the ion continuity equation, the single species ion momentum equation, and the electron momentum equation,

$$\nabla \cdot \mathbf{B} = 0 \tag{3.1}$$

$$\nabla \cdot \mathbf{E} = \frac{e}{\epsilon_0}\left(n_{i-} n_e\right) \tag{3.2}$$

$$\partial_t \mathbf{B} = -\nabla \times \mathbf{E} \tag{3.3}$$

$$\partial_t \mathbf{E} = c^2\left(\nabla \times \mathbf{B} - \mu_0 \mathbf{J}\right) \tag{3.4}$$

$$\mathbf{J} = e n_e (\mathbf{v}_i - \mathbf{v}_e) \tag{3.5}$$

$$\partial_t n_i = -\nabla \cdot (n_i \mathbf{v}_i) \tag{3.6}$$

$$\begin{aligned} \frac{D\mathbf{v}_i}{Dt} &= \frac{e}{M}\left(\mathbf{E} + \mathbf{v}_i \times \mathbf{B}\right) + \mathbf{g} - \frac{\nabla p_i}{n_i M} \\ &\quad - \nu_{ie}\left(\mathbf{v}_i - \mathbf{v}_e\right) - \nu_{in}\left(\mathbf{v}_i - \mathbf{v}_n\right) \end{aligned} \tag{3.7}$$

$$\begin{aligned} \frac{D\mathbf{v}_e}{Dt} &= -\frac{e}{m}\left(\mathbf{E} + \mathbf{v}_e \times \mathbf{B}\right) + \mathbf{g} - \frac{\nabla p_e}{n_e m} \\ &\quad - \nu_{ei}\left(\mathbf{v}_e - \mathbf{v}_i\right) - \nu_{en}\left(\mathbf{v}_e - \mathbf{v}_n\right) \end{aligned} \tag{3.8}$$

where ∂_t is the partial time derivative, D/Dt is the advective derivative ($\partial_t + \mathbf{v}_i \cdot \nabla$ for ions and $\partial_t + \mathbf{v}_e \cdot \nabla$ for electrons), and the rest of the notation is found in the Nomenclature section (on page xvii). However, we rearrange and make a few approximations to equations (3.1) through (3.8).

First, by taking the divergence of Maxwell-Faraday's and Maxwell-Ampere's equations (3.3) and (3.4), it is apparent that they also model both of Gauss's equations (3.1) and (3.2) as long as initial conditions also satisfy Gauss's equations. Hence, we can model all four of Maxwell's equations with just equations (3.3) and (3.4), making sure the initial conditions satisfy Gauss's equations.

To include Alfvénic physics, we must include ion inertia in the current density $\mathbf{J}$ found in Maxwell-Ampere's equation (3.4). In other words, we must include polarization currents. However, time-integrating $\mathbf{E}$ with equation (3.4) can be challenging if it involves the partial derivative of ion velocity $\partial_t \mathbf{v}_i$ embedded in $\mathbf{J}$. Instead, we derive a current density equation that does not directly involve computing $\partial_t \mathbf{v}_i$ but still manages to include ion inertia. Neglecting electron inertia and ion inertia parallel to $\mathbf{B}$, we rearrange the momentum equations (3.7) and (3.8) and solve for the ion and electron velocity as

$$\mathbf{v}_i = \tilde{\mathbf{A}}_i \left(\frac{e}{M}\mathbf{E} + \mathbf{g} - \frac{\nabla p_i}{n_i M} + \nu_{ie}\mathbf{v}_e + \nu_{in}\mathbf{v}_n - \frac{D\mathbf{v}_{i\perp}}{Dt} \right) \tag{3.9}$$

$$\mathbf{v}_e = \tilde{\mathbf{A}}_e \left(-\frac{e}{m}\mathbf{E} + \mathbf{g} - \frac{\nabla p_e}{n_e m} + \nu_{ei}\mathbf{v}_i + \nu_{en}\mathbf{v}_n \right), \tag{3.10}$$

where the $\perp$ subscript denotes perpendicular (to $\mathbf{B}$) components. The $\tilde{\mathbf{A}}_i$ and $\tilde{\mathbf{A}}_e$ are tensors, defined as

$$\tilde{\mathbf{A}}_{(\sigma=i,e)} = \begin{bmatrix} \nu_\sigma & -\Omega_{\sigma z} & \Omega_{\sigma y} \\ \Omega_{\sigma z} & \nu_\sigma & -\Omega_{\sigma x} \\ -\Omega_{\sigma y} & \Omega_{\sigma x} & \nu_\sigma \end{bmatrix}^{-1}, \tag{3.11}$$

where $\nu_i = \nu_{in} + \nu_{ie}$, $\nu_e = \nu_{en} + \nu_{ei}$, and we define the gyrofrequency components as

$$\begin{bmatrix} \Omega_{ix} \\ \Omega_{iy} \\ \Omega_{iz} \end{bmatrix} \equiv \frac{e\mathbf{B}}{M}, \quad \begin{bmatrix} \Omega_{ex} \\ \Omega_{ey} \\ \Omega_{ez} \end{bmatrix} \equiv -\frac{e\mathbf{B}}{m}. \tag{3.12}$$

Electron inertia is neglected ($d\mathbf{v}_e/dt = 0$) because we assume electron dynamics reach an equilibrium virtually instantly due to small electron mass. This also implies a neglect of parallel ion inertia, since ions are relatively fixed compared to the lighter electrons that are free to move in the parallel direction. Note that we stress the inclusion of both $\mathbf{B}_0$ (the background magnetic field vector) and $\mathbf{B}_1$ (the perturbation magnetic field vector) in equation (3.12). Although magnetic field perturbations are several orders less than Earth's magnetic field, $\mathbf{B}_1$ perpendicular to $\mathbf{B}_0$ can be important to dynamics in the collisionless regime (*Seyler*, 1990).

We take the zero order ion velocity as equation (3.9) without ion inertia:

$$\overline{\mathbf{v}}_i = \tilde{\mathbf{A}}_i \left(\frac{e\mathbf{E}}{M} + \mathbf{g} - \frac{\nabla p_i}{n_i M} + \nu_{ie}\mathbf{v}_e + \nu_{in}\mathbf{v}_n \right). \tag{3.13}$$

Making the first-order approximation that $D\mathbf{v}_i/Dt \approx D\overline{\mathbf{v}}_i/Dt$, we approximate ion inertia by taking the derivative of equation (3.13), which results in

$$\frac{D\mathbf{v}_i}{Dt} = \tilde{\mathbf{A}}_i \cdot \frac{e}{M} \left(\partial_t \mathbf{E} \right) + \overline{\mathbf{v}}_i \cdot \nabla \overline{\mathbf{v}}_i, \tag{3.14}$$

where we neglect electron inertia again and assume gravity, pressure, and neutral winds to be constant relative to the electrodynamics we wish to model. Substituting equation (3.14) into (3.9) yields

$$\begin{aligned}
\mathbf{v}_i =& \tilde{\mathbf{A}}_i \left(\frac{e}{M}\mathbf{E}_\parallel + \mathbf{g} - \frac{\nabla p_i}{n_i M} + \nu_{ie}\mathbf{v}_e + \nu_{in}\mathbf{v}_n - \overline{\mathbf{v}}_i \cdot \nabla \overline{\mathbf{v}}_{i\perp} \right) \\
&+ \left(p - h\frac{\mathbf{B}}{|\mathbf{B}|}\times \right) \frac{e}{M}\mathbf{E}_\perp \\
p =& \frac{1}{\nu_i^2 + \Omega_i^2} \left(\nu_i + \frac{\Omega_i^2}{\nu_i^2 + \Omega_i^2}\partial_t - \frac{\nu_i^2}{\nu_i^2 + \Omega_i^2}\partial_t \right) \\
\approx& \frac{1}{\nu_i^2 + \Omega_i^2} \left(\nu_i + \frac{\Omega_i^2}{\nu_i^2 + \Omega_i^2}\partial_t \right) \\
h =& \frac{1}{\nu_i^2 + \Omega_i^2} \left(\Omega_i + \frac{2\Omega_i\nu_i}{\nu_i^2 + \Omega_i^2}\partial_t \right) \approx \frac{\Omega_i}{\nu_i^2 + \Omega_i^2},
\end{aligned} \tag{3.15}$$

where the subscript $\|$ denotes components parallel to $\mathbf{B}$. Approximations are made to p and h considering the time scale of interest. In p, regardless of time scale, $\left[\nu_i^2/\left(\nu_i^2+\Omega_i^2\right)\right]\cdot\partial_t$ is dominated by $\left[\Omega_i^2/\left(\nu_i^2+\Omega_i^2\right)\right]\cdot\partial_t$ for $\nu_i \ll \Omega_i$. However, for $\nu_i \gtrsim \Omega_i$, we must compare $\left[\nu_i^2/\left(\nu_i^2+\Omega_i^2\right)\right]\cdot\partial_t$ to ν_i (found in the first term). To do this, we compare $\left[\nu_i^2/\left(\nu_i^2+\Omega_i^2\right)\right]/\Delta t$ to ν_i where Δt is the time scale of interest. Since Alfvén wave speeds in the ionosphere are typically on the order of 100 km/s and we wish to resolve parallel length scales of at least 100 km, the time scale of interest is on the order of seconds ($\Delta t \sim 1$ s). Consequently, for ν_i comparable to or greater than Ω_i (which is on the order of 100 Hz), $\left[\nu_i^2/\left(\nu_i^2+\Omega_i^2\right)\right]\cdot\partial_t$ is dominated by ν_i. Since $\left[\nu_i^2/\left(\nu_i^2+\Omega_i^2\right)\right]\cdot\partial_t$ is dominated for ν_i less than, greater than, or similar to Ω_i, we neglect it altogether. In h, we neglect the partial derivative term because it is dominated by Ω_i; the maximum of $2\Omega_i\nu_i/\left(\nu_i^2+\Omega_i^2\right)$ is unity and $\Omega_i \gg 1/\Delta t$.

Taking the difference of the ion and electron velocity equations (3.15) and (3.10) and multiplying this difference by the charge density, en_e, yields current density that does not directly involve the partial time derivative of ion velocity

$$\begin{aligned}\mathbf{J} = &\frac{\Omega_i^2}{\left(\Omega_i^2+\nu_i^2\right)^2}\frac{n_e e^2}{M}\partial_t\mathbf{E}_\perp \\ &+ en_e\tilde{\mathbf{A}}_i\left(\frac{e\mathbf{E}}{M}+\mathbf{g}-\frac{\nabla p_i}{n_i M}+\nu_{ie}\mathbf{v}_e+\nu_{in}\mathbf{v}_n-\overline{\mathbf{v}}_i\cdot\nabla\overline{\mathbf{v}}_{i\perp}\right) \\ &- en_e\tilde{\mathbf{A}}_e\left(-\frac{e\mathbf{E}}{M}+\mathbf{g}-\frac{\nabla p_e}{n_e m}+\nu_{ei}\overline{\mathbf{v}}_i+\nu_{en}\mathbf{v}_n\right),\end{aligned} \tag{3.16}$$

where ion inertia is represented by the first term. Substituting equation (3.16) into Maxwell-Ampere's equation (3.4) and solving for $\partial_t\mathbf{E}$ yields what will be referred to as the Alfvénic Maxwell-Ampere's equation

$$\begin{aligned}\partial_t\mathbf{E} = &\frac{c^2V_a^2}{c^2+V_a^2}\left[\nabla\times\mathbf{B}-\mu_0\mathbf{J}'\right]_\perp \\ &+c^2\left[\nabla\times\mathbf{B}-\mu_0\mathbf{J}'\right]_\|,\end{aligned} \tag{3.17}$$

where V_a, the Alfvén speed, is

$$V_a = \frac{\Omega_i^2 + \nu_i^2}{\Omega_i^2} \frac{B_0}{\sqrt{\mu_0 n_e M}}, \tag{3.18}$$

and $\mathbf{J}'$ is

$$\begin{aligned} \mathbf{J}' = & e n_e \tilde{\mathbf{A}}_i \left(\frac{e\mathbf{E}}{M} + \mathbf{g} - \frac{\nabla p_i}{n_i M} + \nu_{ie}\mathbf{v}_e + \nu_{in}\mathbf{v}_n - \overline{\mathbf{v}}_i \cdot \nabla \overline{\mathbf{v}}_{i\perp} \right) \\ & - e n_e \tilde{\mathbf{A}}_e \left(-\frac{e\mathbf{E}}{m} + \mathbf{g} - \frac{\nabla p_e}{n_e m} + \nu_{ei}\mathbf{v}_i + \nu_{en}\mathbf{v}_n \right). \end{aligned} \tag{3.19}$$

Equation (3.17) is Maxwell-Ampere's equation rearranged such that ion inertia manifests itself as the Alfvén speed, V_a. By inspection, it is apparent that $\partial_t \mathbf{E}_\perp$ is suppressed with decreasing V_a. This is due to ion inertia limiting sudden development of the perpendicular electric field, $\mathbf{E}_\perp$. Without ion inertia, the Alfvén speed, V_a, would be infinite and the factor $c^2 V_a^2 / \left(c^2 + V_a^2\right)$ would reduce to c^2, resulting in the absence of the Alfvén speed and associated Alfvén wave modes. Note that the Alfvénic Maxwell-Ampere's equation (3.17) is computationally simpler than equation (3.4) since no time derivatives are required to compute polarization currents found in $\mathbf{J}$. Instead, ion inertia is included in the easily computed V_a, the Alfvén speed (3.18).

While EMI is based on equations (3.1) to (3.8), the model is specifically given by Maxwell-Faraday's equation (3.3), the Alfvénic Maxwell-Ampere's equation (3.17), the continuity equation (3.6), the electron velocity equation (3.10), and the ion velocity equation (3.15), rewritten below

for convenience:

$$\partial_t \mathbf{B} = -\nabla \times \mathbf{E} \tag{3.20}$$

$$\begin{aligned}\partial_t \mathbf{E} =& \frac{c^2 V_a^2}{c^2 + V_a^2} \left[\nabla \times \mathbf{B} - \mu_0 \mathbf{J}'\right]_\perp \\ &+ c^2 \left[\nabla \times \mathbf{B} - \mu_0 \mathbf{J}'\right]_\parallel\end{aligned} \tag{3.21}$$

$$\partial_t n_i = -\nabla \cdot (n_i \mathbf{v}_i)\,. \tag{3.22}$$

$$\mathbf{v}_e = \tilde{\mathbf{A}}_e \left(-\frac{e}{m}\mathbf{E} + \mathbf{g} - \frac{\nabla p_e}{n_e m} + \nu_{ei}\mathbf{v}_i + \nu_{en}\mathbf{v}_n\right) \tag{3.23}$$

$$\begin{aligned}\mathbf{v}_i =& \tilde{\mathbf{A}}_i \left(\frac{e}{M}\mathbf{E} + \mathbf{g} - \frac{\nabla p_i}{n_i M} + \nu_{ie}\mathbf{v}_e + \nu_{in}\mathbf{v}_n - \overline{\mathbf{v}}_i \cdot \nabla \overline{\mathbf{v}}_{i\perp}\right) \\ &+ \left(\frac{\Omega_i}{\nu_i^2 + \Omega_i^2}\right)^2 \frac{e}{M} \partial_t \mathbf{E}_\perp.\end{aligned} \tag{3.24}$$

Note that we assume quasi-neutrality and that the equatorial E and F region ionosphere is entirely singly charged ions (O^+, H^+, He^+, O_2^+, NO^+). Hence, throughout this dissertation, $n_i = n_e$, where n_e and n_i are interchangeable.

3.2 Electromagnetic dispersion relation

It is instructive to derive the electromagnetic dispersion relation to see what electromagnetic wave modes EMI supports. Taking cold plasmas for simplicity and focusing our attention to the electromagnetic parts of equations (3.20) and (3.21) ,

$$\partial_t \mathbf{B} = -\nabla \times \mathbf{E} \tag{3.25}$$

$$\begin{aligned}\partial_t \mathbf{E} =& \frac{c^2 V_a^2}{c^2 + V_a^2} \left[\nabla \times \mathbf{B} - \mu_0 \mathbf{J}'\right]_\perp \\ &+ c^2 \left[\nabla \times \mathbf{B} - \mu_0 \mathbf{J}'\right]_\parallel\end{aligned} \tag{3.26}$$

where we only consider the currents coupled with (3.25) and (3.26),

$$\mathbf{J}' = \tilde{\boldsymbol{\sigma}}\mathbf{E}, \tag{3.27}$$

which is just the currents induced by electric fields. The tensor, $\tilde{\boldsymbol{\sigma}}$, is the conductivity tensor (2.15). Let us define an effective Alfvén speed,

$$V_a' \equiv \frac{c^2 V_a^2}{c^2 + V_a^2}, \tag{3.28}$$

where V_a is defined by equation (3.18),

$$V_a = \frac{\Omega_i^2 + \nu_i^2}{\Omega_i^2} \frac{B_0}{\sqrt{\mu_0 n_e M}}. \tag{3.29}$$

Substituting equation (3.27) into (3.25) and (3.26) results in the coupled equations:

$$\partial_t \mathbf{B} = -\nabla \times \mathbf{E} \tag{3.30}$$

$$\begin{aligned} \partial_t \mathbf{E} =& V_a'^2 \left[\nabla \times \mathbf{B} - \mu_0 \tilde{\boldsymbol{\sigma}} \mathbf{E}\right]_\perp \\ &+ c^2 \left[\nabla \times \mathbf{B} - \mu_0 \tilde{\boldsymbol{\sigma}} \mathbf{E}\right]_\parallel . \end{aligned} \tag{3.31}$$

The coupling of these equations support several electromagnetic waves. In order to investigate what modes these equations support, we perform an Eigenmode analysis. First, let us take the time derivative of (3.31),

$$\begin{aligned} \partial_t^2 \mathbf{E} =& V_a'^2 \left[\nabla \times \partial_t \mathbf{B} - \mu_0 \tilde{\boldsymbol{\sigma}} \partial_t \mathbf{E}\right]_\perp \\ &+ c^2 \left[\nabla \times \partial_t \mathbf{B} - \mu_0 \tilde{\boldsymbol{\sigma}} \partial_t \mathbf{E}\right]_\parallel . \end{aligned} \tag{3.32}$$

Note that $\partial_t \mathbf{B}$, is a function of $\mathbf{E}$ by equation (3.30). Substituting equation (3.30) into (3.32) yields

$$\begin{aligned}\partial_t^2 \mathbf{E} =& V_a'^2 \left[-\nabla \times \nabla \times \mathbf{E} - \mu_0 \tilde{\boldsymbol{\sigma}} \partial_t \mathbf{E}\right]_\perp \\ &+ c^2 \left[-\nabla \times \nabla \times \mathbf{E} - \mu_0 \tilde{\boldsymbol{\sigma}} \partial_t \mathbf{E}\right]_\parallel\end{aligned}$$

$$\partial_t^2 \mathbf{E} + V_a'^2 \left[\nabla \times \nabla \times \mathbf{E} + \mu_0 \tilde{\boldsymbol{\sigma}} \partial_t \mathbf{E}\right]_\perp + c^2 \left[\nabla \times \nabla \times \mathbf{E} + \mu_0 \tilde{\boldsymbol{\sigma}} \partial_t \mathbf{E}\right]_\parallel = 0. \tag{3.33}$$

Recall that the curl of the curl of $\mathbf{E}$ is

$$\nabla \times \nabla \times \mathbf{E} = \begin{bmatrix} 0 & -\partial_z & \partial_y \\ \partial_z & 0 & -\partial_x \\ -\partial_y & \partial_x & 0 \end{bmatrix}^2 \cdot \mathbf{E} = \begin{bmatrix} -\partial_y^2 - \partial_z^2 & \partial_x \partial_y & \partial_x \partial_z \\ \partial_x \partial_y & -\partial_x^2 - \partial_z^2 & \partial_y \partial_z \\ \partial_x \partial_z & \partial_y \partial_z & -\partial_x^2 - \partial_y^2 \end{bmatrix} \cdot \mathbf{E}, \tag{3.34}$$

and that $\tilde{\boldsymbol{\sigma}}$ is defined by equation (2.15). Hence, equation (3.33) can be expressed as

$$\begin{bmatrix} \partial_t^2 + V_a'^2\left(-\partial_y^2 - \partial_z^2 + \mu_0 \sigma_p \partial_t\right) & V_a'^2(\partial_x \partial_y) & V_a'^2(\partial_x \partial_z + \mu_0 \sigma_h \partial_t) \\ c^2(\partial_x \partial_y) & \partial_t^2 + c^2\left(-\partial_x^2 - \partial_z^2 + \mu_0 \sigma_0 \partial_t\right) & c^2(\partial_y \partial_z) \\ V_a'^2(\partial_x \partial_z - \mu_0 \sigma_h \partial_t) & V_a'^2(\partial_y \partial_z) & \partial_t^2 + V_a'^2\left(-\partial_x^2 - \partial_y^2 + \mu_0 \sigma_p \partial_t\right) \end{bmatrix} \cdot \mathbf{E} = 0, \tag{3.35}$$

where we pick a coordinate system where $\hat{\mathbf{y}}$ is parallel to $\mathbf{B}$, and both $\hat{\mathbf{x}}$ and $\hat{\mathbf{z}}$ are in the plane perpendicular to $\mathbf{B}$ and perpendicular to each other. Now, let us assume the plane wave solution for $\mathbf{E}$ where $\mathbf{E} \propto e^{i(\omega t - k_x x - k_y y - k_z z)}$, where k_x, k_y, and k_z are components of the $\mathbf{k}$-vector ($\mathbf{k} \equiv k_x \hat{\mathbf{x}} + k_y \hat{\mathbf{y}} + k_z \hat{\mathbf{z}}$) that indicate the direction of wave propagation and the wavelength of the wave,

$\lambda = 2\pi/|\mathbf{k}|$. The derivatives of the plane wave solution are

$$\begin{aligned} \partial_t \mathbf{E} &= i\omega \mathbf{E} \\ \partial_x \mathbf{E} &= -ik_x \mathbf{E} \\ \partial_y \mathbf{E} &= -ik_y \mathbf{E} \\ \partial_z \mathbf{E} &= -ik_z \mathbf{E}. \end{aligned} \tag{3.36}$$

Hence assuming the plane wave solution for $\mathbf{E}$, equation (3.35) can be expressed as

$$\begin{bmatrix} -\omega^2+V_a'^2\left(k_y^2+k_z^2+i\omega\mu_0\sigma_p\right) & V_a'^2(-k_xk_y) & V_a'^2(-k_xk_z+i\omega\mu_0\sigma_h) \\ c^2(-k_xk_y) & -\omega^2+c^2\left(k_x^2+k_z^2+i\omega\mu_0\sigma_0\right) & c^2(-k_yk_z) \\ V_a'^2(-k_xk_z-i\omega\mu_0\sigma_h) & V_a'^2(-k_yk_z) & -\omega^2+V_a'^2\left(k_x^2+k_y^2+i\omega\mu_0\sigma_p\right) \end{bmatrix} \cdot \mathbf{E} = 0. \tag{3.37}$$

We can simplify the analysis by picking a coordinate system where $k_z = 0$ without loss of generality, as done in *Cosgrove and Doe* (2010). This is because you can rotate a coordinate system around $\hat{\mathbf{y}}$ where a general $\mathbf{k}' \equiv k_x'\hat{\mathbf{x}}' + k_y\hat{\mathbf{y}} + k_z'\hat{\mathbf{z}}'$ becomes $\mathbf{k} \equiv k_x\hat{\mathbf{x}} + k_y\hat{\mathbf{y}}$, where $'$ denotes an arbitrary coordinate frame with $\hat{\mathbf{y}} \parallel \mathbf{B}$. In the new coordinate system, $\hat{\mathbf{x}} \parallel k_x'\hat{\mathbf{x}}' + k_z'\hat{\mathbf{z}}'$, $k_x = \sqrt{k_x'^2 + k_z'^2}$, and most importantly $k_z = 0$. The k-vector is as illustrated in Figure 3.1.

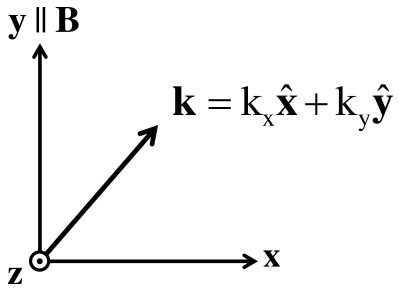

Figure 3.1: General k vector in terms of a perpendicular component and a parallel component.

In this coordinate system where $k_z = 0$, equation (3.37) is simplified to

$$\begin{bmatrix} -\omega^2 + V_a'^2\left(k_y^2 + i\omega\mu_0\sigma_p\right) & V_a'^2\left(-k_xk_y\right) & V_a'^2\left(i\omega\mu_0\sigma_h\right) \\ c^2\left(-k_xk_y\right) & -\omega^2 + c^2\left(k_x^2 + i\omega\mu_0\sigma_0\right) & 0 \\ V_a'^2\left(-i\omega\mu_0\sigma_h\right) & 0 & -\omega^2 + V_a'^2\left(k_x^2 + k_y^2 + i\omega\mu_0\sigma_p\right) \end{bmatrix} \cdot \mathbf{E} = 0. \tag{3.38}$$

For non-trivial solutions, the determinant of the matrix is equal to zero. Hence,

$$\begin{aligned} \left[-\omega^2 + V_a'^2\left(k_y^2 + i\omega\mu_0\sigma_p\right)\right]\left[-\omega^2 + c^2\left(k_x^2 + i\omega\mu_0\sigma_0\right)\right]\left[-\omega^2 + V_a'^2\left(k_x^2 + k_y^2 + i\omega\mu_0\sigma_p\right)\right] \\ - \left(-V_a'^2k_xk_y\right)\left(-c^2k_xk_y\right)\left[-\omega^2 + V_a'^2\left(k_x^2 + k_y^2 + i\omega\mu_0\sigma_p\right)\right] \\ - \left[V_a'^2\left(i\omega\mu_0\sigma_h\right)\right]^2\left[-\omega^2 + c^2\left(k_x^2 + i\omega\mu_0\sigma_0\right)\right] = 0, \end{aligned} \tag{3.39}$$

describing the general wave dispersion for EMI. It is fairly complicated as it is a function of V_a', c, σ_p, σ_h, σ_0, ω, k_x, and k_y. We will go over several of the supported wave modes.

3.2.1 Zero conductivity: Pure Alfvén and light wave modes

First, let us neglect conductivities. Equation (3.38) becomes

$$\begin{bmatrix} -\omega^2 + V_a'^2k_y^2 & -V_a'^2k_xk_y & 0 \\ -c^2k_xk_y & -\omega^2 + c^2k_x^2 & 0 \\ 0 & 0 & -\omega^2 + V_a'^2\left(k_x^2 + k_y^2\right) \end{bmatrix} \cdot \mathbf{E} = 0. \tag{3.40}$$

It is apparent that E_z is not coupled to E_x nor E_y. Hence, waves carried by E_z are solely carried by E_z. The dispersion relation for waves carried by E_z can be found simply be writing out the E_z equation from (3.40),

$$\left[-\omega^2 + V_a'^2\left(k_x^2 + k_y^2\right)\right] \cdot E_z = 0 \tag{3.41}$$

For non-trivial solutions,

$$\omega^2 = V_a'^2 k^2, \tag{3.42}$$

where $k = \sqrt{k_x^2 + k_y^2}$. This is simply the wave dispersion for an Alfvén wave, where the phase and group speed are

$$\frac{\omega}{k} = \pm V_a' \tag{3.43}$$

and

$$\frac{d\omega}{dk} = \pm V_a'. \tag{3.44}$$

Without conductivities, waves carried by E_z (electric field perpendicular to both $\mathbf{B}$ and $\mathbf{k}$) are Alfvén waves that move at the Alfvén speed, V_a'.

Now let us bring our attention back to equation (3.40) and solve for the dispersion relation for waves carried by E_x and E_y. Since E_x and E_y are decoupled from E_z, the non-trivial solutions can be found by setting the determinant of the top-left 2 by 2 elements in the matrix of equation (3.40) to zero,

$$\left(-\omega^2 + V_a'^2 k_y^2\right)\left(-\omega^2 + c^2 k_x^2\right) - \left(V_a' c k_x k_y\right)^2 = 0,$$

which when written out is

$$\omega^4 - \left(V_a'^2 k_y^2 + c^2 k_x^2\right)\omega^2 = 0. \tag{3.45}$$

Solving for ω^2 yields

$$\omega^2 = V_a'^2 k_y^2 + c^2 k_x^2. \tag{3.46}$$

Dividing equation (3.46) by $\sqrt{k_x^2 + k_y^2}$ results in the phase speed,

$$\frac{\omega^2}{k^2} = V_a'^2 \cdot \frac{k_y^2}{\sqrt{k_x^2 + k_y^2}} + c^2 \cdot \frac{k_x^2}{\sqrt{k_x^2 + k_y^2}}$$

$$\frac{\omega}{k} = \sqrt{V_a'^2 \cdot \frac{k_y^2}{\sqrt{k_x^2 + k_y^2}} + c^2 \cdot \frac{k_x^2}{\sqrt{k_x^2 + k_y^2}}}. \tag{3.47}$$

Let us also define ϕ as the angle between $\mathbf{k}$ and $\mathbf{B}$. Then the phase speed can be written out as

$$\frac{\omega}{k} = \pm\sqrt{V_a'^2 \cos^2\phi + c^2 \sin^2\phi}. \tag{3.48}$$

Since the phase speed is independent of k, the group speed is the same as the phase speed,

$$\frac{d\omega}{dk} = \frac{\omega}{k}. \tag{3.49}$$

Without conductivities, waves carried by E_x and E_y (electric fields in the plane of $\mathbf{k}$ and $\mathbf{B}$) are electromagnetic waves that move at the speed between V_a' and c depending on ϕ. The phase speed versus ϕ for different ratios of V_a' to c is plotted in Figure 3.2. For propagation parallel to $\mathbf{B}$, waves carried solely by E_x are purely Alfvénic and propagate at the Alfvén speed, V_a'. For propagation perpendicular to $\mathbf{B}$, waves carried by E_y are purely light waves and propagate at the speed of light, c. For ϕ in between perpendicular or parallel to $\mathbf{B}$, the phase speed is between the Alfvén speed and speed of light as formulated by (3.48) and plotted on a polar plot in Figure 3.2 for different ratios of V_a' to c.

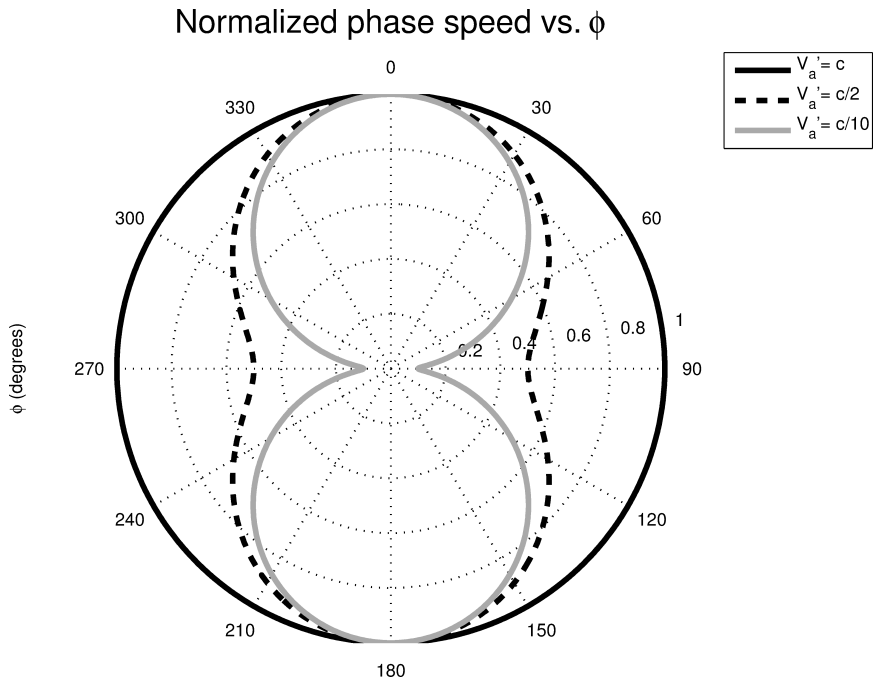

Figure 3.2: Polar plot of phase speed (normalized by the speed of light) of waves carried by E_x and E_y versus ϕ. The solid black line circle is when $V_a' = c$. The dotted black line circle is when $V_a' = c/2$. The solid gray line circle is when $V_a' = c/10$.

3.2.2 Finite Conductivity: Wave propagation perpendicular to B

Let us now consider finite conductivity and its effect on EMI's dispersion relation. For wave propagation perpendicular to background magnetic field ($k_y = 0$), equation (3.38) becomes

$$\begin{bmatrix} -\omega^2 + i\omega V_a'^2 \mu_0 \sigma_p & 0 & i\omega V_a'^2 \mu_0 \sigma_h \\ 0 & -\omega^2 + c^2\left(k_x^2 + i\omega\mu_0\sigma_0\right) & 0 \\ -i\omega V_a'^2 \mu_0 \sigma_h & 0 & -\omega^2 + V_a'^2\left(k_x^2 + i\omega\mu_0\sigma_p\right) \end{bmatrix} \cdot \mathbf{E} = 0. \qquad (3.50)$$

It is apparent that E_y is decoupled from E_x and E_z. The dispersion relation for waves carried by E_y can be found by writing out the E_y equation from (3.50),

$$\left[-\omega^2 + c^2\left(k_x^2 + i\omega\mu_0\sigma_0\right)\right] \cdot E_y = 0. \tag{3.51}$$

For non-trivial solutions,

$$\omega^2 - c^2\left(k_x^2 + i\omega\mu_0\sigma_0\right) = 0$$

$$\frac{\omega^2}{k_x^2} - i\frac{c^2\mu_0\sigma_0}{k_x}\frac{\omega}{k_x} - c^2 = 0$$

$$\frac{\omega}{k_x} = \frac{i\frac{c^2\mu_0\sigma_0}{k_x} \pm \sqrt{\left(i\frac{c^2\mu_0\sigma_0}{k_x}\right)^2 + 4c^2}}{2}$$

$$\frac{\omega}{k_x} = \left[\pm\sqrt{1 - \left(\frac{c\mu_0\sigma_0}{2k_x}\right)^2} + i\frac{c\mu_0\sigma_0}{2k_x}\right] \cdot c, \tag{3.52}$$

which describes a light wave propagating through finite σ_0. Note that for $\sigma_0 = 0$, equation (3.52) reduces to equation (3.48) for $\phi = \pi/2$, which is simply a pure light wave carried by E_y. Finite σ_0 slows down the light wave (as seen the real part of 3.52) and decays the light wave (as seen in the imaginary part of 3.52).

For waves carried by E_x and E_z, we reduce equation (3.50) to

$$\begin{bmatrix} -\omega^2 + i\omega V_a'^2\mu_0\sigma_p & i\omega V_a'^2\mu_0\sigma_h \\ -i\omega V_a'^2\mu_0\sigma_h & -\omega^2 + V_a'^2\left(k_x^2 + i\omega\mu_0\sigma_p\right) \end{bmatrix} \cdot \begin{bmatrix} E_x \\ E_z \end{bmatrix} = 0. \tag{3.53}$$

For non-trivial results, the determinant must be zero,

$$\left(\omega^2 - i\omega V_a'^2\mu_0\sigma_p\right)\left(\omega^2 - i\omega V_a'^2\mu_0\sigma_p - V_a'^2k_x^2\right) - \left(\omega V_a'^2\mu_0\sigma_h\right)^2 = 0, \tag{3.54}$$

which is a fairly complex dispersion relation. For $\sigma_p \gg \sigma_h$, equation (3.53) reduces to two separate equations,

$$\left(-\omega^2 + i\omega V_a'^2 \mu_0 \sigma_p\right) \cdot E_x = 0 \tag{3.55}$$

$$\left(-\omega^2 + V_a'^2 \left(k_x^2 + i\omega\mu_0\sigma_p\right)\right) \cdot E_z = 0. \tag{3.56}$$

It is apparent that for $\sigma_p \gg \sigma_h$ waves propagating in the $\hat{\mathbf{x}}$ direction cannot be carried by E_x (there is no k_x dependence in 3.55). However, the non-trivial solution to equation (3.56),

$$\omega^2 - V_a'^2 \left(k_x^2 + i\omega\mu_0\sigma_p\right) = 0$$

$$\frac{\omega^2}{k_x^2} - i\frac{V_a'^2\mu_0\sigma_p}{k_x}\frac{\omega}{k_x} - V_a'^2 = 0$$

$$\frac{\omega}{k_x} = \frac{i\frac{V_a'^2\mu_0\sigma_p}{k_x} \pm \sqrt{\left(i\frac{V_a'^2\mu_0\sigma_p}{k_x}\right)^2 + 4V_a'^2}}{2}$$

$$\frac{\omega}{k_x} = \left[\pm\sqrt{1 - \left(\frac{V_a'\mu_0\sigma_p}{2k_x}\right)^2} + i\frac{V_a'\mu_0\sigma_p}{2k_x}\right] \cdot V_a', \tag{3.57}$$

describes a wave carried by E_z that propagates the speed of the real part of (3.57) and decays through finite σ_p (as seen by the imaginary part of 3.57). For $\sigma_h \gg \sigma_p$, equation (3.53) reduces to

$$\begin{bmatrix} -\omega^2 & i\omega V_a'^2\mu_0\sigma_h \\ -i\omega V_a'^2\mu_0\sigma_h & -\omega^2 + V_a'^2 k_x^2 \end{bmatrix} \cdot \begin{bmatrix} E_x \\ E_z \end{bmatrix} = 0, \tag{3.58}$$

When solving for non-trivial solutions,

$$-\omega^2\left(-\omega^2 + V_a'^2 k_x^2\right) - \left(i\omega V_a'^2\mu_0\sigma_h\right)\left(-i\omega V_a'^2\mu_0\sigma_h\right) = 0$$

$$\omega^4 - V_a'^2 k_x^2 \omega^2 - \left(\omega V_a'^2 \mu_0 \sigma_h\right)^2 = 0$$

$$\omega^2 = V_a'^2 k_x^2 + \left(V_a'^2 \mu_0 \sigma_h\right)^2$$

$$\frac{\omega^2}{k_x^2} = V_a'^2 + \left(\frac{V_a'^2 \mu_0 \sigma_h}{k_x}\right)^2$$

$$\frac{\omega}{k_x} = \pm\sqrt{V_a'^2 + \left(\frac{V_a'^2 \mu_0 \sigma_h}{k_x}\right)^2}$$

$$\frac{\omega}{k_x} = \pm\sqrt{1 + \left(\frac{V_a' \mu_0 \sigma_h}{k_x}\right)^2} \cdot V_a', \tag{3.59}$$

which describes the dispersion for a wave carried by E_x and E_z propagating in the $\hat{\mathbf{x}}$ direction (perpendicular to $\mathbf{B}$). Note that this wave is partially both a transverse and longitudinal wave. This wave is often referred to as the extraordinary wave or X wave. While the phase speed can exceed the speed of light when $V_a' \to c^2$, the group velocity,

$$\frac{d\omega}{dk_x} = \pm\frac{k_x}{\sqrt{k_x^2 + \left(V_a' \mu_0 \sigma_h\right)^2}} \cdot V_a', \tag{3.60}$$

cannot, considering that $V_a' \leq c^2$. Therefore information transmitted via X waves does not travel faster than light.

3.2.3 Finite Conductivity: Propagation parallel to B

Now let us consider the dispersion relation of waves in propagating parallel to $\mathbf{B}$ ($k_x = 0$) with finite conductivity. For $k_x = 0$, equation (3.38) becomes

$$\begin{bmatrix} -\omega^2 + V_a'^2\left(k_y^2 + i\omega\mu_0\sigma_p\right) & 0 & V_a'^2 i\omega\mu_0\sigma_h \\ 0 & -\omega^2 + i\omega c^2 \mu_0 \sigma_0 & 0 \\ -V_a'^2 i\omega\mu_0\sigma_h & 0 & -\omega^2 + V_a'^2\left(k_y^2 + i\omega\mu_0\sigma_p\right) \end{bmatrix} \cdot \mathbf{E} = 0. \tag{3.61}$$

It is apparent that E_y is decoupled from E_x and E_z. The dispersion relation for waves carried by E_y can be found by writing out the E_y equation from (3.50),

$$\left[-\omega^2 + i\omega c^2 \mu_0 \sigma_0\right] \cdot E_y = 0. \tag{3.62}$$

For non-trivial solutions,

$$\omega = ic^2 \mu_0 \sigma_0, \tag{3.63}$$

which describes a non-propagating wave that simply decays in finite σ_0. For waves carried by E_x and E_z, we reduce equation (3.61) to

$$\begin{bmatrix} -\omega^2 + V_a'^2\left(k_y^2 + i\omega\mu_0\sigma_p\right) & V_a'^2 i\omega\mu_0\sigma_h \\ -V_a'^2 i\omega\mu_0\sigma_h & -\omega^2 + V_a'^2\left(k_y^2 + i\omega\mu_0\sigma_p\right) \end{bmatrix} \cdot \begin{bmatrix} E_x \\ E_z \end{bmatrix} = 0. \tag{3.64}$$

For non-trivial results, the determinant must be zero,

$$\left[-\omega^2 + V_a'^2\left(k_y^2 + i\omega\mu_0\sigma_p\right)\right]^2 - \left[V_a'^2\omega\mu_0\sigma_h\right]^2 = 0. \tag{3.65}$$

Solving for the phase speed (ω/k_y) yields

$$\left[\omega^2 - V_a'^2\left(k_y^2 + i\omega\mu_0\sigma_p\right)\right]^2 = \left[V_a'^2\omega\mu_0\sigma_h\right]^2$$

$$\omega^2 - V_a'^2\left(k_y^2 + i\omega\mu_0\sigma_p\right) = \pm V_a'^2\omega\mu_0\sigma_h$$

$$\frac{\omega^2}{k_y^2} - \left[\frac{V_a'^2\mu_0\left(i\sigma_p \pm \sigma_h\right)}{k_y}\right]\frac{\omega}{k_y} - V_a'^2 = 0$$

$$\frac{\omega}{k_y} = \pm\sqrt{V_a'^2 + \frac{1}{4}\left[\frac{V_a'^2\mu_0\left(i\sigma_p \pm \sigma_h\right)}{k_y}\right]^2} + \frac{1}{2}\left[\frac{V_a'^2\mu_0\left(i\sigma_p \pm \sigma_h\right)}{k_y}\right]$$

$$\frac{\omega}{k_y} = \left[\pm \sqrt{1 + \left(\frac{V_a' \mu_0 \left(i\sigma_p \pm \sigma_h \right)}{2k_y} \right)^2} + \left(\frac{V_a' \mu_0 \left(i\sigma_p \pm \sigma_h \right)}{2k_y} \right) \right] \cdot V_a', \tag{3.66}$$

which is a fairly complicated dispersion relation that includes L, R, and Alfvén waves. In the regime where hall currents are negligible ($\sigma_h \ll \sigma_p$), the dispersion (3.66) becomes

$$\frac{\omega}{k_y} = \left[\pm \sqrt{1 - \left(\frac{V_a' \mu_0 \sigma_p}{2k_y} \right)^2} + i \left(\frac{V_a' \mu_0 \sigma_p}{2k_y} \right) \right] \cdot V_a', \tag{3.67}$$

which describes an Alfvén wave attenuated by finite σ_p. In the regime where Hall currents dominate ($\sigma_h \gg \sigma_p$), the dispersion (3.66) becomes

$$\frac{\omega}{k_y} = \pm \left[\sqrt{1 + \left(\frac{V_a' \mu_0 \sigma_h}{2k_y} \right)^2} \pm \left(\frac{V_a' \mu_0 \sigma_h}{2k_y} \right) \right] \cdot V_a', \tag{3.68}$$

which describes the L and R wave modes. Specifically, the L mode is described by

$$\frac{\omega}{k_y} = \pm \left[\sqrt{1 + \left(\frac{V_a' \mu_0 \sigma_h}{2k_y} \right)^2} + \left(\frac{V_a' \mu_0 \sigma_h}{2k_y} \right) \right] \cdot V_a', \tag{3.69}$$

and the R mode is described by

$$\frac{\omega}{k_y} = \pm \left[\sqrt{1 + \left(\frac{V_a' \mu_0 \sigma_h}{2k_y} \right)^2} - \left(\frac{V_a' \mu_0 \sigma_h}{2k_y} \right) \right] \cdot V_a'. \tag{3.70}$$

Note that the phase speed for both the L and R waves can exceed the speed of than light. However, the group speed,

$$\frac{\partial \omega}{\partial k_y} = \pm \frac{k_y}{\sqrt{k_y^2 + \left(\frac{V_a' \mu_0 \sigma_h}{2} \right)^2}} V_a', \tag{3.71}$$

remains below the speed of light. By inspection of equation (3.64), the L and R modes rely on the coupling of E_x and E_z via Hall currents.

At the limit where polarization and displacement currents are negligible (taking $V_a' \to \infty$), the R mode is sometimes referred to as the "whistler" mode. Recalling that $\sqrt{1+x^2} \simeq x + 1/(2x)$ for $x \gg 1$, then the R mode dispersion at at the limit where polarization and displacement current are negligible, (3.70) becomes

$$\frac{\omega}{k_y} = \pm \frac{k_y}{\mu_0 \sigma_h}, \tag{3.72}$$

The reason for the name "whistler," refers to that waves with higher k_y travel faster than waves with smaller k_y waves. Hence, when observing these waves at a distance, higher frequency waves are observed before lower frequency waves. A whistler pulse is observed as an initially high frequency tone that descends in frequency. The tones are reminiscent of whistling.

3.3 The significance of displacement currents

It is tempting to neglect displacement current, $\epsilon_0 \partial_t \mathbf{E}$, in Maxwell-Ampere's equation (3.4). Often it is negligible. However, it is essential in limiting wave speeds. Recall Maxwell-Faraday's and Maxwell-Ampere's law,

$$\partial_t \mathbf{B} = -\nabla \times \mathbf{E} \tag{3.73}$$

$$\partial_t \mathbf{E} = c^2 \left[\nabla \times \mathbf{B} - \mu_0 \mathbf{J}\right]. \tag{3.74}$$

Restricting our focus to the currents coupled with (3.73) and (3.74), for the purpose of the analysis in this section, the current density is

$$\mathbf{J} = \tilde{\boldsymbol{\sigma}} \mathbf{E}, \tag{3.75}$$

where we neglect ion inertia for simplicity. The tensor, $\tilde{\boldsymbol{\sigma}}$, is the conductivity tensor (2.15). To highlight the importance of displacement currents to the model, we derive the dispersion relation without displacement current ($\partial_t \mathbf{E} = 0$) which yield's the electrostatic Ampere's law,

$$\nabla \times \mathbf{B} = \mu_0 \mathbf{J}. \tag{3.76}$$

$\mathbf{E}$ can no longer be time integrated. However, it can be solved from $\mathbf{J}$ as

$$\mathbf{E} = \tilde{\boldsymbol{\sigma}}^{-1}\mathbf{J} = \tilde{\boldsymbol{\sigma}}^{-1}\frac{\nabla \times \mathbf{B}}{\mu_0}, \tag{3.77}$$

where $\mathbf{J} = \nabla \times \mathbf{B}$ from equation (3.76). Coupled with Maxwell-Ampere's law yields the following equation

$$\partial_t \mathbf{B} = -\nabla \times \mathbf{E} = -\nabla \times \left(\tilde{\boldsymbol{\sigma}}^{-1}\nabla \times \mathbf{B}\right). \tag{3.78}$$

Let us assume the plane wave solution ($\mathbf{B} \propto e^{i(\omega t - k_x x - k_y y - k_z z)}$) and express Ampere's law as

$$i\omega\mathbf{B} = -\begin{bmatrix} 0 & -ik_z & ik_y \\ ik_z & 0 & -ik_x \\ -ik_y & ik_x & 0 \end{bmatrix}\begin{bmatrix} \frac{\sigma_p}{\sigma_h^2+\sigma_p^2} & 0 & \frac{-\sigma_h}{\sigma_h^2+\sigma_p^2} \\ 0 & \frac{1}{\sigma_0} & 0 \\ \frac{\sigma_h}{\sigma_h^2+\sigma_p^2} & 0 & \frac{\sigma_p}{\sigma_h^2+\sigma_p^2} \end{bmatrix}\begin{bmatrix} 0 & -ik_z & ik_y \\ ik_z & 0 & -ik_x \\ -ik_y & ik_x & 0 \end{bmatrix}\frac{\mathbf{B}}{\mu_0}, \tag{3.79}$$

where we take x and z to be perpendicular to $\mathbf{B}$ and y to be parallel to $\mathbf{B}$. For wave propagation parallel to $\mathbf{B}$, equation (3.79) becomes

$$i\omega\mathbf{B} = -\begin{bmatrix} 0 & 0 & ik_y \\ 0 & 0 & 0 \\ -ik_y & 0 & 0 \end{bmatrix}\begin{bmatrix} \frac{\sigma_h}{\sigma_h^2+\sigma_p^2}ik_y & 0 & \frac{\sigma_p}{\sigma_h^2+\sigma_p^2}ik_y \\ 0 & 0 & 0 \\ -\frac{\sigma_p}{\sigma_h^2+\sigma_p^2}ik_y & 0 & \frac{\sigma_h}{\sigma_h^2+\sigma_p^2}ik_y \end{bmatrix}\frac{\mathbf{B}}{\mu_0}$$

$$i\omega\mathbf{B} = -\begin{bmatrix} \frac{\sigma_p}{\sigma_h^2+\sigma_p^2}k_y^2 & 0 & -\frac{\sigma_h}{\sigma_h^2+\sigma_p^2}k_y^2 \\ 0 & 0 & 0 \\ \frac{\sigma_h}{\sigma_h^2+\sigma_p^2}k_y^2 & 0 & \frac{\sigma_p}{\sigma_h^2+\sigma_p^2}k_y^2 \end{bmatrix}\frac{\mathbf{B}}{\mu_0}$$

$$\begin{bmatrix} i\omega + \frac{1}{\mu_0}\frac{\sigma_p}{\sigma_h^2+\sigma_p^2}k_y^2 & 0 & -\frac{1}{\mu_0}\frac{\sigma_h}{\sigma_h^2+\sigma_p^2}k_y^2 \\ 0 & i\omega & 0 \\ \frac{1}{\mu_0}\frac{\sigma_h}{\sigma_h^2+\sigma_p^2}k_y^2 & 0 & i\omega + \frac{1}{\mu_0}\frac{\sigma_p}{\sigma_h^2+\sigma_p^2}k_y^2 \end{bmatrix}\mathbf{B} = 0. \tag{3.80}$$

For non-trivial solutions, the determinant must be zero. Hence, we can derive the dispersion relation from the determinant of the matrix as

$$\left(i\omega + \frac{1}{\mu_0}\frac{\sigma_p}{\sigma_h^2+\sigma_p^2}k_y^2\right)^2 + \left(\frac{1}{\mu_0}\frac{\sigma_h}{\sigma_h^2+\sigma_p^2}k_y^2\right)^2 = 0$$

$$-\omega^2 + i\frac{2}{\mu_0}\frac{\sigma_p k_y^2}{\sigma_h^2+\sigma_p^2}\omega + \left(\frac{1}{\mu_0}\frac{\sigma_p}{\sigma_h^2+\sigma_p^2}k_y^2\right)^2 + \left(\frac{1}{\mu_0}\frac{\sigma_h}{\sigma_h^2+\sigma_p^2}k_y^2\right)^2 = 0$$

$$\omega^2 - i\frac{2\sigma_p k_y^2}{\mu_0\left(\sigma_h^2+\sigma_p^2\right)}\omega - \frac{k_y^4}{\mu_0^2\left(\sigma_h^2+\sigma_p^2\right)} = 0$$

$$\omega = i\frac{\sigma_p}{\mu_0\left(\sigma_h^2+\sigma_p^2\right)}k_y^2 \pm \sqrt{\frac{k_y^4}{\mu_0^2\left(\sigma_h^2+\sigma_p^2\right)} - \left(\frac{\sigma_p k_y^2}{\mu_0\left(\sigma_h^2+\sigma_p^2\right)}\right)^2}$$

$$\omega = i\frac{\sigma_p}{\mu_0\left(\sigma_h^2+\sigma_p^2\right)}k_y^2 \pm \frac{1}{\mu_0}k_y^2 \cdot \sqrt{\frac{1}{\sigma_h^2+\sigma_p^2} - \frac{\sigma_p^2}{\left(\sigma_h^2+\sigma_p^2\right)^2}}$$

$$\frac{\omega}{k_y} = i\frac{\sigma_p}{\mu_0\left(\sigma_h^2+\sigma_p^2\right)}k_y \pm \frac{\sigma_h}{\mu_0\left(\sigma_h^2+\sigma_p^2\right)}k_y. \tag{3.81}$$

Note that the phase speed (3.81) increases with k without limit, which makes numerical integration extremely stiff. However, the inclusion of $\partial_t\mathbf{E}$ saturates and limits the phase speed as seen by comparing equations (3.81) to (3.66).

3.4 Using Cowling conductivity

The problem with simulating full Hall dynamics is that when the Hall conductivity is significant, the X mode (3.59), L mode (3.69), and R mode (3.70) supported by EMI have extremely fast phase speeds that can exceed the speed of light and make the Courant condition (*Courant et al.*, 1967; *Press et al.*, 2007) more restrictive. Note that the X, L, and R mode dynamics are only important in the highly collisional regime where Hall conductivity is significant. In this highly collisional regime, the Alfvén wave speed saturates to the speed of light (see equations 3.28 and 3.29). Hence, in the context of resolving Alfvén dynamics, the X, L, and R mode dynamics are relatively instant and are effectively electrostatic. Treating Hall dynamics as electrostatic, we will discuss what is called the Cowling conductivity and how we can use it to stabilize numerical simulations that have significant Hall conductivity.

To derive the Cowling conductivity, we assume that in equatorial ionosphere, charges generally remain confined in a layer of plasma. It is assumed that currents do not diverge in the meridional direction, which we will define to be in the $\hat{\mathbf{z}}$ direction. Enforcing $\partial_z J_z = 0$ results in a different conductivity tensor that includes what is called the Cowling conductivity. Recall that the current driven by $\mathbf{E}$ is given by Pedersen, Hall, and parallel conductivities (2.15) such that

$$\mathbf{J} = \begin{bmatrix} \sigma_p & 0 & \sigma_h \\ 0 & \sigma_0 & 0 \\ -\sigma_h & 0 & \sigma_p \end{bmatrix} \cdot \mathbf{E}, \tag{3.82}$$

where the meridional current is

$$J_z = -\sigma_h E_x + \sigma_p E_z. \tag{3.83}$$

Enforcing $\partial_z J_z = 0$ yields the meridional electric field in terms of zonal electric field,

$$J_z = -\sigma_h E_x + \sigma_p E_z = 0$$

$$E_z = \frac{\sigma_h}{\sigma_p} E_x, \tag{3.84}$$

in a coordinate system where $\hat{\mathbf{x}}$ is in the zonal direction. In turn, E_z drives a hall current in the zonal direction. Consequently, the zonal current becomes

$$J_x = \sigma_p E_x + \sigma_h E_z = \sigma_c E_x, \tag{3.85}$$

where σ_c is the Cowling conductivity,

$$\sigma_c = \left(1 + \frac{\sigma_h^2}{\sigma_p^2}\right) \cdot \sigma_p. \tag{3.86}$$

The conductivity tensor with the Cowling conductivity can be expressed as

$$\tilde{\boldsymbol{\sigma}} = \begin{bmatrix} \sigma_c & 0 & 0 \\ 0 & \sigma_0 & 0 \\ -\sigma_h & 0 & \sigma_p \end{bmatrix}, \tag{3.87}$$

for a coordinate system where $\hat{\mathbf{x}}$ is zonal, $\hat{\mathbf{y}}$ is parallel to $\mathbf{B}$, and $\hat{\mathbf{z}}$ is meridional (in the direction of increasing L-shell).

By use of this alternative conductivity tensor, we will show that the troublesome X mode (3.59), L mode (3.69), and R mode (3.70) are no longer supported. Using the Cowling conductivity,

equation (3.37) becomes

$$\begin{bmatrix} -\omega^2 + V_a'^2\left(k_y^2 + k_z^2 + i\omega\mu_0\sigma_c\right) & V_a'^2\left(-k_xk_y\right) & 0 \\ c^2\left(-k_xk_y\right) & -\omega^2 + c^2\left(k_x^2 + k_z^2 + i\omega\mu_0\sigma_0\right) & c^2\left(-k_yk_z\right) \\ V_a'^2\left(-k_xk_z - i\omega\mu_0\sigma_h\right) & V_a'^2\left(-k_yk_z\right) & -\omega^2 + V_a'^2\left(k_x^2 + k_y^2 + i\omega\mu_0\sigma_p\right) \end{bmatrix} \cdot \mathbf{E} = 0. \tag{3.88}$$

For waves propagating parallel to $\mathbf{B}$ ($k_x = 0$, $k_y \neq 0$, $k_z = 0$) equation (3.88) becomes

$$\begin{bmatrix} -\omega^2 + V_a'^2\left(k_y^2 + i\omega\mu_0\sigma_c\right) & 0 & 0 \\ 0 & -\omega^2 + c^2 i\omega\mu_0\sigma_0 & 0 \\ -V_a'^2 i\omega\mu_0\sigma_h & 0 & -\omega^2 + V_a'^2\left(k_y^2 + i\omega\mu_0\sigma_p\right) \end{bmatrix} \cdot \mathbf{E} = 0. \tag{3.89}$$

It is apparent that E_y decoupled from E_x and E_z. The dispersion relation for waves carried by E_y can be found by writing out the E_y equation from (3.50),

$$\left[-\omega^2 + i\omega c^2\mu_0\sigma_0\right] \cdot E_y = 0. \tag{3.90}$$

For non-trivial solutions,

$$\omega = ic^2\mu_0\sigma_0, \tag{3.91}$$

which describes a non-propagating wave that simply decays in finite σ_0. For waves carried by E_x and E_z,

$$\left[-\omega^2 + V_a'^2\left(k_y^2 + i\omega\mu_0\sigma_c\right)\right]\left[-\omega^2 + V_a'^2\left(k_y^2 + i\omega\mu_0\sigma_p\right)\right] = 0. \tag{3.92}$$

Note that Hall currents play no role in the dispersion relation when the Cowling conductivity is used. While E_x is coupled into E_z, E_z is not coupled into E_x. Hence, there are no waves that is supported by the exchange of energy between E_x and E_z that is essential to the L and R modes. Waves that propagate parallel to $\mathbf{B}$ are instead solely carried by either E_x, or E_y. Waves carried

by E_x have the dispersion relation,

$$\omega^2 - V_a'^2\left(k_y^2 + i\omega\mu_0\sigma_c\right) = 0$$

$$\frac{\omega^2}{k_y^2} - \left(\frac{iV_a'^2\mu_0\sigma_c}{k_y}\right)\frac{\omega}{k_y} - V_a'^2 = 0$$

$$\frac{\omega}{k_y} = \frac{\frac{iV_a'^2\mu_0\sigma_c}{k_y} \pm \sqrt{\left(\frac{iV_a'\mu_0\sigma_c}{k_y}\right)^2 + 4V_a'^2}}{2}$$

$$\frac{\omega}{k_y} = \left[\pm\sqrt{1 - \left(\frac{V_a'\mu_0\sigma_c}{2k_y}\right)^2} + i\frac{V_a'\mu_0\sigma_c}{2k_y}\right]\cdot V_a'. \tag{3.93}$$

Similarly, waves carried by E_z have the dispersion relation,

$$\frac{\omega}{k_y} = \left[\pm\sqrt{1 - \left(\frac{V_a'\mu_0\sigma_p}{2k_y}\right)^2} + i\frac{V_a'\mu_0\sigma_p}{2k_y}\right]\cdot V_a'. \tag{3.94}$$

For both (3.93) and (3.94), the fastest phase speed does not exceed V_a' and hence does not exceed the speed of light, unlike with the L and R mode dispersion (3.68). Using the Cowling conductivity shorts out the L and R modes, reduces the maximum phase speed, and reduces the stiffness of the model making for more stable numerical simulations.

For waves propagating perpendicular to $\mathbf{B}$ ($k_y = 0$), equation (3.88) becomes

$$\begin{bmatrix} -\omega^2 + V_a'^2\left(k_z^2 + i\omega\mu_0\sigma_c\right) & 0 & 0 \\ 0 & -\omega^2 + c^2\left(k_x^2 + k_z^2 + i\omega\mu_0\sigma_0\right) & 0 \\ V_a'^2\left(-k_xk_z - i\omega\mu_0\sigma_h\right) & 0 & -\omega^2 + V_a'^2\left(k_x^2 + i\omega\mu_0\sigma_p\right) \end{bmatrix}\cdot\mathbf{E} = 0. \tag{3.95}$$

For the same reasons the dispersion relation (3.89) was independent of σ_h, (3.95) is also independent of σ_h. While E_x is coupled into E_z, E_z is not coupled into E_x. Hence, there are no waves that is

supported by the exchange of energy between E_x and E_z. Waves propagating perpendicular to $\mathbf{B}$ are only carried solely by E_x, E_y, or E_z, with the wave dispersion relations,

$$\frac{\omega}{k_z} = \left[\pm \sqrt{1 - \left(\frac{V_a' \mu_0 \sigma_c}{2k_z} \right)^2} + i \frac{V_a' \mu_0 \sigma_c}{2k_z} \right] \cdot V_a' \tag{3.96}$$

$$\frac{\omega}{\sqrt{k_x^2 + k_z^2}} = \left[\pm \sqrt{1 - \left(\frac{c \mu_0 \sigma_0}{2\sqrt{k_x^2 + k_z^2}} \right)^2} + i \frac{c \mu_0 \sigma_0}{2\sqrt{k_x^2 + k_z^2}} \right] \cdot c \tag{3.97}$$

$$\frac{\omega}{k_x} = \left[\pm \sqrt{1 - \left(\frac{V_a' \mu_0 \sigma_p}{2k_x} \right)^2} + i \frac{V_a' \mu_0 \sigma_p}{2k_x} \right] \cdot V_a', \tag{3.98}$$

respectively. For each dispersion, the phase speed does not exceed the speed of light unlike the X mode (3.59). Using the Cowling conductivity shorts out X mode, reduces the maximum phase speed, and reduces the stiffness of the model making for more stable numerical simulations.

The implication of using the Cowling conductivity is that you sacrifice full Hall dynamics. As shown, the L an R waves and X mode waves are no longer supported. However, these phenomenon only happen in the E region where the plasma is highly collisional and the effective Alfvén speed (3.28) is saturated to the speed of light. In an interest of much slower Alfvén dynamics in the F region, Hall dynamics happen relatively instantly. In this case, the use of the Cowling conductivity is warranted.

3.5 Reducing the speed of light

One of the numerical challenges in integrating Maxwell's equations is that equation (3.21) is numerically stiff due to the large c^2 factor applied to the parallel component. In low conductivity regions, the coupling of equation (3.20) to the parallel component of (3.21) includes light wave modes carried by $\mathbf{E}_{\parallel}$ that propagate in the plane perpendicular to $\mathbf{B}_0$ at speed c. The stiffness is remedied by

reducing the speed of light to 10^7 m/s , which is still much faster than the typical Alfvén speed in the ionosphere ($\sim 10^5$ m/s). Despite the reduced speed, light wave dynamics still reach a steady state relatively instantly with respect to the Alfvén dynamics of interest. Keep in mind that the steady-state solution remains unchanged regardless of the speed of light. For the perpendicular term, we maintain the true speed of light. Lowering the numerical speed of light would distort the $c^2V_a^2/\left(c^2+V_a^2\right)$ factor in equation (3.21) for Alfvén speeds that approach the new speed of light. Not only will the wave speed be inaccurate at low ion density regions, but it can also significantly affect the reflection coefficient between low and high Alfvén speed regions. Hence, we maintain the real speed of light for the $c^2V_a^2/\left(c^2+V_a^2\right)$ factor. Fortunately, in the ionosphere, $V_a^2 \ll c^2$ and naturally reduces the numerical stiffness.

3.6 Background conditions

We model the background ionosphere with the 2007 International Reference Ionosphere (IRI-2007) model (*Bilitza and Reinisch*, 2008) for ion density, ion composition, ion temperature, and electron temperature. Modeled are the densities for O^+, H^+, He^+, O_2^+, and NO^+ as well as the ion and electron temperatures. Below, plotted is the ion density on a log scale versus altitude and magnetic latitude. The density profile at the equator is shown on the right subplot. The F peak is at around 250 km and the E layer is at around 100 km.

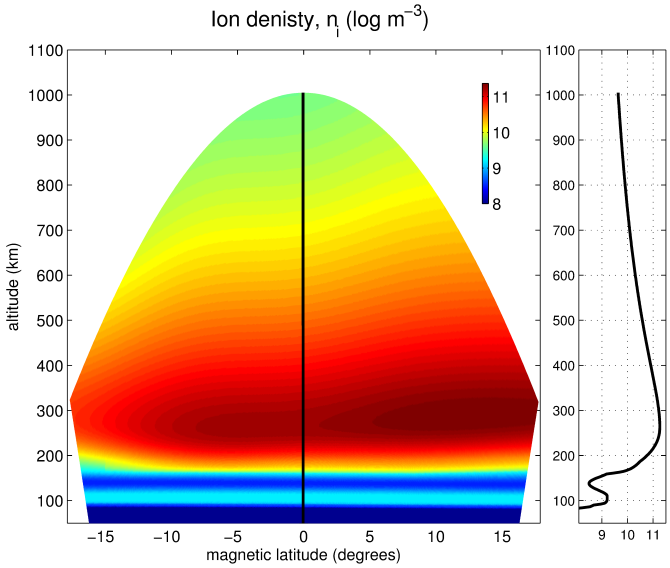

Figure 3.3: Left, the background ion density (on a log scale) as derived modeled by IRI-2007. The density at the vertical black line is plotted on the right.

Shown in the next two plots, are the ion temperature and electron temperatures versus altitude and magnetic latitude. The subplot on the right of each respective figure shows the temperatures at the magnetic equator. In this case, ion and electron temperatures are similar. The ion temperature monotonically increases from $\sim$ 200 K to $\sim$ 900 K with altitude. The electron temperature monotonically increases from $\sim$ 200 K to $\sim$ 1000 K with altitude.

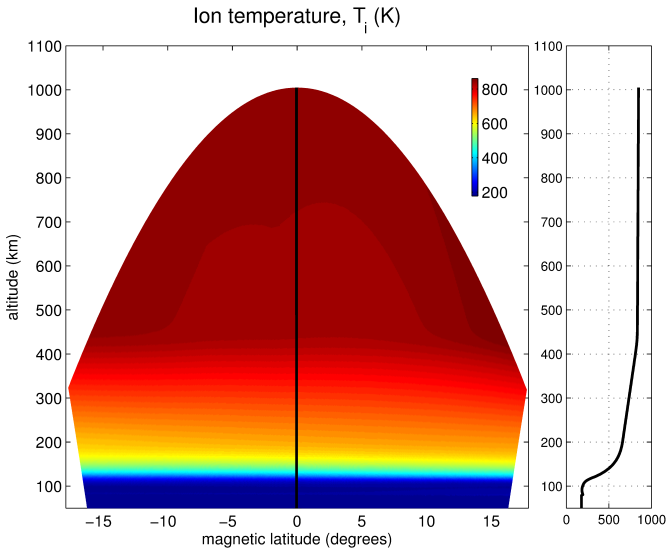

Figure 3.4: The ion temperature (in kelvins) as modeled from IRI-2007. The temperature at the vertical black line is plotted on the right.

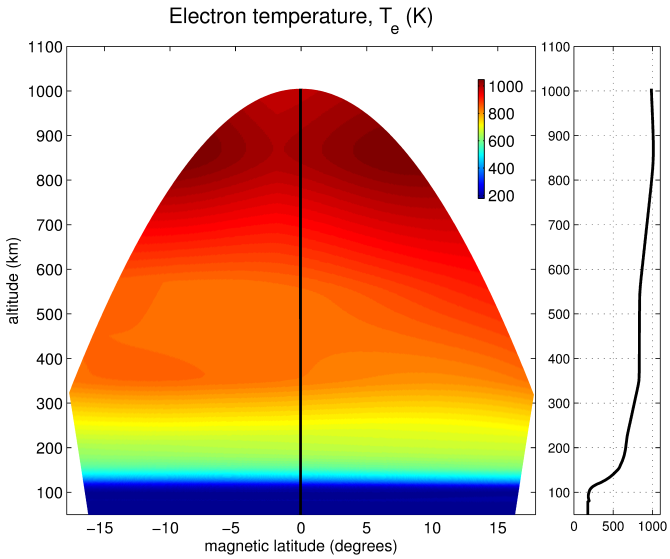

Figure 3.5: The electron temperature (in kelvins) as modeled from IRI-2007. The temperature at the vertical black line is plotted on the right.

We use the NRLMSISE-00 model (*Picone et al.*, 2002) for neutral densities and composition.

Modeled in NRLMSISE-00 are the densities for He, O, N_2, O_2, Ar, H, and N, which are plotted below. Below 100 km, N_2 and O_2 dominate. Between 250 km and 450 km, O dominates. Above 600 km, He and H dominate. The total neutral density is very high at low altitudes, where plasmas will collide with neutrals more frequently and become collisional.

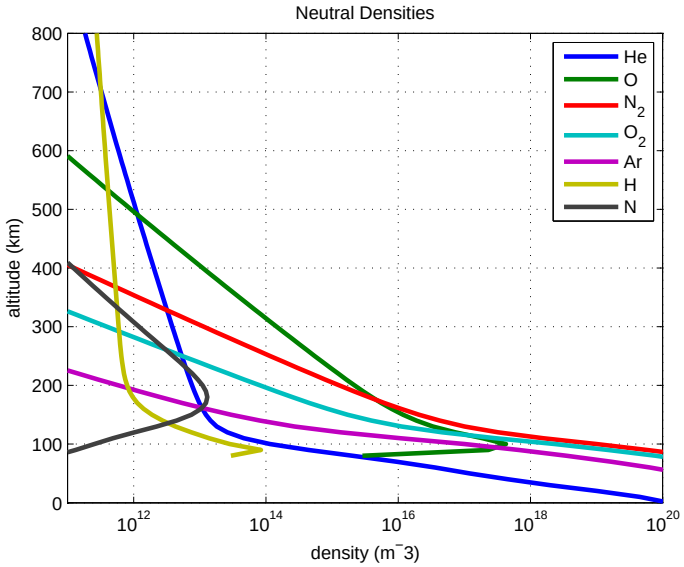

Figure 3.6: Densities of He, O, N_2, O_2, Ar, H, and N versus altitude.

3.7 Collision rates and conductivities

From the ion densities and plasma temperatures and the neutral densities, we compute the ion-neutral, ion-electron, ion, electron-neutral, electron-ion, and electron collision frequencies using

formulas from *Kelley* (2009),

$$\nu_{in} = \left(2.6 \times 10^{-9}\right)\left(n_n A_n^{-1/2} + n_i A_i^{-1/2}\right)\ \mathrm{s}^{-1} \tag{3.99}$$

$$\nu_{ie} = 0\ \mathrm{s}^{-1} \tag{3.100}$$

$$\nu_i = \nu_{in} + \nu_{ie} \tag{3.101}$$

$$\nu_{en} = \left(5.4 \times 10^{-10}\right) n_n T_e^{1/2}\ \mathrm{s}^{-1} \tag{3.102}$$

$$\nu_{ei} = \left(34 + 4.18 \cdot \ln\left(T_e^3/n_e\right)\right) n_n T_e^{-3/2}\ \mathrm{s}^{-1} \tag{3.103}$$

$$\nu_e = \nu_{en} + \nu_{ei}, \tag{3.104}$$

where n_n is neutral density in reciprocal cubic centimeters, n_i is ion density in reciprocal cubic centimeters, A_n is the dimensionless mean molecular mass of the neutrals, A_i is the dimensionless mean molecular mass of the ions, and T_e is the electron temperature in kelvins. Both ν_i and ν_e for the background ionosphere are plotted below.

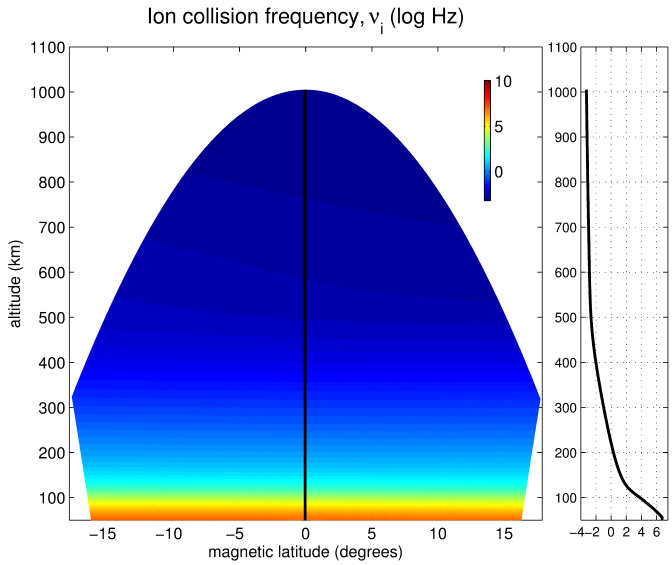

Figure 3.7: The ion collision frequency (on a log scale) derived from both IRI-2007 ions and NRLMSISE-00 neutrals. The collision frequency at the vertical black line is plotted on the right.

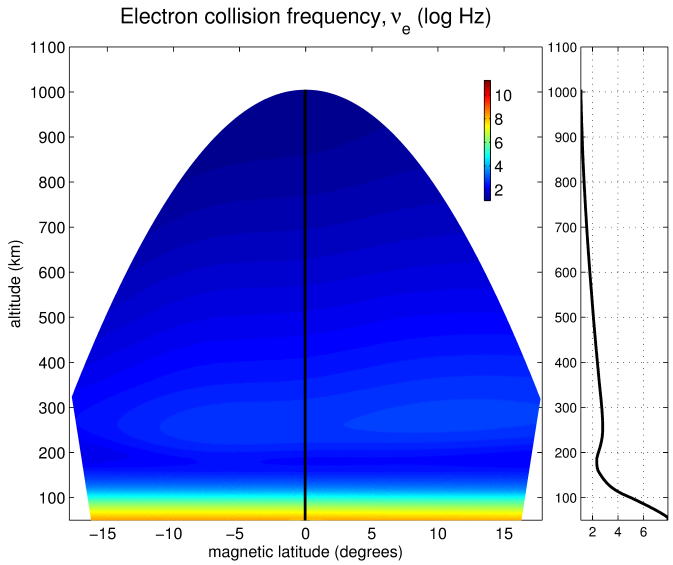

Figure 3.8: The electron collision frequency (on a log scale) as derived from IRI-2007 ions and NRLMSISE-00 neutrals. The collision frequency at the vertical black line is plotted on the right.

Computing the collision rates allow us to also compute the specific, Pedersen, and Hall conductivities from (2.15),

$$\begin{aligned}
\sigma_0 =& e^2 n_e \left(\frac{1}{m\nu_e} + \frac{1}{M\nu_i} \right) \\
\sigma_p =& e^2 n_e \left(\frac{\nu_e}{m\left(\nu_e^2 + \Omega_e^2\right)} + \frac{\nu_i}{M\left(\nu_i^2 + \Omega_i^2\right)} \right) \\
\sigma_h =& e^2 n_e \left(\frac{|\Omega_e|}{m\left(\nu_e^2 + \Omega_e^2\right)} - \frac{\Omega_i}{M\left(\nu_i^2 + \Omega_i^2\right)} \right),
\end{aligned} \tag{3.105}$$

These conductivities for the background conditions presented are shown below:

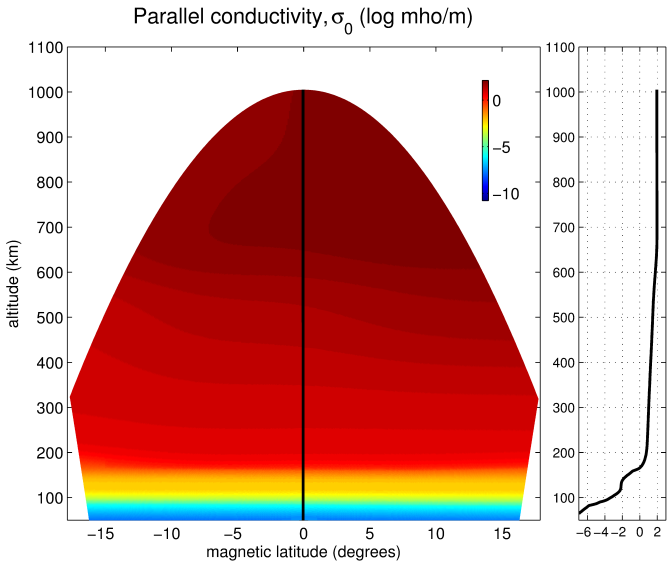

Figure 3.9: The parallel conductivity (on a log scale). The conductivity at the vertical black line is plotted on the right.

Ranging between 10 to 10^2 mho/m, the parallel conductivity, σ_0, is very high above 160 km. Below 160 km, the tandem of decreasing electron density and increasing electron collisions decreases the parallel conductivity sharply by several orders of magnitude.

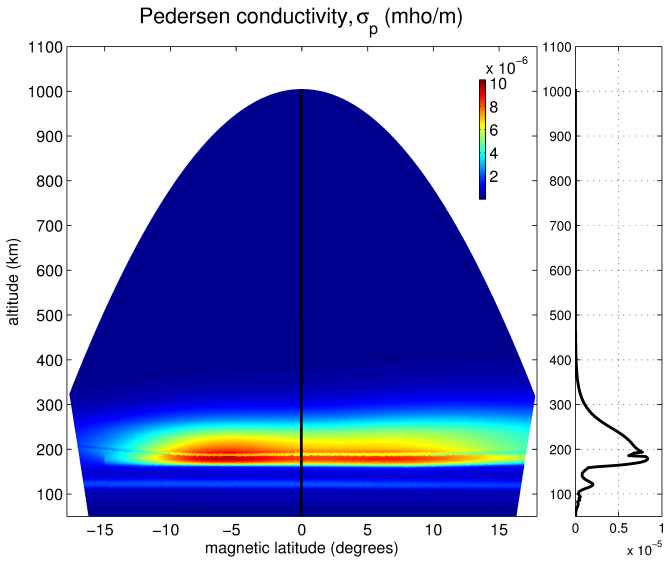

Figure 3.10: The Pedersen conductivity. The conductivity at the vertical black line is plotted on the right.

The Pedersen conductivity, σ_p, maximizes to 8×10^{-4} mhos/m at around 190 km altitude, where the ion collision frequency, ν_i, is high but does not exceed the gyro frequency, $\Omega_i \sim 100$ Hz.

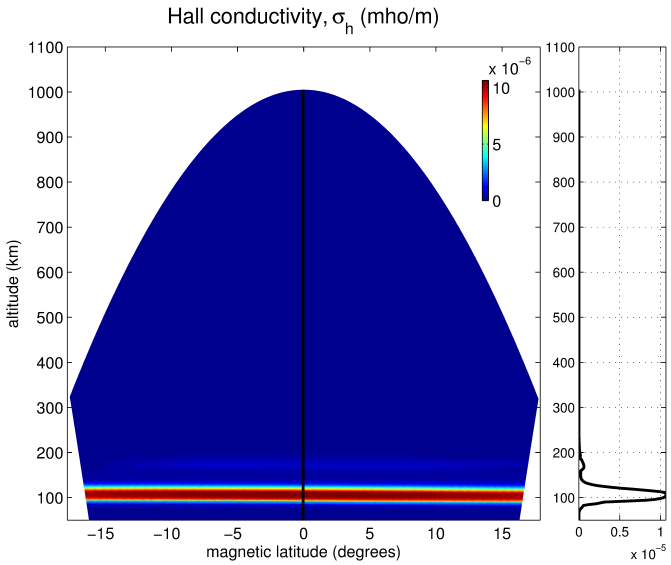

Figure 3.11: The Hall conductivity. The conductivity at the vertical black line is plotted on the right.

The Hall conductivity, σ_h, maximizes to $\sim 10^{-5}$ mho/m at around 100 km where the ions are extremely collisional ($\nu_i \gg \Omega_i$), but where electrons are not collisional ($\nu_e \ll \Omega_e$).

Chapter 4

Numerical methods

Integration of $\mathbf{E}$, $\mathbf{B}$, and n_i described by equations (3.20), (3.21) and (3.22), respectively, is done using many of the advanced finite-volume methods that were previously used in the PERSEUS model (*Seyler and Martin*, 2011), an electromagnetic extended-MHD plasma model. For each flux term, EMI uses a Rusanov scheme with Van Leer flux limiting second order corrections (*Trac and Pen*, 2002). In conjunction with the flux limiting, EMI maintains zero divergent curls in equations (3.20) and (3.21) with a flux-interpolated central-difference scheme outlined by *Toth* (2000). EMI uses Richardson extrapolation for second-order time accuracy. The result is that EMI is second-order accurate, both spatially and temporally. This chapter will go into the details of the numerical methods used to integrate equations (3.20), (3.21) and (3.22).

4.1 Curvilinear dipole grid

We simulate on a grid uniform in dipole coordinates. We will define the x, y, and z coordinates as magnetic zonal, north, and meridional, respectively. Earth's magnetic field strength can be modeled

with that of a dipole magnetic field (*Schunk and Nagy*, 2004),

$$|\mathbf{B}_0| \propto \frac{\sqrt{1+3\cos^2\theta}}{r^3}, \tag{4.1}$$

where θ is the magnetic co-latitude and r is the distance away from the center of Earth,

$$r = R_0 \sin^2\theta, \tag{4.2}$$

where R_0 is the distance away from the center of the Earth at the magnetic equator ($\theta = \pi/2$). We define x as the magnetic longitude in radians. Coordinate y is expressed as

$$y = \cos(\theta) \cdot \left(\frac{R_E}{r}\right)^2, \tag{4.3}$$

where R_E is Earth's radius (~ 6378.1 km) . Coordinate y is a unitless coordinate that corresponds to a position on a unique dipole magnetic field line, where $y = 0$ is at the magnetic equator and the direction of increasing y is parallel to $\mathbf{B}_0$. Coordinate z is expressed as

$$z = \frac{r/R_e}{\sin^2\theta} = \frac{R_0}{R_E}, \tag{4.4}$$

where z increases with increasing L-shell or McIlwain L-parameter. Together, coordinates x, y, and z form an orthogonal curvilinear coordinate system (*Feshbach*, 1953). Given by *Orens et al.* (1979), the scale factors for this curvilinear coordinate system are

$$h_x = r \cdot \sin\theta \tag{4.5}$$

$$h_y = \frac{r^3}{R_E^2\sqrt{1+3\cos^2\theta}} \tag{4.6}$$

$$h_z = \frac{R_E \sin^3\theta}{\sqrt{1+3\cos^2\theta}}, \tag{4.7}$$

for the x, y, and z coordinates, respectively.

Note that the scaling factors (4.5), (4.6), and (4.7) are in terms of r and θ. However, since we work in x, y, and z coordinates, it useful to solve θ and r as a function of x, y, and/or z. While y can be written in terms of θ and z as

$$y = \cos(\theta) \cdot \left(\frac{R_E}{R_0 \sin^2 \theta} \right)^2 = \frac{\cos(\theta)}{z^2 \cdot \sin^4 \theta}, \tag{4.8}$$

solving for θ thereafter is analytically challenging. Instead of solving for θ analytically, we use the Newton-Raphson method (*Press et al.*, 2007) to solve for θ to machine precision. A good initial guess for θ at low latitudes can be made by taking first-order Taylor expansions near $\theta = \pi/2$ (near the magnetic equator) of cosine and sine in equation (4.8),

$$y = \frac{\cos(\theta)}{z^2 \cdot \sin^4 \theta} \approx \frac{\pi/2 - \theta}{z^2}, \tag{4.9}$$

and then solving for θ,

$$\theta^{(n=0)} = \frac{\pi}{2} - yz^2, \tag{4.10}$$

where θ^n is the n^{th} iteration in the Newton-Raphson solution. By the Newton-Raphson method, θ is iteratively solved as

$$\theta^{n+1} = \theta^n - \frac{f(\theta)}{\partial_\theta f(\theta)} = \theta^n - \frac{yz^2 - \frac{\cos(\theta^n)}{\sin^4(\theta^n)}}{\frac{1+3\cos^2(\theta^n)}{\sin^5(\theta^n)}}, \tag{4.11}$$

where $f(\theta) = yz^2 - \cos(\theta) / \sin^4(\theta)$ is the function of which we wish to find the root. Equation (4.11) is iterated until θ converges. The value at which θ converges to is an accurate numerical function evaluation of $\theta(y, z)$. In turn, r is trivially evaluated as

$$r(z, \theta) = R_E z \cdot \sin^2 \theta. \tag{4.12}$$

With both $\theta(y,z)$ and $r(z,\theta)$, we can compute the scaling factors, equations (4.5), (4.6), and (4.7), given (y,z) coordinates. It is apparent that θ and r are independent of x.

4.2 First-order spatial accuracy: Rusanov scheme

EMI utilizes a Rusanov scheme for a stable first-order integration of flux equations which will be made second-order accurate in Section 4.3. First, is instructive to show that simple finite differencing is unstable when integrating flux equations. Let us interrogate the general one-dimensional flux equation,

$$\partial_t U = -\partial_x F, \tag{4.13}$$

where U is the parameter we wish to integrate, ∂_t denotes the partial time derivative, ∂_x denotes the spacial derivative, and F is the flux of U. For simplicity's sake, we only consider one spatial dimension which can be easily used in higher-dimension schemes discussed later. One may be tempted to integrate (4.13) with simple finite differencing between cells such as central differencing,

$$\frac{U_j^{n+1} - U_j^n}{h} = -\frac{F_{j+1}^n - F_{j-1}^n}{2L}.$$

$$U_j^{n+1} = U_j^n - \frac{h}{L}\frac{F_{j+1}^n - F_{j-1}^n}{2}, \tag{4.14}$$

where h is the time step we wish to integrate and L is the distance between cell centers. The ^{n} superscript indicates the nth iteration in time. The $_j$ subscript indicates the value at the jth cell in space. Performing the Von Neumann stability analysis, we take U and F to take the form,

$$U \propto F \propto e^{i(jkL)}. \tag{4.15}$$

In other words, we take U and F to be arbitrary Fourier components corresponding to an arbitrary wave-number, k. In order to analyze whether U_j^{n+1} is iteratively stable, we solve (4.14) for the ratio of consecutive iterations of U,

$$\frac{U_j^{n+1}}{U_j^n} = 1 - \frac{h}{L}\left(\frac{1}{U_j^n} \cdot \frac{F_{j+1}^n - F_{j-1}^n}{2}\right). \tag{4.16}$$

Substituting U and F with relation (4.15) yields

$$\frac{U_j^{n+1}}{U_j^n} = 1 - \frac{h}{L}\left(\frac{F}{U} \cdot \frac{e^{ikL} - e^{-ikL}}{2}\right)$$

$$\frac{U_j^{n+1}}{U_j^n} = 1 - i\frac{F}{U}\frac{h}{L}\sin(kL), \tag{4.17}$$

which has a modulus greater than 1, indicating that the iterative process grows unconditionally. This shows that integrating flux equations with finite differencing is simply unstable and will grow out of control.

EMI utilizes the following Rusanov scheme for integrating flux equations that introduces artificial diffusion that maintains stability. Equation (4.13) becomes

$$\partial_t U = -\partial_L F + D_{artificial}\partial_L^2 U, \tag{4.18}$$

where $D_{artificial}$ is an artificial diffusion coefficient. Analogous to equation (4.14), equation (4.18) is integrated as

$$\frac{U_j^{n+1} - U_j^n}{h} = -\frac{F_{j-1}^n - F_{j+1}^n}{2L} + c_f\frac{U_{j+1}^n - 2U_j^n + U_{j-1}^n}{2L},$$

$$U_j^{n+1} = U_j^n - h \cdot \left(\frac{F_{j-1}^n - F_{j+1}^n}{2L} - c_f\frac{U_{j+1}^n - 2U_j^n + U_{j-1}^n}{2L}\right), \tag{4.19}$$

where c_f is an auxiliary variable referred to as the freezing speed and defined as $c_f \equiv 2D_{artificial}/L$.

As one can see, the freezing speed is directly related to the artificial diffusion. However, using freezing speed instead of $D_{artificial}$ allows for easier-to-read formulation and matches the form of *Jin and Xin* (1995). Performing the Von Neumann stability analysis on the Rusanov Scheme (4.19) where we substitute the relation (4.15) yields

$$\frac{U_j^{n+1}}{U_j^n} = 1 - \frac{h}{U_j^n} \cdot \left(\frac{F_{j-1}^n - F_{j+1}^n}{2L} - c_f \frac{U_{j+1}^n - 2U_j^n + U_{j-1}^n}{2L} \right)$$

$$\frac{U_j^{n+1}}{U_j^n} = 1 - \frac{h}{L} \left(\frac{F}{U} \frac{e^{ikL} - e^{-ikL}}{2} - c_f \frac{e^{ikL} - 2 + e^{-ikL}}{2} \right)$$

$$\frac{U_j^{n+1}}{U_j^n} = 1 - \frac{h}{L} \left[i \frac{F}{U} \cdot \sin(kL) + c_f (1 - \cos(kL)) \right]. \tag{4.20}$$

For stability, the modulus of equation (4.20) must be less than or equal to one. Thus,

$$\left| \frac{U_j^{n+1}}{U_j^n} \right|^2 = \left[1 - \frac{h}{L} c_f (1 - \cos(kL)) \right]^2 + \left[\frac{h}{L} \frac{F}{U} \cdot \sin(kL) \right]^2 \leq 1$$

$$-2\frac{h}{L} c_f (1 - \cos(kL)) + \left[\frac{h}{L} c_f (1 - \cos(kL)) \right]^2 + \left[\frac{h}{L} \frac{F}{U} \cdot \sin(kL) \right]^2 \leq 0$$

$$-2\frac{h}{L} c_f + \left[\frac{h}{L} c_f \right]^2 (1 - \cos(kL)) + \frac{\left[\frac{h}{L} \frac{F}{U} \cdot \sin(kL) \right]^2}{1 - \cos(kL)} \leq 0$$

$$\left[\frac{h}{L} c_f \right]^2 (1 - \cos(kL)) + \left[\frac{h}{L} \frac{F}{U} \right]^2 \frac{\sin^2(kL)}{1 - \cos(kL)} \leq 2\frac{h}{L} c_f$$

$$\left[\frac{h}{L} c_f \right]^2 (1 - \cos(kL)) + \left[\frac{h}{L} \frac{F}{U} \right]^2 \frac{1 - \cos^2(kL)}{1 - \cos(kL)} \leq 2\frac{h}{L} c_f$$

$$\left[\frac{h}{L} c_f \right]^2 (1 - \cos(kL)) + \left[\frac{h}{L} \frac{F}{U} \right]^2 (1 + \cos(kL)) \leq 2\frac{h}{L} c_f$$

$$c_f^2 (1 - \cos(kL)) + \left[\frac{F}{U} \right]^2 (1 + \cos(kL)) \leq 2\frac{L}{h} c_f$$

$$\left(\left[\frac{F}{U}\right]^2 + c_f^2\right) + \cos(kL) \cdot \left(\left[\frac{F}{U}\right]^2 - c_f^2\right) \leq 2\frac{L}{h}c_f. \tag{4.21}$$

Only a certain range of c_f will result in stability. The left-hand side is at a maximum when $\cos(kL) = 1$ or $\cos(kL) = -1$. For $\cos(kL) = -1$, the inequality,

$$\left(\left[\frac{F}{U}\right]^2 + c_f^2\right) - \left(\left[\frac{F}{U}\right]^2 - c_f^2\right) \leq 2\frac{L}{h}c_f$$

$$c_f \leq \frac{L}{h}, \tag{4.22}$$

is required for stability. This is essentially the Courant condition for the freezing speed, c_f, where the artificial diffusion associated with c_f, must not transverse beyond it's neighboring cells for each time step, h. Turning our attention back to equation (4.21), the inequality for $\cos(kL) = 1$,

$$\left(\left[\frac{F}{U}\right]^2 + c_f^2\right) + \left(\left[\frac{F}{U}\right]^2 - c_f^2\right) \leq 2\frac{L}{h}c_f$$

$$c_f\frac{L}{h} > \left[\frac{F}{U}\right]^2, \tag{4.23}$$

is required for stability. Using the lower limit for L/h from inequality (4.22) and generalizing c_f for the whole simulation space, inequality (4.23) becomes

$$c_f^2 > max\left(\left[\frac{F}{U}\right]^2\right)$$

$$c_f > max\left|\frac{F}{U}\right|, \tag{4.24}$$

where max refers to the maximum value of its argument in the simulation space. In the context of the continuity equation (3.22), $F/U = v_i$ and inequality (4.24) becomes $c_f > max|v_i|$. In other words, the freezing speed for the continuity equation must be greater than the maximum

ion velocity for stability. In the context of Maxwell-Faraday's law (3.20) and Maxwell-Ampere's law (3.21), $c_f > max\,|\omega/k|$. In other words, the freezing speed must exceed the maximum phase speed for stability. For EMI, the fastest phase speeds are that of the X mode (3.59) and the L and R modes (3.68). In fact, the continuity equation's v_i is also the phase speed for the continuity equation. Hence, it can be generally stated that the freezing speed must exceed the phase speed for stability for any of the flux equations,

$$c_f > max\left|\frac{\omega}{k}\right|. \tag{4.25}$$

Inequality (4.25) is consistent with c_f conditions found in *Jin and Xin* (1995) and *Trac and Pen* (2002). While the freezing speed can be chosen arbitrarily large to satisfy inequality (4.25), we wish to use the minimum freezing speed, to minimize the artificial diffusion. We also must keep in mind that the freezing speed is bounded by the Courant condition (4.22). Note that inequality (4.25) is easier to satisfy when using the Cowling conductivity in Section 3.4, because the maximum phase speeds are slower than that of the X, L, and R modes.

4.3 Second-order spatial accuracy: MUSCL scheme

One of the numerical challenges of finite volume methods is that first-order differencing is artificially diffusive and cannot model shocks effectively. The Rusanov scheme in Section 4.2 is no exception considering the artificial diffusion used to maintain stability. However, there are several higher-order methods that limit numerical diffusivity and preserve shocks. We implement a monotone upwind schemes for conservation laws (MUSCL) scheme as outlined by *Trac and Pen* (2002) to obtain second-order spacial accuracy that is monotonicity preserving. For simplicity sake, we assume

regular grid spacing. Recall that the one-dimensional flux equation takes the form,

$$\partial_t U = -\partial_x F. \tag{4.26}$$

We can split up the flux into a right moving flux (F^R) and a left moving flux (F^R) as

$$F_{i+1/2} = \frac{F^R_{i+1/2} - F^L_{i+1/2}}{2}, \tag{4.27}$$

where

$$F^R_{i+1/2} = c_f U_i + F_i \tag{4.28}$$

$$F^L_{i+1/2} = c_f U_{i+1} - F_{i+1}, \tag{4.29}$$

and c_f is the freezing speed (see Section 4.2). Equation (4.27) actually implements the Rusanov scheme exactly. Note that cell wall fluxes (4.28) and (4.29) are comprised of cell centered value whereas we are interested in the flux at the cell wall. We make second-order corrections to $F^R_{i+1/2}$ and $F^L_{i+1/2}$ by extrapolating their right-hand side (which each is composed of cell centered values) to the cell wall at $i+1/2$. For extrapolation, we can either use the finite-difference slope at the cell wall of interest or the finite-difference slope at the upwind cell wall. The upwind slope is a natural choice because it makes use of information from where the moving flux travels, a key feature of monotone upwind schemes for conservation laws (MUSCL) (*Van Leer*, 1979). However, this upwind flux slope must be compared to the local slope and limited in order to preserve monotonicity. The MUSCL scheme is expressed as

$$F^*_{i+1/2}(U) = \frac{F^{R,*}_{i+1/2} - F^{L,*}_{i+1/2}}{2} \tag{4.30}$$

$$F^{R,*}_{i+1/2} = F^R_{i+1/2} + \phi\left(\frac{F^R_i - F^R_{i-1}}{2}, \frac{F^R_{i+1} - F^R_i}{2}\right) \tag{4.31}$$

$$F_{i+1/2}^{L,*} = F_{i+1/2}^{L} + \phi\left(\frac{F_i^L - F_{i+1}^L}{2}, \frac{F_{i+1}^L - F_{i+2}^L}{2}\right), \tag{4.32}$$

where we denote the second-order corrected flux with * and ϕ is a flux limiting function that compares the upwind slope with the slope at the $i+1/2$ cell wall. Flux limiting functions takes the two flux slopes and rectifies the more extreme slope for monotonicity preservation. A few flux limiting equations are presented in *Trac and Pen* (2002). We use the Van Leer flux limiter (*Van Leer*, 1974),

$$\phi(a,b) = \begin{cases} \frac{2ab}{a+b} & \text{if } ab>0, \\ 0 & \text{otherwise,} \end{cases} \tag{4.33}$$

which preserves monotonicity and provides second-order spatial accuracy.

We generalize the flux limiting for irregular grid spacing by introducing scaling discussed in *Berger et al.* (2005). Consider an irregular grid spacing as illustrated in the diagram below. Fluxes (F) can correspond with cells with different cell lengths (L).

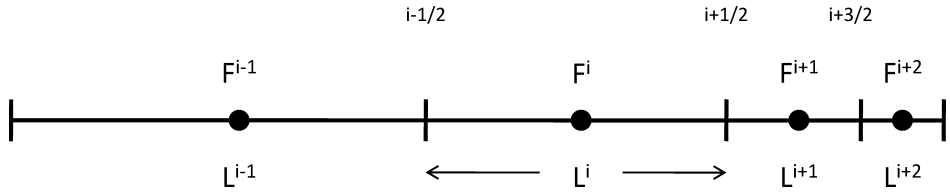

Figure 4.1: Fluxes on an irregular grid.

For equation (4.31), the difference at the $i+1/2^{th}$ cell wall is compared to that of the $i-1/2^{th}$ cell wall as a proxies for the derivatives at the respective cell wall. This is fine for regularly spaced cell spacing. However, for irregular spacing, this cannot be done because the derivatives at the $i+1/2^{th}$ and $i-1/2^{th}$ cell wall are

$$\frac{\partial F}{\partial x}^{i+1/2} = \frac{F^{i+1} - F^i}{\left(L^i + L^{i+1}\right)/2} \tag{4.34}$$

and

$$\frac{\partial F}{\partial x}^{i-1/2} = \frac{F^i - F^{i-1}}{\left(L^{i-1} + L^i\right)/2}, \tag{4.35}$$

respectively. For irregular grid spacing, simply comparing differences of F at the cell walls does not adequately compare the derivatives. This is because the difference of F is essentially a derivative with respect to i which is not necessarily the same as with respect to x. We can outfit equations (4.34) and (4.35) for the flux limiting equation by simply multiplying them by the grid spacing at the $i + 1/2^{th}$ cell wall, $\left(L^i + L^{i+1}\right)/2$. Equations (4.34) and (4.35) become

$$\Delta F^{i+1/2} = F^{i+1} - F^i \tag{4.36}$$

and

$$\Delta F^{i-1/2} = \frac{L^i + L^{i+1}}{L^{i-1} + L^i} F^i - F^{i-1}, \tag{4.37}$$

respectively. In turn, (4.31) becomes

$$F^{R,*}_{i+1/2} = F^R_{i+1/2} + \phi\left(\frac{L^i + L^{i+1}}{L^{i-1} + L^i}\frac{F^R_i - F^R_{i-1}}{2}, \frac{F^R_{i+1} - F^R_i}{2}\right), \tag{4.38}$$

where the F difference at the $i - 1/2^{th}$ cell wall is properly scaled to appropriately compare as a derivative with the difference at the $i + 1/2^{th}$cell wall. Similarly, equation (4.32) becomes

$$F^{L,*}_{i+1/2} = F^L_{i+1/2} + \phi\left(\frac{F^L_i - F^L_{i+1}}{2}, \frac{L^i + L^{i+1}}{L^{i+1} + L^{i+2}}\frac{F^L_{i+1} - F^L_{i+2}}{2}\right). \tag{4.39}$$

Note that for regular spacing ($L_{i-1} = L_i = L_{i+1} = L_{i+2}$), equation (4.38) and (4.39) reduces to equations (4.31) and (4.32), respectively.

4.4 Multi-dimensional second-order spatial accuracy

In the previous section we described how to achieve second-order spatial accuracy for one-dimensional flux equations. For three-dimensional space, we can apply one-dimensional techniques in what are called split or unsplit methods. Split methods integrate using fluxes in one dimension at a time sequentially, a method referred to as dimensional splitting. Details can be found in *Trac and Pen* (2002), *LeVeque* (1998), or *Strang* (1968) amongst several other publications. However, EMI does not integrate with one spatial dimension at a time; EMI integrates with all the spatial dimensions at once in unsplit fashion. For fluxes composed of curls, unsplit integration is essential for zero-divergent curls, which will be described in detail in Section 4.4.1.

4.4.1 Multi-dimensional zero-divergent curls

Both of Maxwell's equations (3.20) and (3.21) require the computation of a curl. As curls are analytically zero-divergent, we must ensure that they are also numerically zero-divergent. In a curvilinear coordinate system, $-\partial_t \mathbf{B}$ and $\nabla \cdot (\partial_t \mathbf{B})$ are given by

$$\begin{aligned} -\partial_t \mathbf{B} = \nabla \times \mathbf{E} = & \frac{\hat{\mathbf{x}}}{h_y h_z} \left\{ \partial_y \left(h_z E_z \right) - \partial_z \left(h_y E_y \right) \right\} \\ & + \frac{\hat{\mathbf{y}}}{h_x h_z} \left\{ \partial_z \left(h_x E_x \right) - \partial_x \left(h_z E_z \right) \right\} \\ & + \frac{\hat{\mathbf{z}}}{h_x h_y} \left\{ \partial_x \left(h_y E_y \right) - \partial_y \left(h_x E_x \right) \right\} \end{aligned} \tag{4.40}$$

and

$$\nabla \cdot (\partial_t \mathbf{B}) = \frac{\partial_x \left(h_y h_z \partial_t B_x \right) + \partial_y \left(h_x h_z \partial_t B_y \right) + \partial_z \left(h_x h_y \partial_t B_z \right)}{h_x h_y h_z}, \tag{4.41}$$

respectively. After computing the flux-limited discussed earlier, one may be tempted to compute the curl as

$$
\begin{aligned}
[-\partial_t \mathbf{B}]^{i,j,k} = & \frac{\hat{\mathbf{x}}}{[h_y h_z]^{i,j,k}} \left\{ \begin{array}{l} \dfrac{\left[h_z E_z^{*(y)}\right]^{i,j+1/2,k} - \left[h_z E_z^{*(y)}\right]^{i,j-1/2,k}}{2dy} \\ -\dfrac{\left[h_y E_y^{*(z)}\right]^{i,j,k+1/2} - \left[h_y E_y^{*(z)}\right]^{i,j,k-1/2}}{2dz} \end{array} \right\} \\
& + \frac{\hat{\mathbf{y}}}{[h_x h_z]^{i,j,k}} \left\{ \begin{array}{l} \dfrac{\left[h_x E_x^{*(z)}\right]^{i,j,k+1/2} - \left[h_x E_x^{*(z)}\right]^{i,j,k-1/2}}{2dz} \\ -\dfrac{\left[h_z E_z^{*(x)}\right]^{i+1/2,j,k} - \left[h_z E_z^{*(x)}\right]^{i-1/2,j,k}}{2dx} \end{array} \right\} \\
& + \frac{\hat{\mathbf{z}}}{[h_x h_y]^{i,j,k}} \left\{ \begin{array}{l} \dfrac{\left[h_y E_y^{*(x)}\right]^{i+1/2,j,k} - \left[h_y E_y^{*(x)}\right]^{i-1/2,j,k}}{2dx} \\ -\dfrac{\left[h_x E_x^{*(y)}\right]^{i,j+1/2,k} - \left[h_x E_x^{*(y)}\right]^{i,j-1/2,k}}{2dy} \end{array} \right\},
\end{aligned}
\tag{4.42}
$$

where superscripts $*(x)$, $*(y)$ and $*(z)$ denote flux limited electric fields (determined by 4.30) evaluated along the x, y, and z directions, respectively, and $[\,]^{i,j,k}$ indicates the value at the (i^{th}, j^{th}, k^{th}) cell in *x, y, z* coordinates. Note that for $[\,]^{i,j,k}$ whole numbers indicate the value at the center while 1/2's indicate the value at the cell wall. The divergence of equation (4.42) does not necessarily equal to zero, violating Gauss's law. The numerical problem lies in that each $\mathbf{E}^*$ component is flux-limited in two directions resulting in two versions of E_x^*, E_y^*, and E_z^*, each. Subsequently, equation (4.42) is a sum of incomplete curls of different versions of $\mathbf{E}^*$. Equation (4.42) cannot adequately compute a zero-divergent curl.

To numerically compute zero divergent curls we implement a flux-interpolated central-difference scheme as outlined by *Toth* (2000), but generalized for a three-dimensional curvilinear coordinate system. Let us define cell-centered fluxes as interpolations between the multiple versions of each $\mathbf{E}^*$

as

$$
\begin{aligned}
[\mathbf{E}^*]^{i,j,k} = &\frac{\hat{\mathbf{x}}}{4}\left\{\left[E_x^{*(y)}\right]^{i,j-1/2,k} + \left[E_x^{*(y)}\right]^{i,j+1/2,k} + \left[E_x^{*(z)}\right]^{i,j,k-1/2} + \left[E_x^{*(z)}\right]^{i,j,k+1/2}\right\} \\
&+ \frac{\hat{\mathbf{y}}}{4}\left\{\left[E_y^{*(x)}\right]^{i-1/2,j,k} + \left[E_y^{*(x)}\right]^{i+1/2,j,k} + \left[E_y^{*(z)}\right]^{i,j,k-1/2} + \left[E_y^{*(z)}\right]^{i,j,k+1/2}\right\} \\
&+ \frac{\hat{\mathbf{z}}}{4}\left\{\left[E_z^{*(x)}\right]^{i-1/2,j,k} + \left[E_z^{*(x)}\right]^{i+1/2,j,k} + \left[E_z^{*(y)}\right]^{i,j-1/2,k} + \left[E_z^{*(y)}\right]^{i,j+1/2,k}\right\}.
\end{aligned} \tag{4.43}
$$

With this cell-centered interpolated flux-limited $\mathbf{E}^*$, we can compute a zero-divergent curl as

$$
\begin{aligned}
[-\partial_t \mathbf{B}]^{i,j,k} = &\frac{\hat{\mathbf{x}}}{[h_y h_z]^{i,j,k}}\left\{\frac{[h_z E_z^*]^{i,j+1,k} - [h_z E_z^*]^{i,j-1,k}}{2dy} - \frac{\left[h_y E_y^*\right]^{i,j,k+1} - \left[h_y E_y^*\right]^{i,j,k-1}}{2dz}\right\} \\
&+ \frac{\hat{\mathbf{y}}}{[h_x h_z]^{i,j,k}}\left\{\frac{[h_x E_x^*]^{i,j,k+1} - [h_x E_x^*]^{i,j,k-1}}{2dz} - \frac{[h_z E_z^*]^{i+1,j,k} - [h_z E_z^*]^{i-1,j,k}}{2dx}\right\} \\
&+ \frac{\hat{\mathbf{z}}}{[h_x h_y]^{i,j,k}}\left\{\frac{\left[h_y E_y^*\right]^{i+1,j,k} - \left[h_y E_y^*\right]^{i-1,j,k}}{2dx} - \frac{[h_x E_x^*]^{i,j+1,k} - [h_x E_x^*]^{i,j-1,k}}{2dy}\right\}.
\end{aligned} \tag{4.44}
$$

We can show that this curl is in fact zero-divergent. Using the same central-differencing as in equation (4.44), the divergence of the curl is

$$
\begin{aligned}
\nabla \cdot [-\partial_t \mathbf{B}]^{i,j,k} = &\frac{[h_y h_z\,(-\partial_t B_x)]^{i+1,j,k} - [h_y h_z\,(-\partial_t B_x)]^{i-1,j,k}}{2dx \cdot [h_x h_y h_z]^{i,j,k}} \\
&+ \frac{[h_x h_z\,(-\partial_t B_y)]^{i,j+1,k} - [h_x h_z\,(-\partial_t B_y)]^{i,j-1,k}}{2dy \cdot [h_x h_y h_z]^{i,j,k}} \\
&+ \frac{[h_x h_y\,(-\partial_t B_z)]^{i,j,k+1} - [h_x h_y\,(-\partial_t B_z)]^{i,j,k-1}}{2dz \cdot [h_x h_y h_z]^{i,j,k}}.
\end{aligned} \tag{4.45}
$$

Substituting equation (4.44) into (4.45) yields

$$\begin{aligned}
\nabla \cdot [-\partial_t \mathbf{B}]^{i,j,k} = & \frac{\left\{ \begin{array}{l} \frac{[h_z E_z^*]^{i+1,j+1,k} - [h_z E_z^*]^{i+1,j-1,k}}{2dy} - \frac{\left[h_y E_y^*\right]^{i+1,j,k+1} - \left[h_y E_y^*\right]^{i+1,j,k-1}}{2dz} \\ -\frac{[h_z E_z^*]^{i-1,j+1,k} - [h_z E_z^*]^{i-1,j-1,k}}{2dy} + \frac{\left[h_y E_y^*\right]^{i-1,j,k+1} - \left[h_y E_y^*\right]^{i-1,j,k-1}}{2dz} \end{array} \right\}}{2dx \cdot [h_x h_y h_z]^{i,j,k}} \\
& + \frac{\left\{ \begin{array}{l} \frac{[h_x E_x^*]^{i,j+1,k+1} - [h_x E_x^*]^{i,j+1,k-1}}{2dz} - \frac{[h_z E_z^*]^{i+1,j+1,k} - [h_z E_z^*]^{i-1,j+1,k}}{2dx} \\ -\frac{[h_x E_x^*]^{i,j-1,k+1} - [h_x E_x^*]^{i,j-1,k-1}}{2dz} + \frac{[h_z E_z^*]^{i+1,j-1,k} - [h_z E_z^*]^{i-1,j-1,k}}{2dx} \end{array} \right\}}{2dy \cdot [h_x h_y h_z]^{i,j,k}} \\
& + \frac{\left\{ \begin{array}{l} \frac{\left[h_y E_y^*\right]^{i+1,j,k+1} - \left[h_y E_y^*\right]^{i-1,j,k+1}}{2dx} - \frac{[h_x E_x^*]^{i,j+1,k+1} - [h_x E_x^*]^{i,j-1,k+1}}{2dy} \\ -\frac{\left[h_y E_y^*\right]^{i+1,j,k-1} - \left[h_y E_y^*\right]^{i-1,j,k-1}}{2dx} + \frac{[h_x E_x^*]^{i,j+1,k-1} - [h_x E_x^*]^{i,j-1,k-1}}{2dy} \end{array} \right\}}{2dz \cdot [h_x h_y h_z]^{i,j,k}} \\
& = 0,
\end{aligned} \tag{4.46}$$

showing that the numerical curl (4.44) is zero-divergent (at least to the accuracy of computational round-off errors). The curl of $\mathbf{B}$ used in Maxwell-Ampere's law is computed the same way for zero-divergence.

4.4.2 Multi-dimensional method for the continuity equation

The method for zero-divergent curls does not apply to the continuity equation (3.22). However, the flux term for the unsplit method for the continuity equation is more simply expressed as

$$\begin{aligned}
[\nabla \cdot (n_i \mathbf{v}_i)]^{i,j,k} = & \frac{\left[h_y h_z \left(n_i v_{ix}\right)^{*(x)}\right]^{i+1/2,j,k} - \left[h_y h_z \left(n_i v_{ix}\right)^{*(x)}\right]^{i-1/2,j,k}}{dx \left[h_x h_y h_z\right]^{i,j,k}} \\
& \frac{\left[h_x h_z \left(n_i v_{iy}\right)^{*(y)}\right]^{i,j+1/2,k} - \left[h_x h_z \left(n_i v_{iy}\right)^{*(y)}\right]^{i,j-1/2,k}}{dy \left[h_x h_y h_z\right]^{i,j,k}}, \\
& \frac{\left[h_x h_y \left(n_i v_{iz}\right)^{*(z)}\right]^{i,j,k+1/2} - \left[h_x h_y \left(n_i v_{iz}\right)^{*(z)}\right]^{i,j,k-1/2}}{dx \left[h_x h_y h_z\right]^{i,j,k}}
\end{aligned} \tag{4.47}$$

where superscripts $*(x)$, $*(y)$ and $*(z)$ denote flux limited fluxes (determined by equation 4.30) evaluated along the x, y, and z directions, respectively, and $[\,]^{i,j,k}$ indicates the value at the (i^{th}, j^{th}, k^{th}) cell in x, y, z coordinates.

4.5 Applying ion inertia to Maxwell-Ampere's law

Let us examine the equations we integrate,

$$\partial_t \mathbf{B} = -\nabla \times \mathbf{E} \tag{4.48}$$

$$\begin{aligned}\partial_t \mathbf{E} =& \frac{c^2 V_a^2}{c^2 + V_a^2} \left[\nabla \times \mathbf{B} - \mu_0 \mathbf{J}'\right]_\perp \\ &+ c^2 \left[\nabla \times \mathbf{B} - \mu_0 \mathbf{J}'\right]_\parallel\end{aligned} \tag{4.49}$$

$$\partial_t n_i = -\nabla \cdot (n_i \mathbf{v}_i)\,. \tag{4.50}$$

Equation (4.48) and (4.50) are already in flux form. However, equation (4.49) is not; the leading $c^2 V_a^2 / \left(c^2 + V_a^2\right)$ factor is not necessarily constant. This is rectified by flux limiting the Maxwell-Ampere's law without ion inertia,

$$\partial_t \mathbf{E} = c^2 \left[\nabla \times \mathbf{B} - \mu_0 \mathbf{J}'\right], \tag{4.51}$$

which is in flux form. Following the flux limiting of equation (4.51), ion inertia is applied by scaling the perpendicular components by $V_a^2 / \left(c^2 + V_a^2\right)$, which fully models the Alfvénic Maxwell-Ampere's law (4.49).

4.6 First-order time integration

Recall EMI's differential model equations (3.20) through (3.22) rewritten for convenience:

$$\partial_t \mathbf{B} = -\nabla \times \mathbf{E} \tag{4.52}$$

$$\begin{aligned}\partial_t \mathbf{E} = {} & \frac{c^2 V_a^2}{c^2 + V_a^2} \left[\nabla \times \mathbf{B} - \mu_0 \mathbf{J}'\right]_\perp \\ & + c^2 \left[\nabla \times \mathbf{B} - \mu_0 \mathbf{J}'\right]_\parallel \end{aligned} \tag{4.53}$$

$$\partial_t n_i = -\nabla \cdot (n_i \mathbf{v}_i), \tag{4.54}$$

where $\mathbf{J}'$ is

$$\begin{aligned}\mathbf{J}' = {} & e n_e \tilde{\mathbf{A}}_i \left(\frac{e\mathbf{E}}{M} + \mathbf{g} - \frac{\nabla p_i}{n_i M} + \nu_{ie}\mathbf{v}_e + \nu_{in}\mathbf{v}_n - \overline{\mathbf{v}}_i \cdot \nabla \overline{\mathbf{v}}_{i\perp} \right) \\ & - e n_e \tilde{\mathbf{A}}_e \left(-\frac{e\mathbf{E}}{m} + \mathbf{g} - \frac{\nabla p_e}{n_e m} + \nu_{ei}\mathbf{v}_i + \nu_{en}\mathbf{v}_n \right). \end{aligned} \tag{4.55}$$

EMI integrates Maxwell-Faraday's law, the Alfvénic Maxwell-Ampere's law, and the continuity equation through time. In other words, EMI integrates a $(7 \times n_x \times n_y \times n_z)$-dimensional vector where there are 7 state variables ($\mathbf{B}$, $\mathbf{E}$, n_i) for each grid point on a n_x by n_y by n_z grid. The differential equation we integrate takes the form of

$$\partial_t \mathbf{U} = D(\mathbf{U}), \tag{4.56}$$

where $D(\mathbf{U})$ is the differential equation of $\mathbf{U}$ as a function of $\mathbf{U}$ defined by equations (4.52), (4.53), and (4.54). In this section we will discuss the first-order Euler method and Backward-Euler methods for time integration that will later be used to implement a second-order time integration scheme.

4.6.1 First-order explicit time integration: Euler method

One of the simplest ways to integrate partial differential equations is by the Euler method (*Press et al.*, 2007), a popular way to explicitly integrate differential equations. The term "explicitly" refers to how the method can determine the next iteration of $\mathbf{U}$ (which we will refer to as $\mathbf{U}^{n+1}$) explicitly from the current iteration (which we refer to as $\mathbf{U}^n$). The Euler method models $\partial_t \mathbf{U} = D(\mathbf{U})$ as

$$\frac{\mathbf{U}^{n+1} - \mathbf{U}^n}{h} = D(\mathbf{U}^n), \tag{4.57}$$

where h is the time step we wish integrate. Solving for next iteration of $\mathbf{U}$ is formulated as

$$\mathbf{U}^{n+1} = \mathbf{U}^n + h \cdot D(\mathbf{U}^n). \tag{4.58}$$

This method is simple and is sufficient for non-stiff integration. However, it is only linearly accurate and it assumes that the $D(\mathbf{U})$ is constant throughout the whole h step interval ($\partial_t D(\mathbf{U}) = 0$). For stiff differential equations, $D(\mathbf{U}^n)$ can be wildly inappropriate for integrating unless h is really small. Keep in mind that smaller h steps requires more iterations than large h steps and may be implausible to numerically compute.

In many cases, the Euler method can also be unstable (*Press et al.*, 2007). The instability of the Euler method can be illustrated with a simple one-dimensional toy example differential equation

$$\partial_t U = -\gamma U, \tag{4.59}$$

which is the classic equation for exponential decay for $\gamma > 0$. The analytical integration should be exactly

$$U^{n+1} = U^n e^{-\gamma h} \tag{4.60}$$

Taking $h \to \infty$ should yield $U^{n+1} = 0$. However, integrating this equation with the Euler method,

$$U^{n+1} = U^n - h \cdot \gamma U^n, \tag{4.61}$$

and taking $h \to \infty$ yields $\left|U^{n+1}\right| = \infty$. Secondly, the magnitude of the ratio between consecutive U iterations,

$$\left|\frac{U^{n+1}}{U^n}\right| = \left|1 - h \cdot \gamma\right|, \tag{4.62}$$

is greater than unity for $h \cdot \gamma > 2$, indicating a growing U after each iteration, where U should decay to zero. Both (4.61) and (4.62) illustrate the Euler method can wildly overshoot integrals for large h. In order for the method to work, one needs to use very small h.

4.6.2 First-order implicit time integration: Backward-Euler method

A more stable method of integration is the Back-Euler method, which is an implicit method. The explicit Euler method explicitly defined its differential equations by $\mathbf{U}^n$. Implicit methods attempt to define the differential equation by $\mathbf{U}^{n+1}$. The backward-Euler method models $\partial_t \mathbf{U} = D\left(\mathbf{U}\right)$ as

$$\frac{\mathbf{U}^{n+1} - \mathbf{U}^n}{h} = D\left(\mathbf{U}^{n+1}\right). \tag{4.63}$$

Solving for next iteration of $\mathbf{U}$ requires algebra unique to the set of equations you want to integrate, but is often more stable than the Euler method.

The stability of the backward-Euler method can be demonstrated with the same one-dimensional toy example (4.59). Using the backward-Euler method (4.63) with (4.59) and solving for $\mathbf{U}^{n+1}$ yields the numerical integration,

$$U^{n+1} = \frac{U^n}{1 + h \cdot \gamma}. \tag{4.64}$$

Taking $h \to \infty$ yields $U^{n+1} = 0$, which is the proper asymptotic limit. Secondly, for any h the ratio

between the magnitudes of consecutive U iterations,

$$\frac{\left|U^{n+1}\right|}{|U^n|} = \frac{1}{1+h\cdot\gamma}, \tag{4.65}$$

is unconditionally less than unity, indicating a decaying U after each iteration, where U should, in fact, decay. Both (4.64) and (4.65) illustrate that the backward-Euler method is stable and relaxes to the asymptotic of the real solution, for any h. However, keep in mind that this method is still only first-order accurate. Also, in many cases, it is not possible to solve the whole set of differential equations completely implicitly; there may be no way to solve equation (4.63) for $\mathbf{U}^{n+1}$. EMI cannot completely integrate its differential equations (4.52), (4.53), and (4.54) implicitly with the backward-Euler method. EMI instead utilizes the backward-Euler method where it can, and utilizes the Euler method when the backward-Euler is not possible.

4.6.3 EMI's first-order semi-implicit time-integration

For stability reasons, we would prefer to implicitly integrate all of $\mathbf{U}$. In fact for Maxwell-Ampere's law, implicit integration is necessary. Implicit time integration allows EMI to integrate over shorter time scale oscillations associated with the electron plasma frequency and the electron gyrofrequency, that we do not wish to resolve. However, it is algebraically impossible to solve equation (4.63) for all of $\mathbf{U}^{n+1}$ with EMI's formulas (4.52) to (4.54). Hence, EMI's integration scheme is composed of implicit integration where possible, and explicit integration elsewhere. In other words, EMI's integration takes the form,

$$\frac{\mathbf{U}^{n+1}-\mathbf{U}^n}{h} = D_e\left(\mathbf{U}\right) + D_i\left(\mathbf{U}\right), \tag{4.66}$$

where $D_e(\mathbf{U})$ refers to the differential equations to be integrated explicitly and $D_i(\mathbf{U})$ refers to the differential equations to be integrated implicitly. To be more specific, let us represent $\mathbf{U}$ as

$$\mathbf{U} = \begin{bmatrix} \mathbf{B} \\ \mathbf{E} \\ n_i \end{bmatrix}. \tag{4.67}$$

Then $D_e(\mathbf{U})$ can be given by

$$D_e(\mathbf{U}) = \begin{bmatrix} -\nabla \times \mathbf{E}^n \\ \frac{c^2 V_a^2}{c^2 + V_a^2} \left[\nabla \times \mathbf{B}^n - \mu_0 \mathbf{J}'^n|_{\mathbf{E}_1=0}\right]_\perp + c^2 \left[\nabla \times \mathbf{B}^n - \mu_0 \mathbf{J}'^n|_{\mathbf{E}_1=0}\right]_\parallel \\ -\nabla \cdot (n_i^n \mathbf{v}_i^n) \end{bmatrix}, \tag{4.68}$$

where $\mathbf{J}'^n|_{\mathbf{E}_1=0}$ is $\mathbf{J}'^n$ without $\mathbf{E}_1$ contributions. The $\mathbf{E}_1$ contributions to $\mathbf{J}'$ are found in $D_i(\mathbf{U})$, which is given by

$$D_i(\mathbf{U}) = \begin{bmatrix} 0 \\ \frac{c^2 V_a^2}{c^2 + V_a^2} \left[-\mu_0 \tilde{\boldsymbol{\sigma}} \cdot \mathbf{E}_1^{n+1}\right]_\perp + c^2 \left[-\mu_0 \tilde{\boldsymbol{\sigma}} \cdot \mathbf{E}_1^{n+1}\right]_\parallel \\ 0 \end{bmatrix}, \tag{4.69}$$

where $\tilde{\boldsymbol{\sigma}}$ is the conductivity tensor (2.15). Using equations (4.125) and (4.69), equation (4.66) can be written out as

$$\begin{aligned}
\frac{\mathbf{B}_1^{n+1}-\mathbf{B}_1^n}{h} &= -\nabla\times\mathbf{E}^n && (4.70)\\
\frac{\mathbf{E}_1^{n+1}-\mathbf{E}_1^n}{h} &= \frac{c^2V_a^2}{c^2+V_a^2}\left[\nabla\times\mathbf{B}^n-\mu_0\mathbf{J}'^n\big|_{\mathbf{E}_1=0}-\mu_0\tilde{\boldsymbol{\sigma}}\cdot\mathbf{E}_1^{n+1}\right]_\perp \\
&+ c^2\left[\nabla\times\mathbf{B}^n-\mu_0\mathbf{J}'^n\big|_{\mathbf{E}_1=0}-\mu_0\tilde{\boldsymbol{\sigma}}\cdot\mathbf{E}_1^{n+1}\right]_\parallel && (4.71)\\
\frac{n_i^{n+1}-n_i^n}{h} &= -\nabla\cdot(n_i^n\mathbf{v}_i^n)\,. && (4.72)
\end{aligned}$$

Solving for $\mathbf{U}^{n+1}$ yields the following equations

$$\begin{aligned}
\mathbf{B}_1^{n+1} &= \mathbf{B}_1^n - h\cdot\nabla\times\mathbf{E}_\perp^n && (4.73)\\
\mathbf{E}_{1\perp}^{n+1} &= \left\{\left[1+h\cdot\frac{c^2V_a^2}{c^2+V_a^2}\mu_0\tilde{\boldsymbol{\sigma}}\right]^{-1}\cdot\left(\mathbf{E}_1^n+h\cdot\frac{c^2V_a^2}{c^2+V_a^2}\left[\nabla\times\mathbf{B}^n-\mu_0\mathbf{J}'^n\big|_{\mathbf{E}_1=0}\right]\right)\right\}_\perp && (4.74)\\
\mathbf{E}_{1\parallel}^{n+1} &= \frac{\mathbf{E}_{1\parallel}^n+h\cdot c^2\left[\nabla\times\mathbf{B}^n-\mu_0\mathbf{J}'^n|_{\mathbf{E}_1=0}\right]_\parallel}{1+h\cdot c^2\mu_0\sigma_0} && (4.75)\\
n_i^{n+1} &= n_i^n - h\cdot\nabla\cdot(n_i^n\mathbf{v}_i^n)\,, && (4.76)
\end{aligned}$$

The benefits of the implicit integration in (4.74) and (4.75) is found by taking $h\to\infty$,

$$\begin{aligned}
\mathbf{E}_{1\perp}^{n+1} &= \left\{[\mu_0\tilde{\boldsymbol{\sigma}}]^{-1}\cdot\left(\left[\nabla\times\mathbf{B}^n-\mu_0\mathbf{J}'^n\big|_{\mathbf{E}_1=0}\right]\right)\right\}_\perp \\
\mathbf{E}_{1\parallel}^{n+1} &= \frac{\left[\nabla\times\mathbf{B}^n-\mu_0\mathbf{J}'^n|_{\mathbf{E}_1=0}\right]_\parallel}{\mu_0\sigma_0},
\end{aligned}$$

which can be rearranged and combined as

$$\nabla\times\mathbf{B}^n=\mu_0\left(\mathbf{J}'^n\big|_{\mathbf{E}_1=0}+\tilde{\boldsymbol{\sigma}}\mathbf{E}_1\right), \qquad (4.77)$$

where it is apparent that $\mathbf{E}$ is relaxed to an asymptotic limit that satisfies $\nabla \times \mathbf{B} = \mu_0 \mathbf{J}'$, a feature that the Euler method cannot achieve without an extremely small h. The implicit integration effectively integrates over shorter time scale oscillations associated with the electron plasma frequency and gyrofrequency. For convenience of the reader, equation (4.74) and (4.75) with the conductivity tensor (2.15) can also be written out as

$$\begin{aligned}
\mathbf{E}_1^{n+1} = & \frac{P}{P^2+H^2} \cdot \left(\mathbf{E}_{1\perp}^n + h \cdot \frac{c^2 V_a^2}{c^2+V_a^2} \left[\nabla \times \mathbf{B}^n - \mu_0 \mathbf{J}'^n \big|_{\mathbf{E}_1=0} \right]_\perp \right) \\
& + \frac{H}{P^2+H^2} \cdot \left(\mathbf{E}_{1\perp}^n + h \cdot \frac{c^2 V_a^2}{c^2+V_a^2} \left[\nabla \times \mathbf{B}^n - \mu_0 \mathbf{J}'^n \big|_{\mathbf{E}_1=0} \right]_\perp \right) \times \frac{\mathbf{B}}{|\mathbf{B}|} \\
& + \frac{1}{1+h \cdot c^2 \mu_0 \sigma_0} \cdot \left(\mathbf{E}_{1\parallel}^n + h \cdot c^2 \left[\nabla \times \mathbf{B}^n - \mu_0 \mathbf{J}'^n \big|_{\mathbf{E}_1=0} \right]_\parallel \right),
\end{aligned} \tag{4.78}$$

where

$$P = 1 + h \cdot \frac{c^2 V_a^2}{c^2+V_a^2} \mu_0 \sigma_p \tag{4.79}$$

$$H = h \cdot \frac{c^2 V_a^2}{c^2+V_a^2} \mu_0 \sigma_h. \tag{4.80}$$

Alternatively, if using the Cowling conductivity tensor (3.87), equation (4.74) and (4.75) is written out as

$$\begin{aligned}
\mathbf{E}_1^{n+1} = & \frac{1}{C} \cdot \left(\mathbf{E}_{1x}^n + h \cdot \frac{c^2 V_a^2}{c^2+V_a^2} \left[\nabla \times \mathbf{B}^n - \mu_0 \mathbf{J}'^n \big|_{\mathbf{E}_1=0} \right]_{zonal} \right) \\
& + \frac{1}{P} \cdot \left(\mathbf{E}_{1z}^n + h \cdot \frac{c^2 V_a^2}{c^2+V_a^2} \left[\nabla \times \mathbf{B}^n - \mu_0 \mathbf{J}'^n \big|_{\mathbf{E}_1=0} \right]_{meridional} \right) \\
& + \frac{H}{CP} \cdot \left(\mathbf{E}_{1x}^n + h \cdot \frac{c^2 V_a^2}{c^2+V_a^2} \left[\nabla \times \mathbf{B}^n - \mu_0 \mathbf{J}'^n \big|_{\mathbf{E}_1=0} \right]_{zonal} \right) \times \frac{\mathbf{B}}{|\mathbf{B}|} \\
& + \frac{1}{1+h \cdot c^2 \mu_0 \sigma_0} \cdot \left(\mathbf{E}_{1\parallel}^n + h \cdot c^2 \left[\nabla \times \mathbf{B}^n - \mu_0 \mathbf{J}'^n \big|_{\mathbf{E}_1=0} \right]_\parallel \right),
\end{aligned} \tag{4.81}$$

where the subscripts *zonal* and *meridional* refer strictly to zonal and meridional components, respectively, and where

$$C = 1 + h \cdot \frac{c^2 V_a^2}{c^2 + V_a^2} \mu_0 \sigma_c. \tag{4.82}$$

4.7 Second-order time integration

In the previous section, we discussed first-order methods to integrate EMI's equations. While stable, we wish to improve temporal accuracy to the second-order. Fortunately, we can use the first-order methods discussed earlier using Runge-Kutta methods in order to achieve second-order accuracy, which will be discussed in this section.

4.7.1 Exact Taylor series of time integration

Before we discuss how EMI achieves second-order temporal accuracy, let us first derive the Taylor series of time integrating $\mathbf{U}$ from the nth to the $n+1$th iteration given its derivative function, $D(\mathbf{U})$. As a Taylor series, the $n+1$th iteration of $\mathbf{U}$ takes the form of

$$\mathbf{U}^{n+1} = C_0 + C_1 h + C_2 h^2 + C_3 h^3 + ... \tag{4.83}$$

where C_i is the i'th Taylor coefficient and h is the time step we wish to integrate from the nth to the $n+1$th iteration. C_0 is simply solved for by setting $h = 0$ which implies no change in $\mathbf{U}^{n+1}$ or in other words, $\mathbf{U}^{n+1} = \mathbf{U}^n$. Thus,

$$C_0 = \mathbf{U}^n, \tag{4.84}$$

the initial value. Taking the derivative of equation (4.83) yields

$$d_h \mathbf{U}^{n+1} = C_1 + 2C_2 h + 3C_3 h^2 + ... = D(\mathbf{U}), \tag{4.85}$$

recalling that $D(\mathbf{U})$ is the derivative function of $\mathbf{U}$. We solve for C_1 by setting $h = 0$. Thus,

$$C_1 = D(\mathbf{U}). \tag{4.86}$$

Taking the derivative of equation (4.85) yields

$$d_h^2 \mathbf{U}^{n+1} = 2C_2 + 6C_3 h + ... = \partial_{\mathbf{U}} D(\mathbf{U}) \cdot D(\mathbf{U}), \tag{4.87}$$

where we applied the chain rule to the furthest right hand side and $\partial_{\mathbf{U}}$ is the partial derivative with respect to $\mathbf{U}$. C_2 is solved by setting $h = 0$. Thus,

$$C_2 = \frac{1}{2} \partial_{\mathbf{U}} D(\mathbf{U}) \cdot D(\mathbf{U}). \tag{4.88}$$

Having solved for C_0, C_1, and C_2, the exact Taylor series for time integration is

$$\mathbf{U}^{n+1} = \mathbf{U}^n + D(\mathbf{U}) h + \partial_{\mathbf{U}} D(\mathbf{U}) \cdot D(\mathbf{U}) \frac{h^2}{2} + O\left(h^3\right), \tag{4.89}$$

where we use big-O notation to represent terms of order i or greater with $O\left(h^i\right)$. For a vector $\mathbf{F} = O\left(h^i\right)$ means that $|\mathbf{F}| < \mathbf{A} h^i$ for some constant vector, $\mathbf{A}$. We already formulated $D(\mathbf{U})$ as a with equations (3.20) to (3.22). However, the question remains: how do we implement second-order temporal accuracy and obtain $\partial_{\mathbf{U}} D(\mathbf{U})$ from a set of equations that only includes first derivatives? An exact analytical formula for $\partial_{\mathbf{U}} D(\mathbf{U})$ would be complex to implement. It would also double the set of derivative equations. Instead, we can simply use the first-order time integration scheme discussed in Section 4.6 to achieve second-order accuracy using second-order schemes described in the following subsections.

4.7.2 Explicit second-order time integration: Explicit Runge-Kutta method

Consider the commonly used explicit second-order Runge-Kutta scheme that can be found in *Press et al.* (2007) or *Trac and Pen* (2002), which can be expressed as

$$\mathbf{U}^{n+1} = \mathbf{U}^n + D_e\left(\mathbf{U}^n + D_e\left(\mathbf{U}^n\right)\frac{h}{2}\right)\cdot h, \tag{4.90}$$

where $D_e\left(\mathbf{U}\right)$ is the differential function that we wish to integrate explicitly (as opposed to differential functions which we will want to integrate implicitly). The first and second derivatives of $\mathbf{U}^{n+1}$ are

$$d_h\mathbf{U}^{n+1} = D_e\left(\mathbf{U}^n + D_e\left(\mathbf{U}^n\right)\frac{h}{2}\right) + \partial_{\mathbf{U}}D_e\left(\mathbf{U}^n + D_e\left(\mathbf{U}^n\right)\frac{h}{2}\right)\cdot\frac{D_e\left(\mathbf{U}^n\right)}{2}h \tag{4.91}$$

$$d_h^2\mathbf{U}^{n+1} = \partial_{\mathbf{U}}D_e\left(\mathbf{U}^n + D_e\left(\mathbf{U}^n\right)\frac{h}{2}\right)\cdot D_e\left(\mathbf{U}^n\right) + \partial_{\mathbf{U}}^2D_e\left(\mathbf{U}^n + D_e\left(\mathbf{U}^n\right)\frac{h}{2}\right)\cdot\left(\frac{D_e\left(\mathbf{U}^n\right)}{2}\right)^2 h \quad , \tag{4.92}$$

respectively. The zeroth to second derivative of $\mathbf{U}^{n+1}$ at $h = 0$ are

$$\begin{aligned}
\mathbf{U}^{n+1}\big|_{h=0} &= \mathbf{U}^n \\
\partial_h\mathbf{U}^{n+1}\big|_{h=0} &= D_e\left(\mathbf{U}^n\right) \\
\partial_h^2\mathbf{U}^{n+1}\big|_{h=0} &= \partial_{\mathbf{U}}D_e\left(\mathbf{U}^n\right)\cdot D_e\left(\mathbf{U}^n\right),
\end{aligned} \tag{4.93}$$

respectively. Thus the Taylor expansion of $\mathbf{U}^{n+1}$ at $h = 0$ is

$$\mathbf{U}^{n+1} = \mathbf{U}^n + D_e\left(\mathbf{U}^n\right)h + \partial_{\mathbf{U}}D_e\left(\mathbf{U}^n\right)\cdot D_e\left(\mathbf{U}^n\right)\frac{h^2}{2} + O\left(h^3\right). \tag{4.94}$$

Note that the similarities to the exact Taylor series (4.89) up to the second-order. For this explicit method, the first derivative is given by $D_e\left(\mathbf{U}^n\right)$. The second derivative, $\partial_{\mathbf{U}}D\left(\mathbf{U}\right)\cdot D\left(\mathbf{U}\right)$, is given by $\partial_{\mathbf{U}}D_e\left(\mathbf{U}^n\right)\cdot D_e\left(\mathbf{U}^n\right)$. Hence, the explicit Runge-Kutta scheme is considered second-order accurate in the temporal sense. We use this explicit Runge-Kutta scheme to integrate EMI's non-stiff differential

equations and equations than cannot be formulated implicitly.

4.7.3 Implicit second-order time integration: Implicit Runge-Kutta method

For differential equations we wish to integrate implicitly, we could utilize a diagonal implicit Runge-Kutta scheme (*Norsett*, 1974; *Crouzeix*, 1976; *Alexander*, 1977; *Butcher*, 1987; *Ascher et al.*, 1997). The implicit Runge-Kutta scheme EMI uses can be described as

$$\mathbf{U}^{n+1} = \mathbf{U}^n + (1-\alpha)\,\mathbf{K}_1 + \alpha\mathbf{K}_2, \tag{4.95}$$

where

$$\mathbf{K}_1 = D_i\left(\mathbf{U}^n + \alpha\mathbf{K}_1\right)h$$

after which we use to determine

$$\mathbf{K}_2 = D_i\left(\mathbf{U}^n + (1-\alpha)\,\mathbf{K}_1 + \alpha\mathbf{K}_2\right)h.$$

The steps to implement the scheme is as follows:

1. Implicitly integrate by an αh step where you subsequently determine $\mathbf{K}_1$.
2. From the αh point, extrapolate to the $(1-\alpha)\,h$ point using $D_i\left(\mathbf{U}^n + \alpha\mathbf{K}_1\right)$. Or equivalently, $\mathbf{U}^{n+(1-\alpha)} = \mathbf{U}^n + (1-\alpha)\,\mathbf{K}_1$.
3. From the $(1-\alpha)\,h$ point, implicitly integrate an additional αh to complete the full h step, which results in equation (4.95).

The scheme maintains the stable properties of implicit integration (*Alexander*, 1977; *Ascher et al.*, 1997). In intuitive terms, the stability comes from the fact that the last step is an implicit integration. Not only is the scheme stable, but it will be shown that the scheme is second-order accurate

for specific α. The first derivative of $\mathbf{K}_1$ is derived as

$$d_h\mathbf{K}_1 = D_i\left(\mathbf{U}^n + \alpha\mathbf{K}_1\right) + \alpha\partial_{\mathbf{U}}D_i\left(\mathbf{U}^n + \alpha\mathbf{K}_1\right)d_h\mathbf{K}_1 h$$

$$d_h\mathbf{K}_1 = \frac{D_i\left(\mathbf{U}^n + \alpha\mathbf{K}_1\right)}{1 - \alpha\partial_{\mathbf{U}}D_i\left(\mathbf{U}^n + \alpha\mathbf{K}_1\right)h}. \tag{4.96}$$

The second derivative is

$$\begin{aligned} d_h^2\mathbf{K}_1 = &\frac{\alpha\partial_{\mathbf{U}}D_i\left(\mathbf{U}^n + \alpha\mathbf{K}_1\right)d_h\mathbf{K}_1 \cdot \left[1 - \alpha\partial_{\mathbf{U}}D_i\left(\mathbf{U}^n + \alpha\mathbf{K}_1\right)h\right]}{\left[1 - \alpha\partial_{\mathbf{U}}D_i\left(\mathbf{U}^n + \alpha\mathbf{K}_1\right)h\right]^2} \\ &- \frac{D_i\left(\mathbf{U}^n + \alpha\mathbf{K}_1\right)\left[-\alpha\partial_{\mathbf{U}}D_i\left(\mathbf{U}^n + \alpha\mathbf{K}_1\right) - \alpha\partial_{\mathbf{U}}^2D_i\left(\mathbf{U}^n + \alpha\mathbf{K}_1\right)d_h\mathbf{K}_1 h\right]}{\left[1 - \alpha\partial_{\mathbf{U}}D_i\left(\mathbf{U}^n + \alpha\mathbf{K}_1\right)h\right]^2} \end{aligned} \tag{4.97}$$

The first derivative of $\mathbf{K}_2$ is a little more complicated, because $\mathbf{K}_2$ is coupled with $\mathbf{K}_1$ by definition. Nonetheless, the first derivative is derived as

$$\mathbf{K}_2 = D_i\left(\mathbf{U}^n + (1-\alpha)\mathbf{K}_1 + \alpha\mathbf{K}_2\right)h$$

$$d_h\mathbf{K}_2 = D_i\left(\mathbf{U}^n + (1-\alpha)\mathbf{K}_1 + \alpha\mathbf{K}_2\right) + \partial_{\mathbf{U}}D_i\left(\mathbf{U}^n + (1-\alpha)\mathbf{K}_1 + \alpha\mathbf{K}_2\right)d_h\left((1-\alpha)\mathbf{K}_1 + \alpha\mathbf{K}_2\right)h$$

$$d_h\mathbf{K}_2 = \frac{D_i\left(\mathbf{U}^n + (1-\alpha)\mathbf{K}_1 + \alpha\mathbf{K}_2\right) + (1-\alpha)\partial_{\mathbf{U}}D_i\left(\mathbf{U}^n + (1-\alpha)\mathbf{K}_1 + \alpha\mathbf{K}_2\right)d_h\mathbf{K}_1 \cdot h}{1 - \alpha\partial_{\mathbf{U}}D_i\left(\mathbf{U}^n + (1-\alpha)\mathbf{K}_1 + \alpha\mathbf{K}_2\right)h}. \tag{4.98}$$

The second derivative is

$$\begin{aligned} d_h^2\mathbf{K}_2 = &\frac{\left[\partial_{\mathbf{U}}D_i\left(\mathbf{U}^n + (1-\alpha)\mathbf{K}_1 + \alpha\mathbf{K}_2\right)d_h\left(2(1-\alpha)\mathbf{K}_1 + \alpha\mathbf{K}_2\right) + O(h)\right]\left[1 - O(h)\right]}{\left[1 - \alpha\partial_{\mathbf{U}}D_i\left(\mathbf{U}^n + (1-\alpha)\mathbf{K}_1 + \alpha\mathbf{K}_2\right)h\right]^2} \\ &- \frac{\left[D_i\left(\mathbf{U}^n + (1-\alpha)\mathbf{K}_1 + \alpha\mathbf{K}_2\right) + O(h)\right]\left[-\alpha\partial_{\mathbf{U}}D_i\left(\mathbf{U}^n + (1-\alpha)\mathbf{K}_1 + \alpha\mathbf{K}_2\right) - O(h)\right]}{\left[1 - \alpha\partial_{\mathbf{U}}D_i\left(\mathbf{U}^n + (1-\alpha)\mathbf{K}_1 + \alpha\mathbf{K}_2\right)h\right]^2}. \end{aligned} \tag{4.99}$$

The derivatives of $\mathbf{K}_1$ and $\mathbf{K}_2$ at $h = 0$ are

$$\begin{aligned}
d_h\mathbf{K}_1\left(h=0\right) &= D_i\left(\mathbf{U}^n + \alpha\mathbf{K}_1\right) \\
d_h\mathbf{K}_2\left(h=0\right) &= D_i\left(\mathbf{U}^n + \left(1-\alpha\right)\mathbf{K}_1 + \alpha\mathbf{K}_2\right) \\
d_h^2\mathbf{K}_1\left(h=0\right) &= 2\alpha\partial_{\mathbf{U}} D_i\left(\mathbf{U}^n + \alpha\mathbf{K}_1\right) D_i\left(\mathbf{U}^n + \alpha\mathbf{K}_1\right) \\
d_h^2\mathbf{K}_2\left(h=0\right) &= \partial_{\mathbf{U}} D_i\left(\mathbf{U}^n + \left(1-\alpha\right)\mathbf{K}_1 + \alpha\mathbf{K}_2\right)\cdot \\
&\qquad \left[2\left(1-\alpha\right) D_i\left(\mathbf{U}^n + \alpha\mathbf{K}_1\right) + 2\alpha D_i\left(\mathbf{U}^n + \left(1-\alpha\right)\mathbf{K}_1 + \alpha\mathbf{K}_2\right)\right].
\end{aligned} \tag{4.100}$$

Now let us bring our attention back to equation (4.95). The first and second derivative of $\mathbf{U}^{n+1}$ are

$$d_h\mathbf{U}^{n+1} = \left(1-\alpha\right) d_h\mathbf{K}_1 + \alpha d_h\mathbf{K}_2 \tag{4.101}$$

$$d_h^2\mathbf{U}^{n+1} = \left(1-\alpha\right) d_h^2\mathbf{K}_1 + \alpha d_h^2\mathbf{K}_2, \tag{4.102}$$

respectively. Substituting the derivative values of (4.100), the zeroth to second derivatives of $\mathbf{U}^{n+1}$ at $\mathbf{U}^n$ or at $h = 0$ are

$$\mathbf{U}^{n+1}\big|_{h=0} = \mathbf{U}^n \tag{4.103}$$

$$\begin{aligned}
\partial_h\mathbf{U}^{n+1}\big|_{h=0} &= \left(1-\alpha\right) D_i\left(\mathbf{U}^n + \left(1-\alpha\right)\mathbf{K}_1 + \alpha\mathbf{K}_2\right) \\
&+ \alpha D_i\left(\mathbf{U}^n + \left(1-\alpha\right)\mathbf{K}_1 + \alpha\mathbf{K}_2\right)
\end{aligned} \tag{4.104}$$

$$\begin{aligned}
\partial_h^2\mathbf{U}^{n+1}\big|_{h=0} &= 2\alpha\left(1-\alpha\right)\partial_{\mathbf{U}} D_i\left(\mathbf{U}^n + \alpha\mathbf{K}_1\right) D_i\left(\mathbf{U}^n + \alpha\mathbf{K}_1\right) \\
&+ 2\alpha\left(1-\alpha\right)\partial_{\mathbf{U}} D_i\left(\mathbf{U}^n + \left(1-\alpha\right)\mathbf{K}_1 + \alpha\mathbf{K}_2\right)\cdot D_i\left(\mathbf{U}^n + \alpha\mathbf{K}_1\right) \\
&+ 2\alpha^2\partial_{\mathbf{U}} D_i\left(\mathbf{U}^n + \left(1-\alpha\right)\mathbf{K}_1 + \alpha\mathbf{K}_2\right)\cdot D_i\left(\mathbf{U}^n + \left(1-\alpha\right)\mathbf{K}_1 + \alpha\mathbf{K}_2\right)
\end{aligned} \tag{4.105}$$

respectively. Subsequently, the Taylor expansion of $\mathbf{U}^{n+1}$ at $h = 0$ is

$$\mathbf{U}^{n+1} = \mathbf{U}^n + \left(\partial_h \mathbf{U}^{n+1}\big|_{h=0}\right) h + \left(\partial_h^2 \mathbf{U}^{n+1}\big|_{h=0}\right) \frac{h^2}{2} + O\left(h^3\right), \tag{4.106}$$

which is an appropriate second-order model of the exact Taylor series (4.89) for certain α. By inspection of the first derivative (4.104), it is easy to see that $\partial_h \mathbf{U}^{n+1}\big|_{h=0}$ takes the form of a weighted mean of first derivatives, $D(\mathbf{U})$, for any chosen α since the coefficients of each term add to unity ($(1-\alpha)+\alpha = 1$). However, let us turn our attention to $\partial_h^2 \mathbf{U}^{n+1}\big|_{h=0}$ expressed by equation (4.105). All the terms in $\partial_h^2 \mathbf{U}^{n+1}\big|_{h=0}$ has the form $w_j \cdot \partial_{\mathbf{U}} D_i(\mathbf{U}) \cdot D_i(\mathbf{U})$, where w_j is a weight coefficient and $\partial_{\mathbf{U}} D_i(\mathbf{U}) \cdot D_i(\mathbf{U})$ is a second-derivative defined by $\mathbf{U}$ at different implicit points in time. However, in order for $\partial_h^2 \mathbf{U}^{n+1}\big|_{h=0}$ to truly be a weighted mean of second derivatives, all of the weight coefficients must add to unity,

$$\sum w_j = 2\alpha(1-\alpha) + 2\alpha(1-\alpha) + 2\alpha^2 = 1. \tag{4.107}$$

This condition can only be met for $\alpha = 1 \pm 1/\sqrt{2}$, which is found after solving for the roots of the quadratic equation. Any other α would make $\partial_h^2 \mathbf{U}^{n+1}\big|_{h=0}$ an arbitrary linear function of second derivatives. Note the similarities of equation (4.106) to the explicit Runge-Kutta Taylor expansion (4.94). They both represent second-order integration, except they differ by the first and second derivatives they use. The explicit Runge-Kutta scheme has its first and second derivatives defined explicitly by $\mathbf{U}^n$. The implicit Runge-Kutta scheme has its first and second derivatives defined by weighted means of first and second derivatives implicitly away from $\mathbf{U}^n$. As discussed in Section 4.6.3, the implicit method's use of derivatives away from the explicit point is a necessity to integrate over shorter time scale oscillations associated with the electron plasma frequency and gyrofrequency.

4.7.4 Implicit-Explicit second-order time integration: Richardson extrapolation

In Sections 4.7.2 and 4.7.3 second-order explicit and implicit integration were described in separate manners. In this section we describe a scheme (that EMI implements) for second-order accurate semi-implicit time integration, where both explicit and implicit integration are implemented. For semi-explicit time integration, the differential function, $D(\mathbf{U})$, takes the form

$$D(\mathbf{U}) = D_e(\mathbf{U}) + D_i(\mathbf{U}), \tag{4.108}$$

where $D_e(\mathbf{U})$ refers to the differential equations to be integrated explicitly and $D_i(\mathbf{U})$ refers to the differential equations to be integrated implicitly, as discussed in Section 4.6.3. With equation (4.108), the exact second-order Taylor expansion (4.89) can be expressed as

$$\begin{aligned}
\mathbf{U}^{n+1} = \mathbf{U}^n & \\
& + D_e(\mathbf{U})\, h \\
& + D_i(\mathbf{U})\, h \\
& + \partial_{\mathbf{U}} D_e(\mathbf{U}) \cdot D_e(\mathbf{U}) \frac{h^2}{2} \\
& + \partial_{\mathbf{U}} D_e(\mathbf{U}) \cdot D_i(\mathbf{U}) \frac{h^2}{2} \\
& + \partial_{\mathbf{U}} D_i(\mathbf{U}) \cdot D_e(\mathbf{U}) \frac{h^2}{2} \\
& + \partial_{\mathbf{U}} D_i(\mathbf{U}) \cdot D_i(\mathbf{U}) \frac{h^2}{2} \\
& + O\left(h^3\right).
\end{aligned} \tag{4.109}$$

The question remains: how is equation (4.109) modeled?

Second and higher order accurate IMEX schemes can be found in *Ascher et al.* (1997) and *Pareschi and Russo* (2000). They discuss clever ways to integrate with high-order accuracy. EMI uses a second-order Richardson extrapolation which can be described as

$$\mathbf{U}^{n+1} = \mathbf{U}^n + 2\mathbf{K}_2 - \mathbf{K}_3, \tag{4.110}$$

where

$$\mathbf{K}_1 = D_e\left(\mathbf{U}^n\right)\frac{h}{2} + D_i\left(\mathbf{U}^n + \mathbf{K}_1\right)\frac{h}{2}$$

$$\mathbf{K}_2 = \mathbf{K}_1 + D_e\left(\mathbf{U}^n + \mathbf{K}_1\right)\frac{h}{2} + D_i\left(\mathbf{U}^n + \mathbf{K}_2\right)\frac{h}{2}$$

$$\mathbf{K}_3 = D_e\left(\mathbf{U}^n\right)h + D_i\left(\mathbf{U}^n + \mathbf{K}_3\right)h.$$

The steps to implement the scheme is as follows:

1. Semi-implicitly integrate by an $h/2$ step.
2. From the $h/2$ point, semi-implicitly integrate another $h/2$ step, where $\mathbf{K}_2$ is determined (the difference between the current $\mathbf{U}$ and the original $\mathbf{U}^n$).
3. Go back to the original $\mathbf{U}^n$ and from that point, semi-implicitly integrate a full h step, where $\mathbf{K}_3$ is determined (the difference between the current $\mathbf{U}$ and the original $\mathbf{U}^n$).
4. $\mathbf{U}^{n+1}$ is computed as $\mathbf{U}^{n+1} = \mathbf{U}^n + 2\mathbf{K}_2 - \mathbf{K}_3$.

It can be shown that the scheme is second-order accurate; that is, the scheme models equation (4.109) appropriately. The first derivative of $\mathbf{K}_1$ is derived as

$$\mathbf{K}_1 = D_e\left(\mathbf{U}^n\right)\frac{h}{2} + D_i\left(\mathbf{U}^n + \mathbf{K}_1\right)\frac{h}{2}$$

$$2d_h\mathbf{K}_1 = D_e\left(\mathbf{U}^n\right) + D_i\left(\mathbf{U}^n + \mathbf{K}_1\right) + \partial_{\mathbf{U}}D_i\left(\mathbf{U}^n + \mathbf{K}_1\right)d_h\mathbf{K}_1 h$$

$$d_h\mathbf{K}_1 = \frac{D_e\left(\mathbf{U}^n\right) + D_i\left(\mathbf{U}^n + \mathbf{K}_1\right)}{2 - \partial_{\mathbf{U}}D_i\left(\mathbf{U}^n + \mathbf{K}_1\right)h}. \tag{4.111}$$

The second derivative is

$$d_h^2\mathbf{K}_1 = \frac{\partial_{\mathbf{U}} D_i\left(\mathbf{U}^n + \mathbf{K}_1\right) d_h\mathbf{K}_1}{2 - \partial_{\mathbf{U}} D_i\left(\mathbf{U}^n + \mathbf{K}_1\right) h} - \frac{\left[D_e\left(\mathbf{U}^n\right) + D_i\left(\mathbf{U}^n + \mathbf{K}_1\right)\right]\left[-\partial_{\mathbf{U}} D_i\left(\mathbf{U}^n + \mathbf{K}_1\right) - O(h)\right]}{\left[2 - O(h)\right]^2}. \tag{4.112}$$

The first derivative of $\mathbf{K}_2$ is derived as

$$\mathbf{K}_2 = \mathbf{K}_1 + D_e\left(\mathbf{U}^n + \mathbf{K}_1\right)\frac{h}{2} + D_i\left(\mathbf{U}^n + \mathbf{K}_2\right)\frac{h}{2}$$

$$2d_h\mathbf{K}_2 = 2d_h\mathbf{K}_1 + D_e\left(\mathbf{U}^n + \mathbf{K}_1\right) + D_i\left(\mathbf{U}^n + \mathbf{K}_2\right) + \left[\partial_{\mathbf{U}} D_e\left(\mathbf{U}^n + \mathbf{K}_1\right) d_h\mathbf{K}_1 + \partial_{\mathbf{U}} D_i\left(\mathbf{U}^n + \mathbf{K}_2\right) d_h\mathbf{K}_2\right] h$$

$$d_h\mathbf{K}_2 = \frac{2d_h\mathbf{K}_1 + D_e\left(\mathbf{U}^n + \mathbf{K}_1\right) + D_i\left(\mathbf{U}^n + \mathbf{K}_2\right) + \partial_{\mathbf{U}} D_e\left(\mathbf{U}^n + \mathbf{K}_1\right) d_h\mathbf{K}_1 h}{2 - \partial_{\mathbf{U}} D_i\left(\mathbf{U}^n + \mathbf{K}_2\right) h}. \tag{4.113}$$

The second derivative is

$$d_h^2\mathbf{K}_2 = \frac{2d_h^2\mathbf{K}_1 + 2\partial_{\mathbf{U}} D_e\left(\mathbf{U}^n + \mathbf{K}_1\right) d_h\mathbf{K}_1 + \partial_{\mathbf{U}} D_i\left(\mathbf{U}^n + \mathbf{K}_2\right) d_h\mathbf{K}_2 + O(h)}{2 - O(h)} - \frac{\left[2d_h\mathbf{K}_1 + D_e\left(\mathbf{U}^n + \mathbf{K}_1\right) + D_i\left(\mathbf{U}^n + \mathbf{K}_2\right) + O(h)\right]\left[-\partial_{\mathbf{U}} D_i\left(\mathbf{U}^n + \mathbf{K}_2\right) - O(h)\right]}{\left[2 - \partial_{\mathbf{U}} D_i\left(\mathbf{U}^n + \mathbf{K}_2\right) h\right]^2}. \tag{4.114}$$

The first derivative of $\mathbf{K}_3$ is derived as

$$\mathbf{K}_3 = D_e\left(\mathbf{U}^n\right) h + D_i\left(\mathbf{U}^n + \mathbf{K}_3\right) h$$

$$d_h\mathbf{K}_3 = D_e\left(\mathbf{U}^n\right) + D_i\left(\mathbf{U}^n + \mathbf{K}_3\right) + \partial_{\mathbf{U}} D_i\left(\mathbf{U}^n + \mathbf{K}_3\right) d_h\mathbf{K}_3 h \tag{4.115}$$

$$d_h\mathbf{K}_3 = \frac{D_e\left(\mathbf{U}^n\right) + D_i\left(\mathbf{U}^n + \mathbf{K}_3\right)}{1 - \partial_{\mathbf{U}} D_i\left(\mathbf{U}^n + \mathbf{K}_3\right) h}. \tag{4.116}$$

The second derivative is

$$
\begin{aligned}
d_h^2\mathbf{K}_3 = & \frac{\partial_{\mathbf{U}} D_i\left(\mathbf{U}^n+\mathbf{K}_3\right) d_h\mathbf{K}_3}{1-O(h)} \\
& - \frac{\left[D_e\left(\mathbf{U}^n\right)+D_i\left(\mathbf{U}^n+\mathbf{K}_3\right)\right]\left[-\partial_{\mathbf{U}} D_i\left(\mathbf{U}^n+\mathbf{K}_3\right)-O\left(h\right)\right]}{\left[1-O(h)\right]^2}.
\end{aligned}
\tag{4.117}
$$

The derivatives of $\mathbf{K}_1$, $\mathbf{K}_2$, and $\mathbf{K}_3$ at $h=0$ are

$$
\begin{aligned}
d_h\mathbf{K}_1\left(h=0\right) &= \frac{1}{2}\left[D_e\left(\mathbf{U}^n\right)+D_i\left(\mathbf{U}^n+\mathbf{K}_1\right)\right] \\
d_h\mathbf{K}_2\left(h=0\right) &= \frac{1}{2}\left[D_e\left(\mathbf{U}^n\right)+D_i\left(\mathbf{U}^n+\mathbf{K}_1\right)\right]+\frac{1}{2}\left[D_e\left(\mathbf{U}^n+\mathbf{K}_1\right)+D_i\left(\mathbf{U}^n+\mathbf{K}_2\right)\right] \\
d_h\mathbf{K}_3\left(h=0\right) &= \left[D_e\left(\mathbf{U}^n\right)+D_i\left(\mathbf{U}^n+\mathbf{K}_3\right)\right] \\
d_h^2\mathbf{K}_1\left(h=0\right) &= \frac{1}{2}\partial_{\mathbf{U}} D_i\left(\mathbf{U}^n+\mathbf{K}_1\right)\left[D_e\left(\mathbf{U}^n\right)+D_i\left(\mathbf{U}^n+\mathbf{K}_1\right)\right] \\
d_h^2\mathbf{K}_2\left(h=0\right) &= \frac{1}{2}\partial_{\mathbf{U}} D_e\left(\mathbf{U}^n+\mathbf{K}_1\right)\left[D_e\left(\mathbf{U}^n\right)+D_i\left(\mathbf{U}^n+\mathbf{K}_1\right)\right] \\
&\quad + \frac{1}{2}\partial_{\mathbf{U}} D_i\left(\mathbf{U}^n+\mathbf{K}_1\right)\left[D_e\left(\mathbf{U}^n\right)+D_i\left(\mathbf{U}^n+\mathbf{K}_1\right)\right] \\
&\quad + \frac{1}{2}\partial_{\mathbf{U}} D_i\left(\mathbf{U}^n+\mathbf{K}_2\right)\left[D_e\left(\mathbf{U}^n\right)+D_i\left(\mathbf{U}^n+\mathbf{K}_1\right)\right]. \\
&\quad + \frac{1}{2}\partial_{\mathbf{U}} D_i\left(\mathbf{U}^n+\mathbf{K}_2\right)\left[D_e\left(\mathbf{U}^n+\mathbf{K}_1\right)+D_i\left(\mathbf{U}^n+\mathbf{K}_2\right)\right] \\
d_h^2\mathbf{K}_3\left(h=0\right) &= 2\partial_{\mathbf{U}} D_i\left(\mathbf{U}^n+\mathbf{K}_3\right)\left[D_e\left(\mathbf{U}^n\right)+D_i\left(\mathbf{U}^n+\mathbf{K}_3\right)\right].
\end{aligned}
\tag{4.118}
$$

Now let us bring our attention back to equation (4.110). The first and second derivative of $\mathbf{U}^{n+1}$ are

$$
d_h\mathbf{U}^{n+1} = 2d_h\mathbf{K}_2 - d_h\mathbf{K}_3 \tag{4.119}
$$

$$
d_h^2\mathbf{U}^{n+1} = 2d_h^2\mathbf{K}_2 - d_h^2\mathbf{K}_3, \tag{4.120}
$$

respectively. Substituting the derivative values (4.118), the zeroth to second derivatives of $\mathbf{U}^{n+1}$ at

$\mathbf{U}^n$ or at $h = 0$ are

$$\begin{aligned}
\mathbf{U}^{n+1}\big|_{h=0} &= \mathbf{U}^n && (4.121)\\
\partial_h \mathbf{U}^{n+1}\big|_{h=0} &= D_e\left(\mathbf{U}^n + \mathbf{K}_1\right) && (4.122)\\
&+ D_i\left(\mathbf{U}^n + \mathbf{K}_1\right) + D_i\left(\mathbf{U}^n + \mathbf{K}_2\right) - D_i\left(\mathbf{U}^n + \mathbf{K}_3\right)\\
\partial_h^2 \mathbf{U}^{n+1}\big|_{h=0} &= \partial_{\mathbf{U}} D_e\left(\mathbf{U}^n + \mathbf{K}_1\right)\left[D_e\left(\mathbf{U}^n\right) + D_i\left(\mathbf{U}^n + \mathbf{K}_1\right)\right] && (4.123)\\
&+ \partial_{\mathbf{U}} D_i\left(\mathbf{U}^n + \mathbf{K}_1\right)\left[D_e\left(\mathbf{U}^n\right) + D_i\left(\mathbf{U}^n + \mathbf{K}_1\right)\right]\\
&+ \partial_{\mathbf{U}} D_i\left(\mathbf{U}^n + \mathbf{K}_2\right)\left[D_e\left(\mathbf{U}^n\right) + D_i\left(\mathbf{U}^n + \mathbf{K}_1\right)\right]\\
&+ \partial_{\mathbf{U}} D_i\left(\mathbf{U}^n + \mathbf{K}_2\right)\left[D_e\left(\mathbf{U}^n + \mathbf{K}_1\right) + D_i\left(\mathbf{U}^n + \mathbf{K}_2\right)\right]\\
&- 2\partial_{\mathbf{U}} D_i\left(\mathbf{U}^n + \mathbf{K}_3\right)\left[D_e\left(\mathbf{U}^n\right) + D_i\left(\mathbf{U}^n + \mathbf{K}_3\right)\right],
\end{aligned}$$

respectively. Subsequently, the Taylor expansion of $\mathbf{U}^{n+1}$ at $h = 0$ is

$$\mathbf{U}^{n+1} = \mathbf{U}^n + \left(\partial_h \mathbf{U}^{n+1}\big|_{h=0}\right) h + \left(\partial_h^2 \mathbf{U}^{n+1}\big|_{h=0}\right) \frac{h^2}{2} + O\left(h^3\right), \tag{4.124}$$

which is an appropriate second-order model of semi-implicit second-order Taylor series (4.109),

where the series (4.109) derivatives are modeled as

$$
\begin{aligned}
D_e\left(\mathbf{U}\right) &= D_e\left(\mathbf{U}^n + \mathbf{K}_1\right) && (4.125)\\
D_i\left(\mathbf{U}\right) &= D_i\left(\mathbf{U}^n + \mathbf{K}_1\right) + D_i\left(\mathbf{U}^n + \mathbf{K}_2\right) - D_i\left(\mathbf{U}^n + \mathbf{K}_3\right) && (4.126)\\
\partial_{\mathbf{U}} D_e\left(\mathbf{U}\right) \cdot D_e\left(\mathbf{U}\right) &= \partial_{\mathbf{U}} D_e\left(\mathbf{U}^n + \mathbf{K}_1\right) \cdot D_e\left(\mathbf{U}^n\right) && (4.127)\\
\partial_{\mathbf{U}} D_e\left(\mathbf{U}\right) \cdot D_i\left(\mathbf{U}\right) &= \partial_{\mathbf{U}} D_e\left(\mathbf{U}^n + \mathbf{K}_1\right) \cdot D_i\left(\mathbf{U}^n + \mathbf{K}_1\right) && (4.128)\\
\partial_{\mathbf{U}} D_i\left(\mathbf{U}\right) \cdot D_e\left(\mathbf{U}\right) &= \partial_{\mathbf{U}} D_i\left(\mathbf{U}^n + \mathbf{K}_1\right) \cdot D_e\left(\mathbf{U}^n\right) && (4.129)\\
&+ \partial_{\mathbf{U}} D_i\left(\mathbf{U}^n + \mathbf{K}_2\right) \cdot D_e\left(\mathbf{U}^n\right)\\
&+ \partial_{\mathbf{U}} D_i\left(\mathbf{U}^n + \mathbf{K}_2\right) \cdot D_e\left(\mathbf{U}^n + \mathbf{K}_1\right)\\
&- 2\partial_{\mathbf{U}} D_i\left(\mathbf{U}^n + \mathbf{K}_3\right) \cdot D_e\left(\mathbf{U}^n\right)\\
\partial_{\mathbf{U}} D_i\left(\mathbf{U}\right) \cdot D_i\left(\mathbf{U}\right) &= \partial_{\mathbf{U}} D_i\left(\mathbf{U}^n + \mathbf{K}_1\right) \cdot D_i\left(\mathbf{U}^n + \mathbf{K}_1\right) && (4.130)\\
&+ \partial_{\mathbf{U}} D_i\left(\mathbf{U}^n + \mathbf{K}_2\right) \cdot D_i\left(\mathbf{U}^n + \mathbf{K}_1\right)\\
&+ \partial_{\mathbf{U}} D_i\left(\mathbf{U}^n + \mathbf{K}_2\right) \cdot D_i\left(\mathbf{U}^n + \mathbf{K}_2\right)\\
&- 2\partial_{\mathbf{U}} D_i\left(\mathbf{U}^n + \mathbf{K}_3\right) \cdot D_i\left(\mathbf{U}^n + \mathbf{K}_3\right).
\end{aligned}
$$

Note that for each equation (4.125) through (4.130), the coefficients of the terms on the right-hand-side add to unity. Thus, the right-hand-side of each equation is a kind of weighted mean of derivatives (determined at different points) and is consistent with the left-hand-side that it models. If the coefficients on the right-hand-side did not add to unity, then the right-hand-side would be an arbitrary linear function of derivatives inconsistent with the left-hand-side that it models.

In this Richardson extrapolation scheme, the explicit and implicit integration are both implemented with second-order accuracy. Note that for each semi-implicit step, explicit integration should be applied before the implicit integration. In this order, the pair makes up a first-order semi-implicit step described in Subsection 4.6.3. It's worth noting that, without the presence of

implicit integration, it can be shown that this scheme produces the same results as the second-order explicit Runge-Kutta scheme described in Subsection 4.7.2.

4.8 Summary of EMI algorithm

To summarize, the EMI algorithm is as follows:

1. Initialize ionosphere
    (a) Use IRI-2007 for background plasma parameters (section 3.6).
    (b) Use NRLMSISE-00 for neutral parameters (section 3.6).
2. Time step
    (a) Flux limit for second-order spatial accuracy
        i. Use the Rusanov scheme for stable first-order intermediate flux (section 4.2).
        ii. Apply second-order corrections to the Rusanov scheme with a MUSCL scheme (section 4.3).
        iii. For curls, use a flux interpolated scheme (section 4.4.1) for zero-divergent curls.
    (b) Use second-order Richardson extrapolation scheme (section 4.7.4) for temporal integration.
3. Iteratively go back to step 2 for next time step.

Chapter 5

EMI code tests

Before using EMI to simulate and analyze the electromagnetic characteristics of low-latitude plasma irregularities, we will first check the model for consistency with analytical solutions to test problems. Specifically, EMI is checked for the support for Alfvén waves, the correct phase speed for Alfvén waves, and the numerical dissipation of Alfvén waves.

5.1 Support for Alfvén waves

In order to test the support for Alfvén waves, an Alfvén wave pulse (with an Alfvén speed set to 10^7 m/s) is simulated on a $50 \times 100 \times 50$ rectangular grid where the y-dimension is parallel to B_0. The simulation results are presented in Figure 5.1, where Sub-figures (a) through (f) plot $\mathbf{E}_1$ and $\mathbf{B}_1$ at times separated by 0.05 s. The cell lengths in the x and z dimensions are kilometer-scaled. Cell lengths in the y-dimension are tens of kilometers. The span of the y-dimension is thousands of kilometers, the length of magnetic field lines typically associated with low-latitudes plasma irregularities. This particular Alfvén wave is supported by E_{x1} and B_{z1}. It is apparent that it propagates along the y-dimension at the Alfvén speed; the wave travels 2500 km in 0.25 s. The results in Figure 5.1 show that, in fact, EMI supports Alfvén waves.

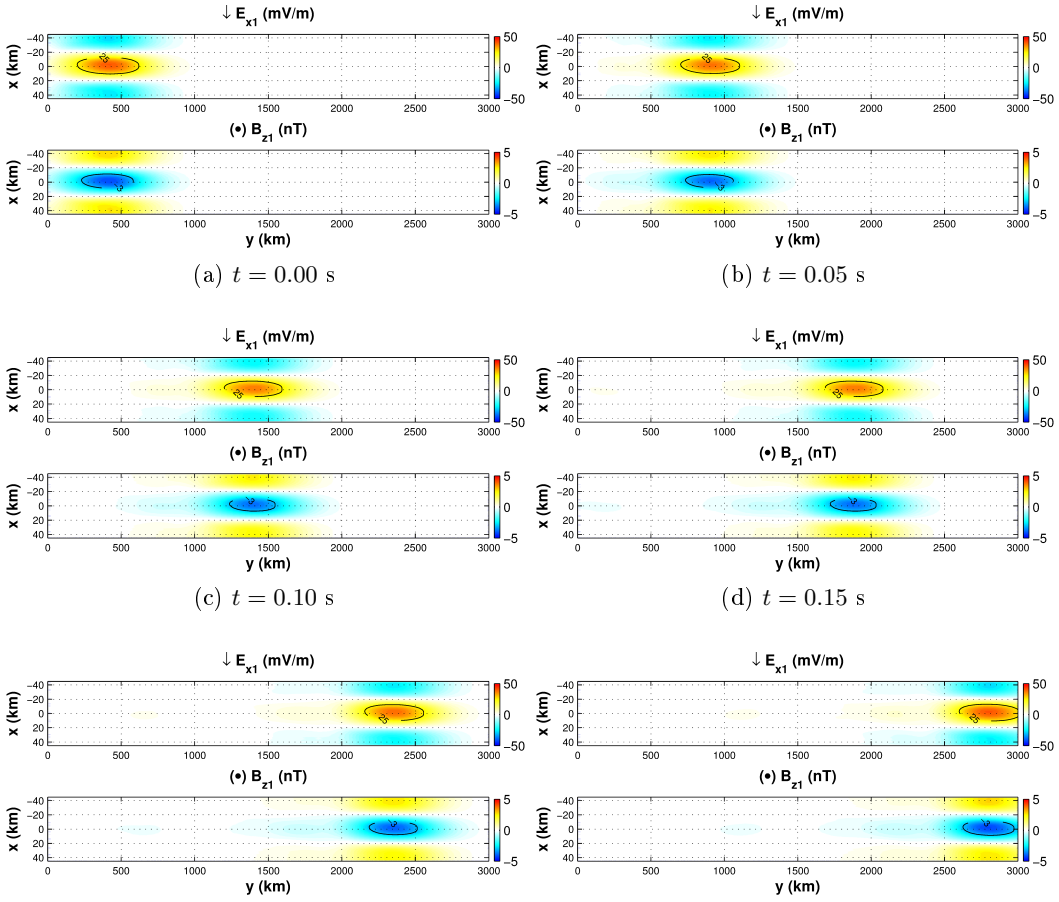

(a) $t = 0.00$ s (b) $t = 0.05$ s

(c) $t = 0.10$ s (d) $t = 0.15$ s

(e) $t = 0.20$ s (f) $t = 0.25$ s

Figure 5.1: Alfvén wave pulse propagating (in the y-direction) through time with $V_a = 10^7$ m/s. For each sub-figure, E_{x1} and B_{z1} are plotted.

5.2 Alfvén speed test

In Section 5.1, the support for Alfvén waves was shown. In this section, we excite several Alfvén waves with different V_a. According to linear theory, Alfvén waves should propagate at V_a (see Section 3.2). In Figure 5.2, the $\mathbf{E}_1$ of an example simulation is presented, where an Alfvén wave pulse (where $V_a = 10^7$ m/s in this particular simulation) is excited and propagates parallel to $\mathbf{B}_0$.

The x-axis indicates time in seconds. The y-axis indicates the distance along $\mathbf{B}_0$. The wave peak is fitted and traced by the solid black line. By fitting a line through the wave peak versus time, a the phase speed is calculated. As mentioned before, by linear theory, this phase speed should be equal to V_a, which is, in fact, true. The phase speeds versus V_a are plotted (marked with + signs) in Figure 5.3 for several simulations. Figure 5.3 shows that the phase speeds match V_a and are consistent with the linear wave theory.

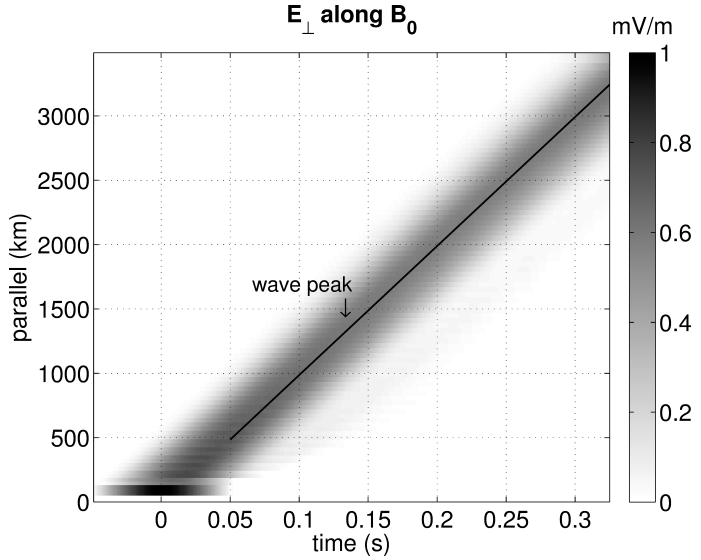

Figure 5.2: Alfvén wave pulse propagating parallel to $\mathbf{B}_0$ versus time for an Alfvén speed, $V_a = 10^7$ m/s. The solid line traces the wave peak, where the derivative of the line is the phase speed.

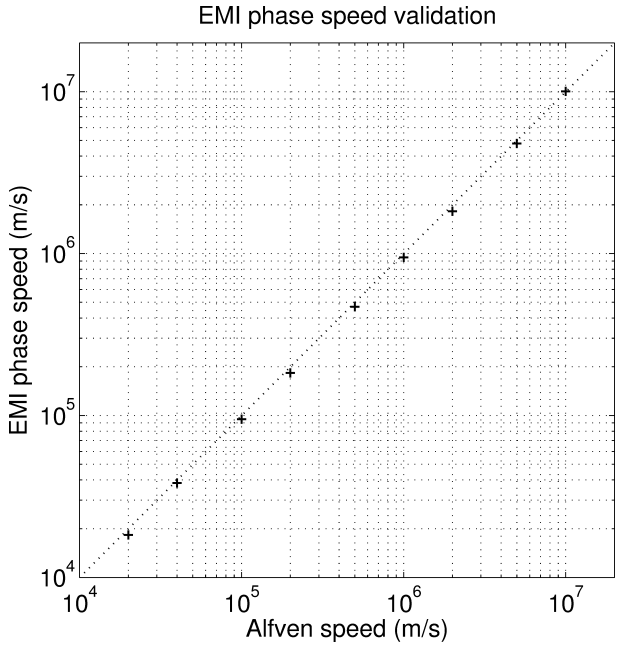

Figure 5.3: Phase speeds as simulated with EMI versus Alfvén speed.

5.3 Numerical dissipation

The inherent problem with the Rusanov scheme described in Section 4.2 is that it introduces numerical diffusion to the model for stability. In Section 4.3, second-order corrections are made to the Rusanov scheme to limit the numerical diffusion to an extent. While, numerical diffusivity is greatly diminished with the second-order corrections, numerical diffusivity still exists and can artificially dissipate the Alfvén wave modes of interest. To test EMI's dissipation, we simulate several Alfvén waves with different wavelengths over 1000's of km with 40 km cell spacing and measure the dissipation of the Alfvén wave amplitude. The results are plotted in Figure 5.4a, where the estimated e-fold distance is plotted versus cell points per wavelength. For waves resolved by 20 points or more, the wave dissipation e-fold distance is much greater than the 1000's of km lengths of interest. In other words, Alfvén wavelengths resolved by 20 cell points or more suffers minimally from numerical

dissipation. Furthermore, the natural dissipation of Alfvén waves from Pedersen conductivity (as determined by equation 3.67) exceeds the numerical dissipation at altitudes less than 300 km. The e-fold distances due to Pedersen conductivity is plotted in Figure 5.4b. The color plot plots the e-fold distance (in color in units of log km) versus both altitude and magnetic latitude. The e-fold distance (in units of log km) at the black solid line is plotted on the right by the black curve. It is apparent that the e-fold distance below 300 km is less than the 10000s km numerical e-fold distance for waves resolved by 20 points or more.

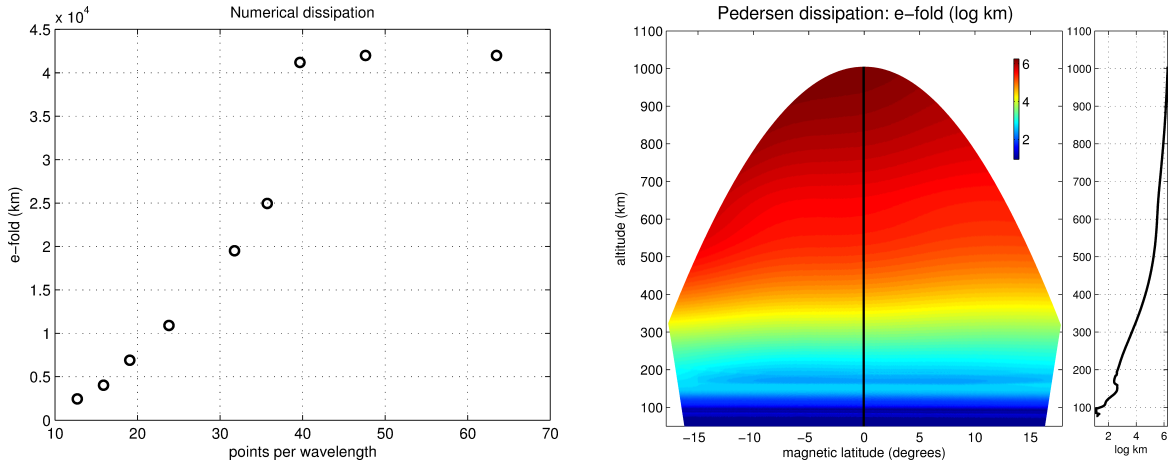

(a) Numerical dissipation.

(b) Pedersen conductivity dissipation.

Figure 5.4: Numerical dissipation of propagating Alfvén waves versus physical dissipation.

Chapter 6

Basic Alfvén wave dynamics

6.1 Alfvén wave interaction with change in Alfvén speeds

In this section, we show how Alfvén waves interact with discontinuities in Alfvén speed, V_a, as illustrated in Figure 6.1. This problem is described by an initial wave incident to the boundary that splits into a reflected wave and transmitted wave. Here, c_1 is Alfvén speed on the side of incidence and c_2 is the Alfvén speed on the other side of incidence. By equation (C.8) derived in the Appendix,

$$E_{reflected} = \frac{c_2 - c_1}{c_2 + c_1} \cdot E_{incident}, \tag{6.1}$$

where the E of the reflected and incident wave are indicated by the subscripts. For $c_1 < c_2$, the reflected wave is a positive reflection; that is, the E of the reflected wave has the same sign as the incident wave. For $c_1 > c_2$, the reflected wave is a negative reflection; that is, the E of the reflected wave has the opposite sign as the incident wave.

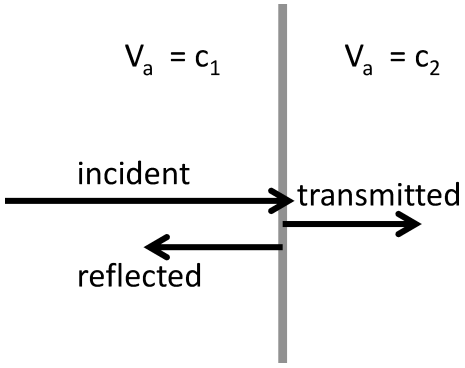

Figure 6.1: Diagram of an incident wave interacting with a change in Alfvén speed.

To illustrate this reflection, we simulate an Alfvén wave pulse encountering a negative change in V_a, as shown in Figure 6.2. Sub-figures (a) through (d) plot the $\mathbf{E}_1$ and $\mathbf{B}_1$ at $t = 0.00$ s, $t = 0.10$ s, $t = 0.20$ s, and $t = 0.30$ s, respectively. The black solid line at $y = 2700$ km, indicate change of Alfvén speed from $c_1 = 10^7$ m/s to $c_1 = 10^6$ m/s. The incident wave has a positive E_{x1} and propagates to the right from $t = 0.00$ s to $t = 0.20$ s. After $t = 0.20$ s, a reflected wave propagates to the left. Consistent with equation (6.1), the reflected wave has a negative E_{x1}. A negative change in Alfvén speed results in a negative reflection.

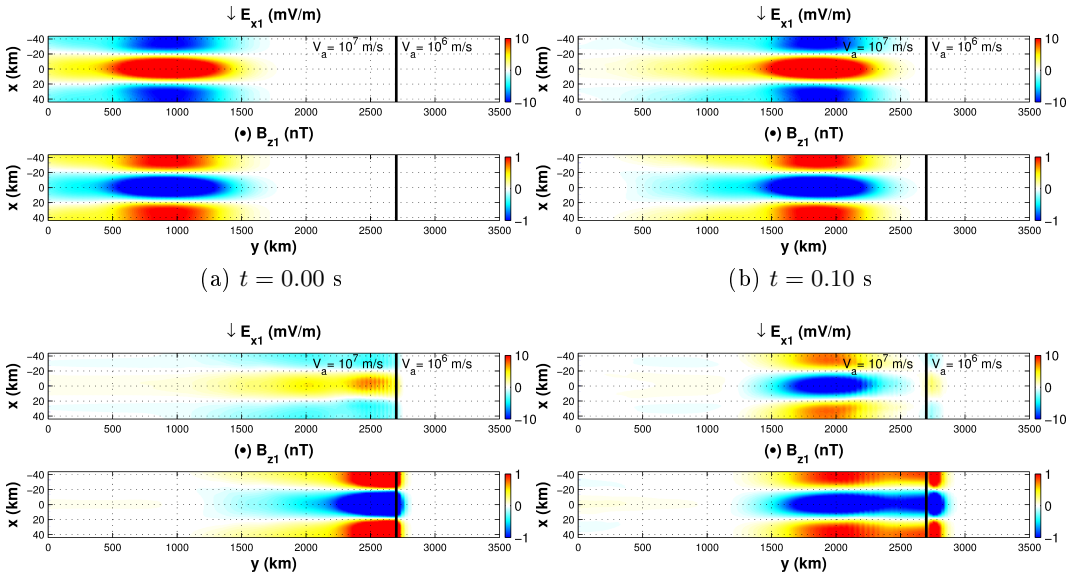

(a) $t = 0.00$ s (b) $t = 0.10$ s

(c) $t = 0.20$ s (d) $t = 0.30$ s

Figure 6.2: Alfvén interaction with a negative change in V_a.

We simulate an Alfvén wave pulse encountering a positive change in V_a, as presented in Figure 6.3. Sub-figures (a) through (d) plot the $\mathbf{E}_1$ and $\mathbf{B}_1$ at $t = 0.00$ s, $t = 0.10$ s, $t = 0.20$ s, and $t = 0.30$ s, respectively. The black solid line at $y = 2700$ km, indicate change of Alfvén speed from $c_1 = 10^7$ m/s to $c_1 = 10^8$ m/s. The incident wave has a positive E_{x1} and propagates to the right from $t = 0.00$ s to $t = 0.20$ s. After $t = 0.20$ s, a reflected wave propagates to the left. Consistent with equation (6.1), the reflected wave has a positive E_{x1}. A positive change in Alfvén speed results in a positive reflection.

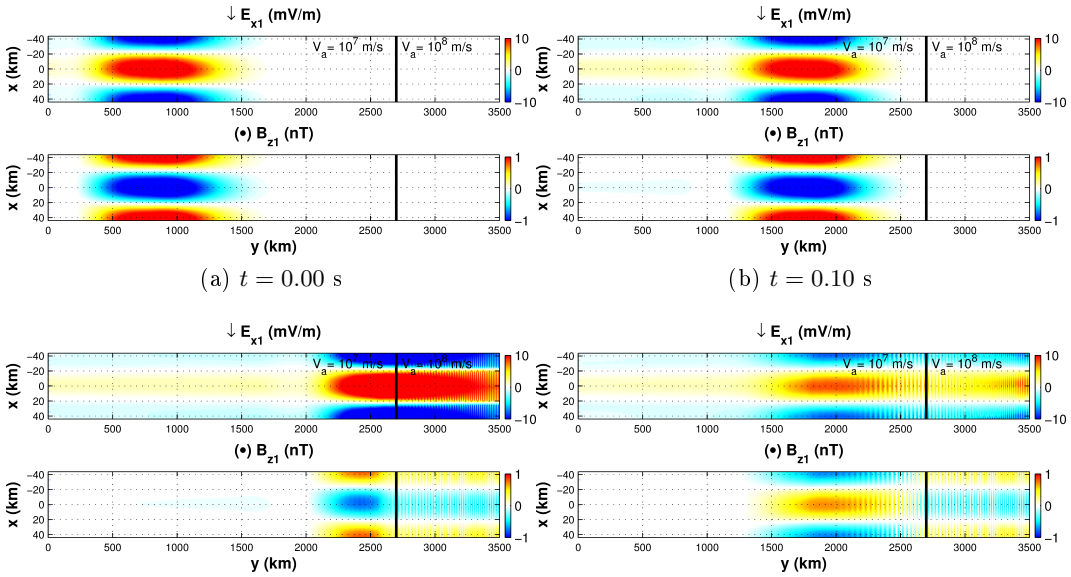

(a) $t = 0.00$ s (b) $t = 0.10$ s

(c) $t = 0.20$ s (d) $t = 0.30$ s

Figure 6.3: Alfvén interaction with a positive change in V_a.

6.2 Alfvén wave interaction with high transverse conductors

In this section, we show how Alfvén waves interact with high transverse conductors as illustrated in Figure 6.4. Here, "transverse" refers to dimensions perpendicular to the direction of wave propagation. This problem is described by an initial wave incident to the boundary that splits into a reflected wave and transmitted wave. Here, we consider a wave propagating with zero transverse conductivity to a region with high transverse conductivity.

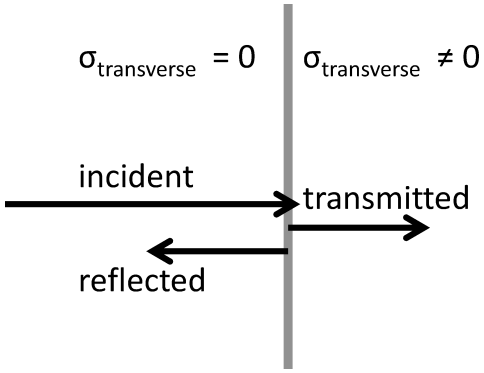

Figure 6.4: Diagram of an incident wave interacting with an interface with high transverse conductivity

For consistency at the interface, the sum of E on the incident side of the interface must equal to the sum E on the other side of interface. This is expressed as

$$E_{incident} + E_{reflected} = E_{transmitted}. \tag{6.2}$$

where the E of the reflected, transmitted, and incident wave are indicated by the subscripts. When encountering a high transverse conductor, $E_{transmitted} \sim 0$, as the conductor shorts out the electric field. Subsequently, the interaction results in a negative reflection; that is, the reflected wave has an electric field with a sign opposite to that of the incident wave.

We simulate an Alfvén wave pulse encountering a transverse conductor, presented in Figure 6.5. Sub-figures (a) through (e) plot the $\mathbf{E}_1$ and $\mathbf{B}_1$ at $t = 0.00$ s, $t = 0.10$ s, $t = 0.20$ s, $t = 0.30$ s, and $t = 0.40$ s, respectively. The black solid line at $y = 2700$ km, indicate change of transverse conductivity from $\sigma = 0$ mho/m to $\sigma = 10^{-5}$ mho/m. The incident wave has a positive E_{x1} and propagates to the right from $t = 0.00$ s to $t = 0.20$ s. After $t = 0.20$ s, a reflected wave propagates to the left. The reflected wave has a negative E_{x1}, showing how the interaction with transverse conductivity result in negative reflections.

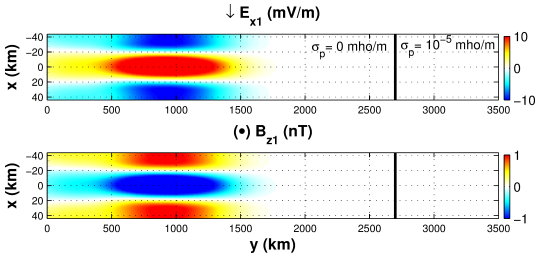

(a) $t = 0.00$ s

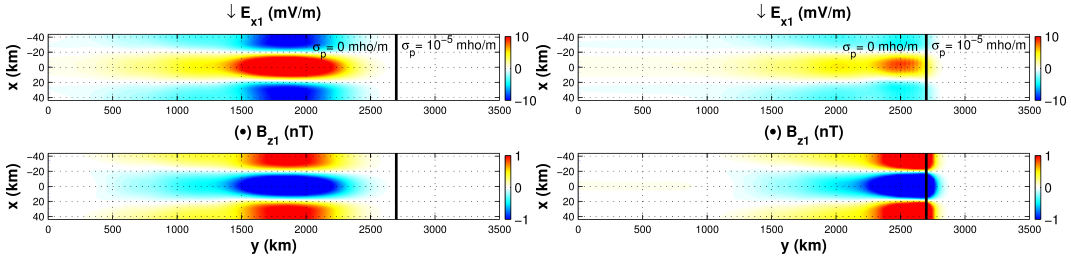

(b) $t = 0.10$ s

(c) $t = 0.20$ s

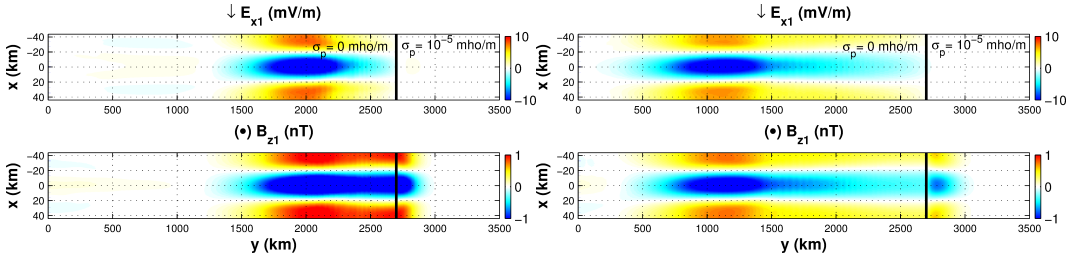

(d) $t = 0.30$ s

(e) $t = 0.40$ s

Figure 6.5: Alfvén interaction with a large transverse conductor.

Chapter 7

Rayleigh-Taylor Alfvén wave generator

In this chapter, we present several simulations of the Alfvénic dynamics that result from given density bubbles in the F region. The simulations presented are cast on a $100 \times 100 \times 100$ point rectangular grid in magnetic dipole coordinate space. Cells are spaced by kilometers in the perpendicular direction and by tens of kilometers in the parallel direction. We model the background ionosphere with the 2007 International Reference Ionosphere (IRI-2007) model (*Bilitza and Reinisch*, 2008) for ion density, ion composition, ion temperature, and electron temperature. Specifically, we model the background ionosphere at 0° magnetic longitude (near −77° geographic longitude) during 1 June 2008. We use the NRLMSISE-00 model (*Picone et al.*, 2002) for neutral densities and composition. We compute the collision frequencies using expressions from *Kelley* (2009). In this chapter, for simplicity's sake, we examine the cold plasma Alfvénic dynamics; that is, we impose $T_i = T_e = 0$ K. We will refer to x as magnetically zonal, y as being parallel to Earth's magnetic field, and z as meridional or magnetically vertical (in the direction with increasing L-shell). Subscripts x, y, and z denote vector components in the x, y, and z directions, respectively.

7.1 Off-equator bubbles with symmetry about the equator

Our first simulation is initialized with a plasma depletion shown in Figure 7.1 (top left) where each slice, a through f, is a perpendicular slice of the same set of magnetic fields, as indicated by the slice key (top middle). Slice a is at the magnetic equator while slice f is farthest from the equator and dips into the E region. The bubble has a 50 km scale length in the perpendicular directions and 400 km scale length along Earth's magnetic field. To save half of the computational time, we impose a symmetric boundary at the equator and simulate the northern hemisphere. With the symmetric boundary, simulating one hemisphere effectively simulates both hemispheres. The implication is that all of the simulated physics are mirrored in the complimentary hemisphere. The ion density is effectively constant in this simulation where we only simulate 30 seconds. According to the flux-tube-integrated formalism introduced by *Haerendel* (1973), equatorial irregularities are expected to grow on time scales of at least tens of minutes, which are much longer than the tens of seconds we simulate. Although a density bubble found in nature would already have internally developed $\mathbf{E}_1$ and $\mathbf{B}_1$, we initialized both $\mathbf{E}_1$ and $\mathbf{B}_1$ as zero. This scenario allows us to study the Alfvénic wave dynamics most clearly. Initially zero $\mathbf{E}_1$ and $\mathbf{B}_1$ may also apply to the tops of rising bubbles that introduce density depletions into regions where $\mathbf{E}_1$ and $\mathbf{B}_1$ have not yet developed.

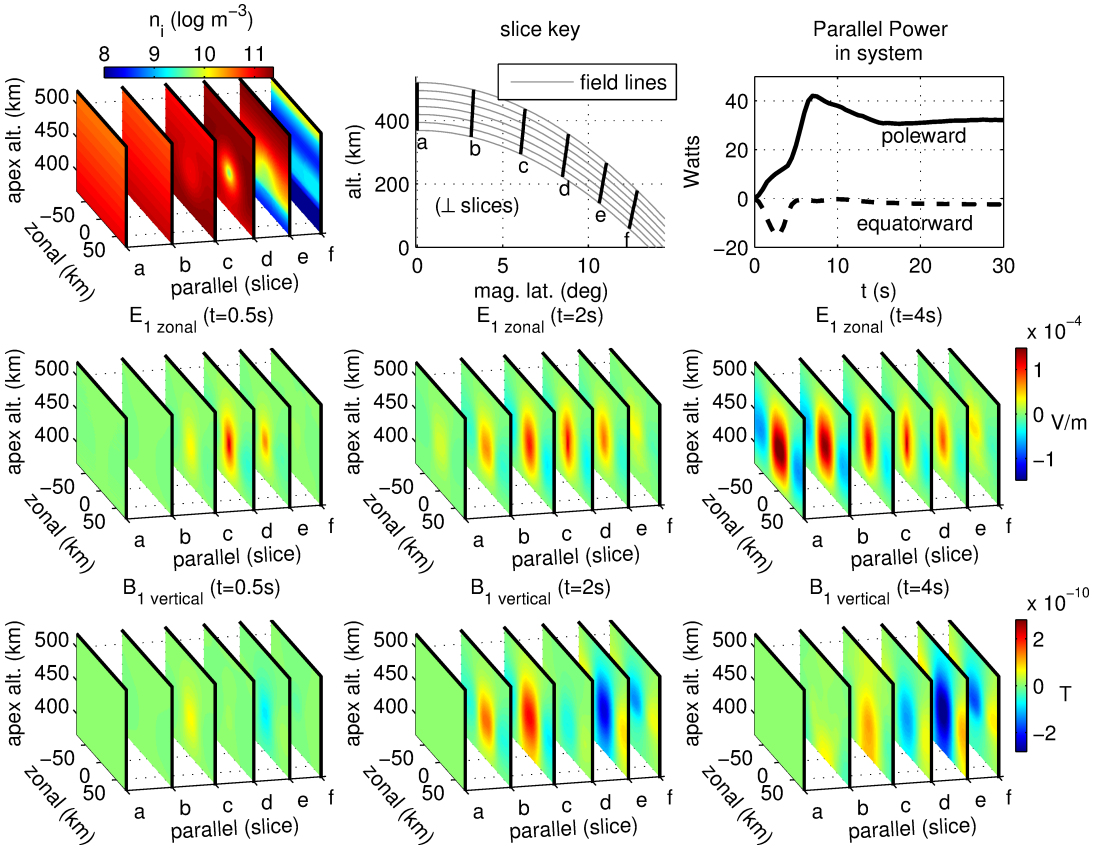

Figure 7.1: Launching Alfvén waves. Simulation results of a density depletion (top left subplot) centered near slice d off the equator. Slices a through f correspond to perpendicular slices of the same set of magnetic fields as indicated by the slice key (top middle). E_{1x} (middle row) and B_{1z} (bottom row) are plotted for times 0.5, 2.0, and 4.0 seconds from left to right. On the top right, the total power going poleward (solid line) and equatorward (dashed line) are plotted vs. time.

In Figure 7.1, we simulate the gravitational generalized Rayleigh-Taylor mode and ignore pressure forces. The middle and bottom rows of Figure 7.1 show the perturbation zonal electric field (E_{1x}) and meridional magnetic field (B_{1z}), respectively, at 0.5, 2.0, and 4.0 seconds from left to right. E_{1y}, E_{1z}, B_{1x}, and B_{1y} are insignificant. As shown at 0.5 s, zonal electric fields initially develop locally within the depletion due to an anti-zonal divergence of gravity-driven currents as classic gravitational Rayleigh-Taylor theory dictates. As time progresses, Alfvén waves are trans-

mitted poleward and equatorward, away from the bubble, as shown at 2.0 s and evidenced by the progression of zonal electric fields farther along the field lines and by the Poynting vector direction ($\mathbf{E}_1 \times \mathbf{B}_1$ direction). Given zonal electric fields, meridional (anti-meridional) magnetic fields indicate southward (northward) propagating Alfvén waves. At 4.0 s, the southward propagating waves meet with the imposed reflecting boundary at the equator. At this moment, it is as if the waves from the northern hemisphere mix with mirrored waves from the southern hemisphere propagating northward. The result is a net canceling of Poynting flux, as evidenced by the lack of significant B_{1z} in slices a and b.

The top right of Figure 7.1 plots the total Poynting power poleward (solid line) and equatorward (dashed line) in the system versus time, thus indicating how much Alfvénic energy is directed poleward and equatorward at different times. Initially, Alfvénic power increases poleward and equatorward as Alfvén waves emit away from the bubble. Shortly after 3 seconds, equatorward Alfvén waves from both hemispheres reach across the equator, as seen by the decreasing equatorward Poynting flux when the colliding waves start canceling out their power. These waves eventually travel past the transequator depletion and contribute to the poleward flux, as seen by the acceleration of poleward power at around 4 seconds. These Alfvén waves bounce back and forth within the system, but the system reaches an approximately steady state after 15 seconds. In other words, the system becomes electrostatic. The electrostatic properties will be discussed in Section 8.1.

Figure 7.2 shows the zonal electric field on the magnetic field line that intersects the center of the bubble. In this figure, the southern hemisphere (to the left of point a) is inferred from the reflection of the simulated northern hemisphere. Initially, zonal electric fields develop in both hemispheres at points $-d$ and d. As time progresses, zonal electric fields are launched toward the equator via Alfvén waves from both hemispheres. At 4 seconds, zonal electric fields from both hemispheres constructively form a maximum at the equator as the launched Alfvén waves from each hemisphere meet. Afterward, these waves pass each other and continue their way across the

equator into the opposite hemisphere, where they originated. At around 6 seconds, they reach the transequator bubbles and form maximums of 0.2 mV/m near $-d$ and d. After 6 seconds, they pass the transequator bubbles and reach the E region where increasing perpendicular conductivity absorbs the Alfvén waves. A majority of the waves are absorbed, but the remainder reflect and begin the second leg of their round trip. The waves bounce back and forth between hemispheres while being absorbed by transverse conductivity. Eventually, an approximate steady state is reached after 15 seconds. As mentioned before, this reaching of an approximate steady state is also evident from the Poynting power in Figure 7.1. Both Figures 7.1 and 7.2 clearly show that the Alfvénic time scale is on the order of seconds to tens of seconds.

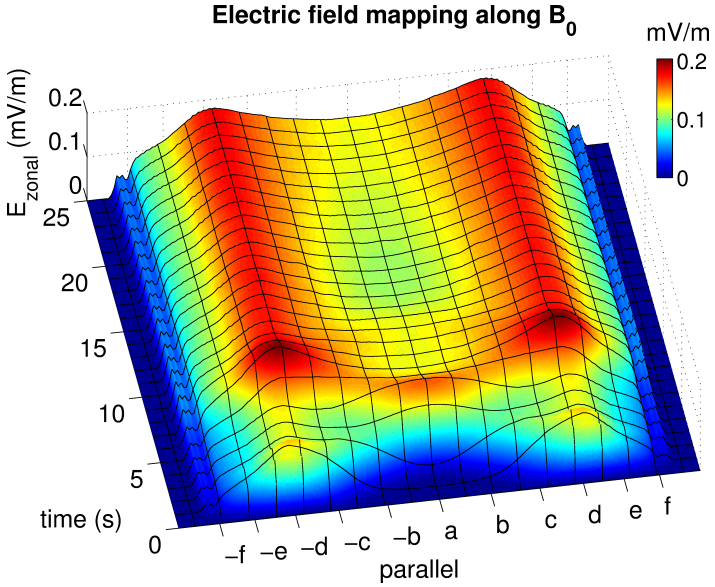

Figure 7.2: Zonal electric field mapping along the field line that intersects through the center of the bubble vs. time (seconds).

7.2 Off-equator bubbles with asymmetry about the equator

In Section 7.1, we presented the generation of Alfvén waves from the gravitational Rayleigh Taylor mode while imposing a symmetric boundary at the equator. This implied two identical bubbles in

the symmetric hemispheres. Between the two bubbles, their respective B_{1z} and Poynting flux cancel each other. In order to sort the B_{1z} of each bubble, it is instructive to simulate one bubble at a time. In this section we simulate the gravitational Rayleigh Taylor mode allowing for asymmetry about the equator. More specifically, we present two simulations. In one simulation there is a density bubble solely in the southern hemisphere as presented in Figure 7.3a. In the other simulation there is a density bubble solely in the northern hemisphere as presented in Figure 7.3b. For the Figures presented in this section, each slice, a through f, is a perpendicular slice of the same set of magnetic fields, as indicated by the slice key (top middle). Slice a is at the magnetic equator while slice f is farthest from the equator and dips into the E region.

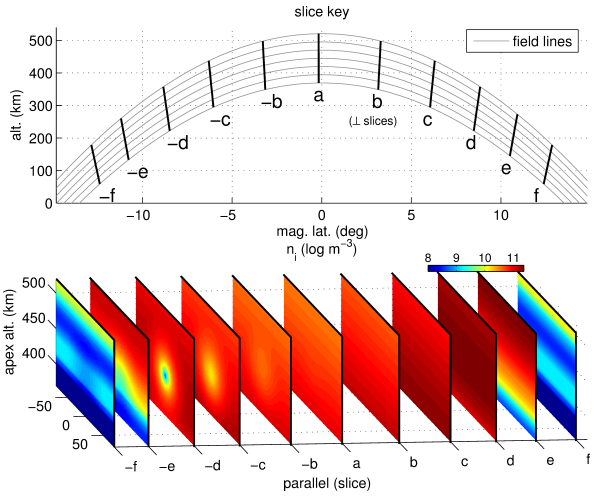

(a) Simulation setup for a bubble in southern hemisphere without symmetry at the equator.

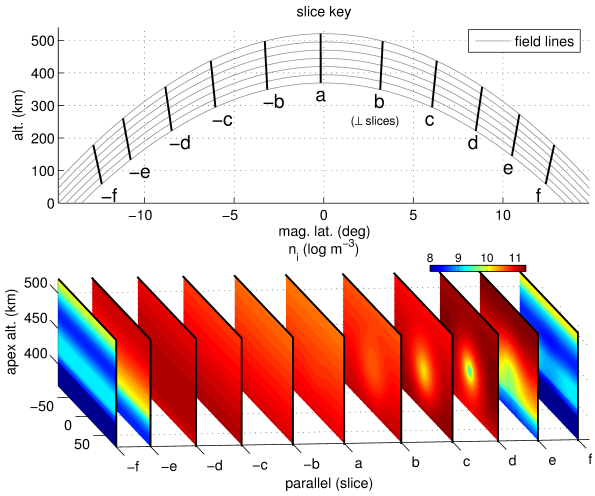

(b) Simulation setup for a bubble in northern hemisphere without symmetry at the equator.

Figure 7.3: Slice keys for a bubble in southern (a) and northern hemisphere (b).

The dynamics are similar to that of the simulation shown in Section 7.1, except that we can sort out the Alfvén waves generated from a northern bubble versus a southern bubble. In Figures 7.4a and 7.4c, plotted are the zonal electric and meridional magnetic field along the field line that goes through the density bubble at the southern hemisphere versus time. Within the bubble between slices $-c$ and

$-d$, zonal polarization electric fields develop due to a divergence of gravity-driven currents. Shortly after, the bubble emits out zonal electric field away from itself along Earth's magnetic field lines via Alfvén waves. Significant electric field is transmitted to the northern hemisphere accompanied with negative B_{z1} via Alfvén waves all the way to slice f in about 20 seconds. A steady state is reached after ~ 30 seconds. The Alfvénic timescale is of the same order of magnitude with the simulation presented in Section 7.1, which reached an approximate steady-state after ~ 15 seconds.

In Figures 7.4b and 7.4d, plotted are the zonal electric and meridional magnetic field along the field line that goes through the density bubble at the northern hemisphere versus time. Within the bubble between slices c and d, zonal polarization electric fields develop due to a divergence of gravity-driven currents. Shortly after, the bubble emits out zonal electric away from itself along Earth's magnetic field lines via Alfvén waves. Significant electric field is transmitted to the southern hemisphere accompanied with positive B_{z1} via Alfvén waves all the way to slice $-f$ in about 20 seconds. A steady state is reached after ~ 30 seconds. The Alfvénic timescale is of the same order of magnitude with the simulation presented in Section 7.1, which reached an approximate steady-state after ~ 15 seconds. However, the time at which steady-state is reached is roughly two times longer because symmetry was not imposed at the magnetic equator. The maximum electric field in Figure 7.4b is slightly different that in Figure 7.4a due to the slight asymmetry of the background ionosphere.

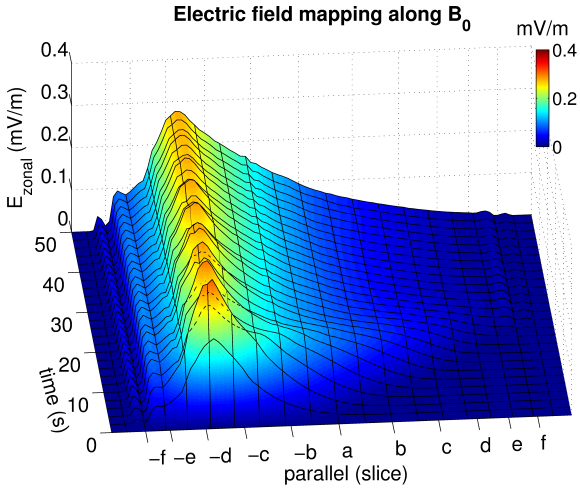

(a) E_{x1} for a bubble in the southern hemisphere.

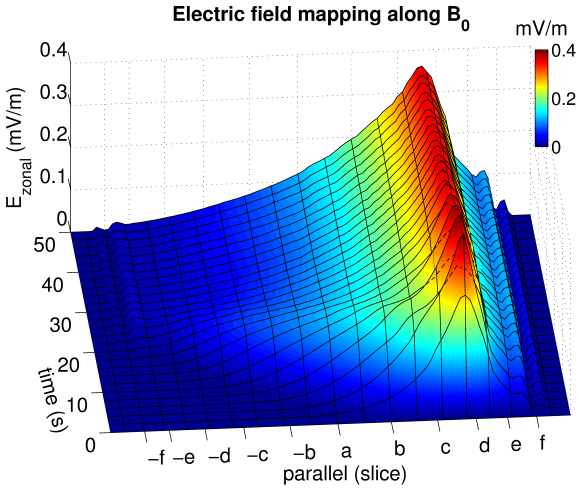

(b) E_{x1} for a bubble in the northern hemisphere.

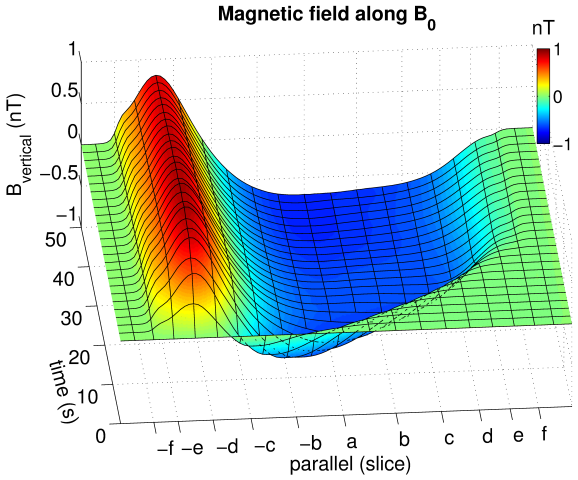

(c) B_{z1} for a bubble in the southern hemisphere.

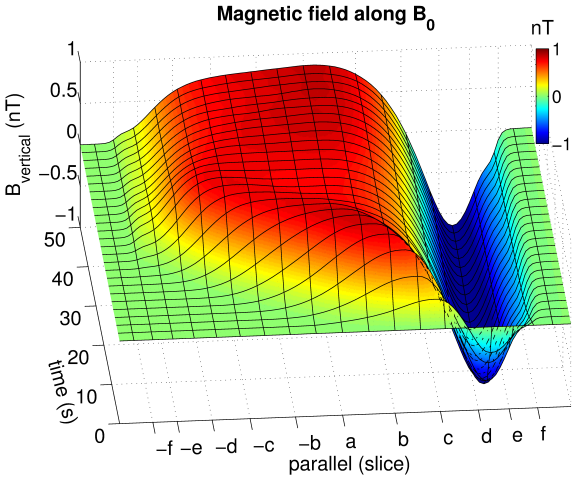

(d) B_{z1} for a bubble in the northern hemisphere.

Figure 7.4: The zonal electric and meridional magnetic field along the field line that intersect the center of the bubble in the southern/northern hemisphere. For (a) and (c), slices $-f$ through f correspond to the slice key in Figure 7.3a. For (b) and (d), slices $-f$ through f correspond to the slice key in Figure 7.3b

Allowing for asymmetry, the electric field dynamics are qualitatively similar to when imposing symmetry at the equator. However, the biggest difference between the symmetric simulation and the asymmetric simulations is the magnetic field at the equator. Symmetry results in cancellation

of magnetic fields at the equator because the northern hemisphere bubble transmits a positive B_{z1}, while the implied southern hemisphere bubble transmits a B_{z1} that equal in magnitude, but negative.

Note that although there is no ion depletion at the equator (slice a) for both of the simulations presented in Figures 7.4a and 7.4b, bubbles off the equator do map zonal electric fields remotely via Alfvén waves. This highlights the limitation of classic Rayleigh-Taylor theory that neglects the parallel dimension, which can only describe the physics of bubbles that stretch along whole field lines. That off-equator bubbles map electric fields to the equator is argued in both *Burke et al.* (2012) and *Dao et al.* (2012). Off-equator disturbances mapping electric fields to the equator have already been explored with 3-D fluid models utilizing 2-D electric fields (where Earth's magnetic field lines are treated as equipotential), as in the work by *Krall et al.* (2011). We show that 3-D electromagnetic fields also support this remote mapping. However, we must recognize that the electric field mapping is not perfect as the equipotential field line approximation suggests which is discussed further in Section 8.5.

7.3 Bubble centered at the equator

In Sections 7.1 and 7.2, we simulated bubbles off the equator. In this section we simulate the gravitational Rayleigh Taylor mode for a bubble at the magnetic equator. The simulation setup is shown in Figure 7.5a. Slice, $-f$ through f, is a perpendicular slice of the same set of magnetic fields, as indicated by the slice key (top middle). Slice a is at the magnetic equator while slice f is farthest from the equator and dips into the E region.

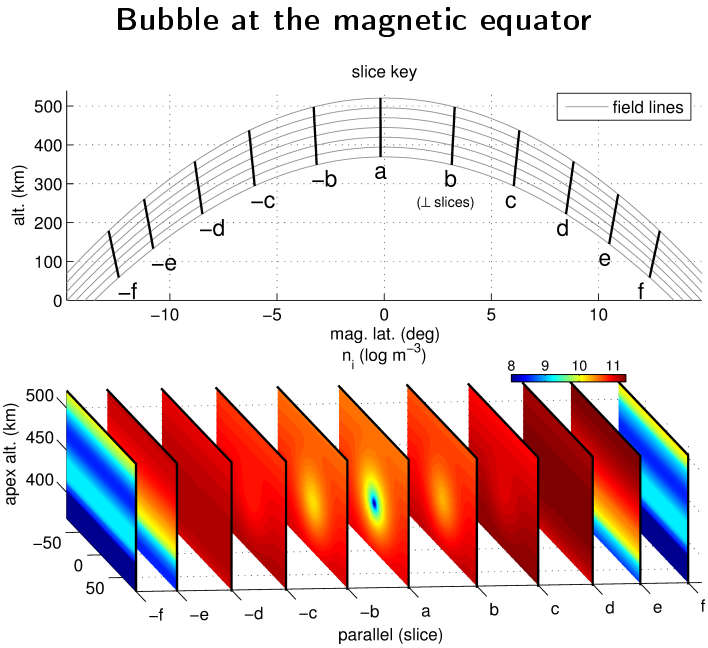

(a) Simulation setup for a bubble at the equator.

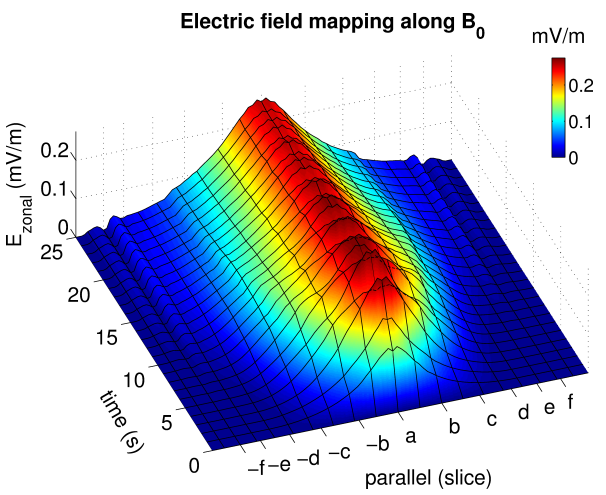

(b) E_{x1} for a bubble at the equator.

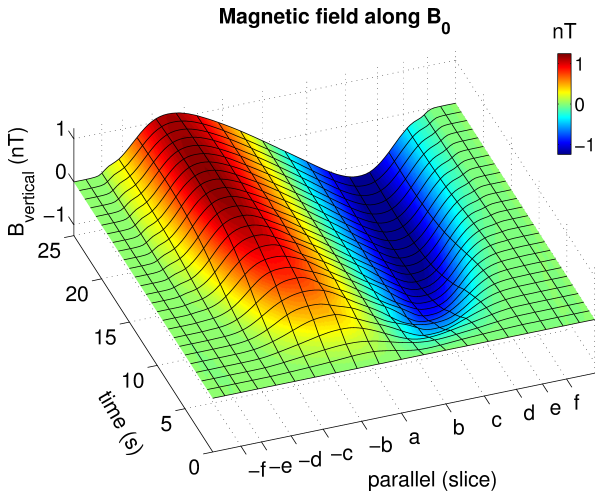

(c) B_{z1} for a bubble at the equator.

Figure 7.5: The zonal electric field (b) and meridional magnetic field (c) along the field line that intersect the center of the bubble at the magnetic equator. Slices $-f$ through f correspond to the slice key in (a).

The dynamics are similar to that of the simulation shown in Sections 7.1 and 7.2. In Figure

7.5b and 7.5c, plotted are the zonal electric and meridional magnetic field, respectively, along the field line that goes through the density bubble at the southern hemisphere versus time. Within the bubble, at slice a, zonal polarization electric fields develop due to a divergence of gravity-driven currents. Shortly after, the bubble emits out zonal electric field away from itself along Earth's magnetic field lines via Alfvén waves. On the northern side of the bubble, the zonal electric field is accompanied with negative B_{z1} consistent with poleward Poynting flux. On the southern side, the zonal electric field is accompanied with positive B_{z1} consistent with poleward Poynting flux. Significant electric field is transmitted to both poleward sides via Alfvén waves all the way to slice f in about 10 seconds. A steady state is reached after ~ 15 seconds. The Alfvénic timescale is of the same order of magnitude with the simulation presented in Sections 7.1 and 7.2, which reached an approximate steady-state after $15 - 30$ seconds.

7.4 Conclusions

The simulations presented in this chapter explore the electrodynamic processes that lead to the electrostatic state of the Rayleigh-Taylor mode. Polarization electric field developed within bubbles are transmitted away from the bubble to the E region along Earth's magnetic field lines via Alfvén waves. In the E region, these waves get absorbed by high transverse conductivity. The simulations show that the generalized Rayleigh-Taylor mode can take tens of seconds to reach an approximately electrostatic state. These electrodynamic time scales will, of course, vary with the ion mass density as well as the length of the magnetic field line on which the ion density bubble resides.

The magnetic signature associated with these waves is a B_{z1} on the order of 0.1 nT, which is roughly consistent with *Basu* (2005). This is detectable by sensitive magnetometers on-board satellites. With the combined measurements of E_{x1} and B_{z1}, we can theoretically compute the asymmetry of density depletion on either side of the point of measurement. If we measure zero B_{z1}, we can infer that there is equal depletion on both sides of the point, as with all of the simulations

in this chapter. On the other hand, asymmetry about the point of measurement results in a net Poynting flux. Negative B_{z1} indicate more power coming from the south. Positive B_{z1} indicate more power coming from the north. The side from which the net power is coming indicates which side has the larger depletion. This is useful in pinpointing where a plasma irregularity may be from a single measurement on a magnetic field line. Measuring $\mathbf{E}_1$ at the equator can identify that a plasma irregularity exists somewhere ambiguously along the intersecting magnetic field line. Additionally measuring $\mathbf{B}_1$ can hone in on the irregularity and determine on which side of the point of measurement the irregularity exists.

Chapter 8

Static electromagnetic characteristics of plasma irregularities

In this chapter, we present several simulations of the electrostatic characteristics given a density bubble in the F region. The simulations presented are cast on a $100 \times 100 \times 100$ point rectangular grid in magnetic dipole coordinate space. Perpendicular cell walls are on the order of kilometers while the parallel cell walls are on the order of tens of kilometers. We model the background ionosphere with the 2007 International Reference Ionosphere (IRI-2007) model (*Bilitza and Reinisch*, 2008) for ion density, ion composition, ion temperature, and electron temperature. Specifically, we model the background ionosphere at 0° magnetic longitude (near -77° geographic longitude) during 1 June 2008. We use the NRLMSISE-00 model (*Picone et al.*, 2002) for neutral densities and composition. We compute the collision frequencies from *Kelley* (2009). We will refer to x as magnetically zonal, y as being parallel to Earth's magnetic field, and z as meridional or magnetically vertical (in the direction with increasing L-shell). Subscripts x, y, and z denote vector components in the x, y, and z directions, respectively.

8.1 Electrostatic Rayleigh-Taylor current circulation: symmetry about the equator

We direct our attention to the electrostatic state of the gravitational Rayleigh-Taylor mode in Section 7.1. As indicated by the power subplot in Figure 7.1, an approximately electrostatic state is reached after 15 seconds. We show this electrostatic state in Figure 8.1. In the top three rows we present n_i, E_{1x}, and B_{1z} on the field lines with 425 km apex altitude plotted versus zonal and parallel distance, where the solid lines a through f correspond to the slices in Figure 7.1. E_{1y}, E_{1z}, B_{1x}, and B_{1y} are insignificant. By applying the steady-state Ampere's law on $\mathbf{B}_1$, we calculate the zonal currents J_{x1} and parallel currents J_{y1} shown on the bottom two rows with color. Overlayed on these plots are arrows indicating the clockwise current flow.

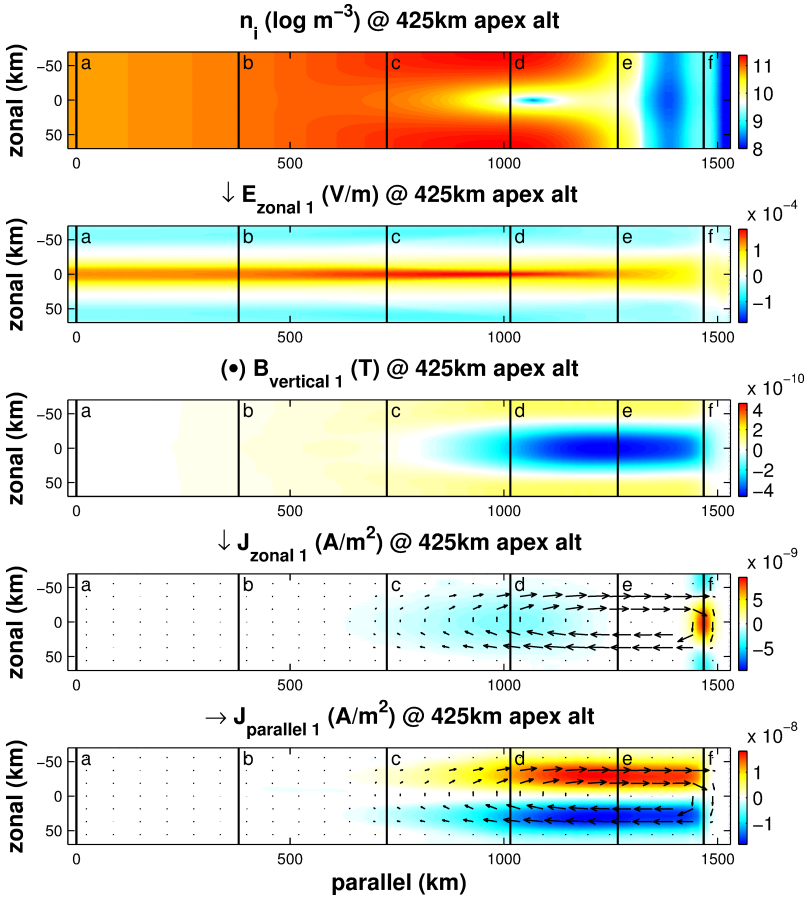

Figure 8.1: Electrostatic generalized Rayleigh-Taylor currents. From top to bottom: A bird's eye view of n_i, E_{x1}, B_{z1}, J_{x1}, and J_{y1} on field lines with 425 km apex altitude after an electrostatic state is met (t $>$ 15 seconds). For J_{x1} and J_{y1}, arrows are overlayed, indicating the current circulation. Slices a through f correspond to the slice key in Figure 7.1.

The divergence of gravity-driven currents from the density depletion is a source of anti-zonal currents that drive current circulation, as seen in the bottom two rows of Figure 8.1. Most current circulation happens between the source (at the bubble) and where zonal conductivity is the greatest: the E region. These currents, directed to the E region, can also be seen in the power plot in Figure 7.1, where most of the power (about 30 watts) is directed poleward into the E region whereas a small amount (a few watts) of power is directed equatorward. Not only is the Pedersen conduc-

tivity high in the E region, but Hall physics also increases the zonal conductivity with Cowling conductivity. In the electrostatic point of view, the highest zonal conductivity is naturally where the current divergence (from the bubble) will circulate through to satisfy Kirchhoff's current law. In the electromagnetic point of view, bubbles from both hemispheres are continuously generating Alfvén waves that emit poleward and equatorward. The meridional magnetic fields, B_{1z}, of these waves destructively interfere between the bubbles and constructively interfere on the poleward sides of each bubble. By Ampere's law, the destructive and constructive interference of B_{1z} corresponds to minimal J_{1y} and strong J_{1y}, respectively.

Note how well the electric fields map along magnetic field lines in Figure 8.1 as well as the steady state of Figure 7.2. It is approximately a constant order of magnitude along Earth's magnetic field lines, which act like equipotential wires due to the high conductivity along field lines. However, it is apparent that the field lines are not exactly equipotential, especially in the E region where the perpendicular conductivity is the highest and the parallel conductivity is decreased.

8.2 Electrostatic Rayleigh-Taylor current circulation: asymmetry about the equator

We direct our attention to the electrostatic state of the gravitational Rayleigh-Taylor modes in Section 7.2, where we allow for asymmetry about the equator. There is significant transequator current flow as shown in Figures 8.2a (for the bubble in the southern hemisphere) and 8.2b (for the bubble in the northern hemisphere). The panels from top to bottom present a bird's eye view of of the electrostatic n_i, E_{x1}, B_{z1}, J_{x1}, and J_{y1}, respectively, on field lines with 425 km apex altitude, corresponding to the z coordinate that passes through the center of the respective bubble. Slices $-f$ through f correspond to the slice keys in Figure 7.3.

For Figure 8.2a, the divergence of gravity-driven currents is seen as the anti-zonal currents

(blue) that is greatest at the center of the bubble (between slices $-d$ and $-c$). This divergence of current flows away from the bubble on the western magnetic field lines and towards the bubble on the eastern field lines as seen in the fifth panel. Turning our attention to the fourth panel, in the southern hemisphere, part of the anti-zonal current divergence is closed off at slice $-f$ by the zonal currents (yellow). In the northern hemisphere, part of the anti-zonal current divergence is closed near slice e by zonal currents that are slightly weaker than the zonal currents at slice $-f$. Nonetheless, it can be seen that significant currents flow along the full length of the magnetic field lines to close off the anti-zonal current divergence. The majority of the anti-zonal current divergence is closed off in the E region in both hemispheres because the transverse conductivity is the highest there.

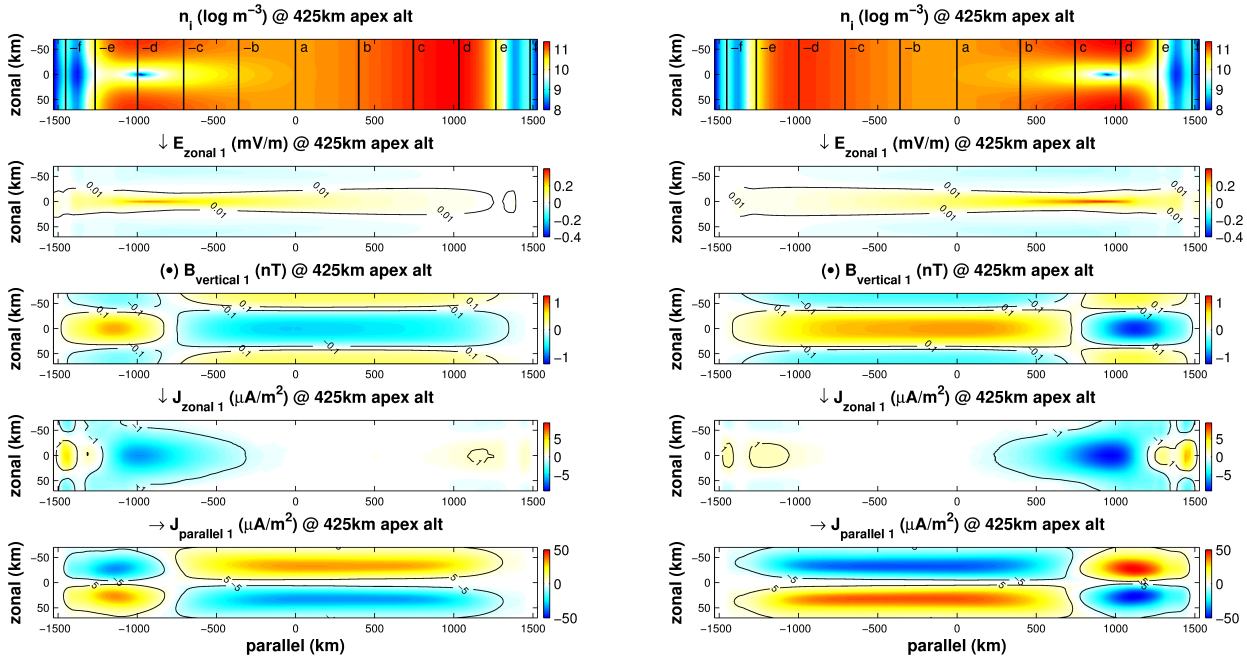

(a) The electrostatic Rayleigh Taylor currents with a bubble in the southern hemisphere. Slices $-f$ through f correspond to the slice key in Figure 7.3a.

(b) The electrostatic Rayleigh Taylor currents with a bubble in the northern hemisphere. Slices $-f$ through f correspond to the slice key in Figure 7.3b.

Figure 8.2: From top to bottom: A bird's eye view of n_i, E_{x1}, B_{z1}, J_{x1}, and J_{y1} on field lines with 425 km apex altitude after an electrostatic state is met (t $>$ 30 seconds).

For Figure 8.2b, the divergence of gravity-driven currents is seen as the anti-zonal currents (blue) that is greatest at the center of the bubble (between slices c and d). This divergence of current flows away from the bubble on the western magnetic field lines and towards the bubble on the eastern field lines as seen in the fifth panel. Turning our attention to the fourth panel, in the northern hemisphere, part of the anti-zonal current divergence is closed off at slice f by the zonal currents (yellow/orange). In the southern hemisphere, part of the anti-zonal current divergence is closed off at both slices $-f$ and $-e$ by zonal currents (yellow) that are slightly weaker than the zonal currents at slice f. Nonetheless, it can be seen that significant currents flow along the full length of the magnetic field lines to close off the anti-zonal current divergence. The majority of the anti-

zonal current divergence is closed off in the E region in both hemispheres because the transverse conductivity is the highest there.

When *Stolle et al.* (2006) investigated magnetic signatures of equatorial plasma irregularities, they observed inferred Poynting fluxes coming from both the north and south of the points of measurements. They attempted to interpret the flux directions as power transmitting away or towards a ion density bubble at the magnetic equator as modeled by *Bhattacharyya and Burke* (2000). It was thought that ion density bubble should generate Poynting power away from itself and away from the equator. However, they could not explain observations of Poynting flux pointing towards the equator and seemingly towards the generator. *Burke et al.* (2012) suggested the inconsistency comes from the assumption that plasma bubbles only reside at the equator and that plasma bubbles off the equator must be considered. As mentioned, that off-equator plasma bubbles can transmit Poynting power to the equator can certainly be the case as simulated and shown in Figures 8.2a and 8.2b. In both simulations, the off-equator bubble emits Poynting flux away from itself. For the simulation in Figure 8.2a, the bubble in the southern hemisphere emits northward power flux on its northern side as indicated by the positive E_{x1} and negative B_{z1}, corresponding to power transmitted towards the equator from the bubble. In Figure 8.2b, the bubble in the northern hemisphere emits southward power flux on its southern side as indicated by the positive E_{x1} and positive B_{z1}, corresponding to power also transmitted towards the equator from the bubble.

8.3 Diamagnetic current circulation

In this section, we present the electrostatic state of a simulation with the same initial conditions as in Sections 7.1 and 8.1. However, we turn on perpendicular pressure forces and turn off gravity. Under this condition, diamagnetic currents form. The electrostatic result is shown in Figure 8.3. The top two subplots present n_i and B_{y1} for field lines at 425 km apex altitude. The left and right columns present n_i and B_{y1} at perpendicular slice d. E_{1x}, E_{1y}, E_{1z}, B_{1x}, and B_{1z} are insignificant.

Diamagnetic currents are overlayed on n_i, showing the current flow along the bubble's walls in the plane perpendicular to Earth's magnetic field. By Ampere's law, this results in an enhanced B_{1y} within the center of the bubble. The blue line traces a simulated satellite pass. The bottom left and right plots show what the ion density and magnetic field measurements would look like along this pass. Accompanying the dip in n_i is an enhanced B_{y1} of about 0.2 nT. In other words, there is anti-correlation between n_{i1} and B_{y1}, where n_{i1} is the perturbation in ion density.

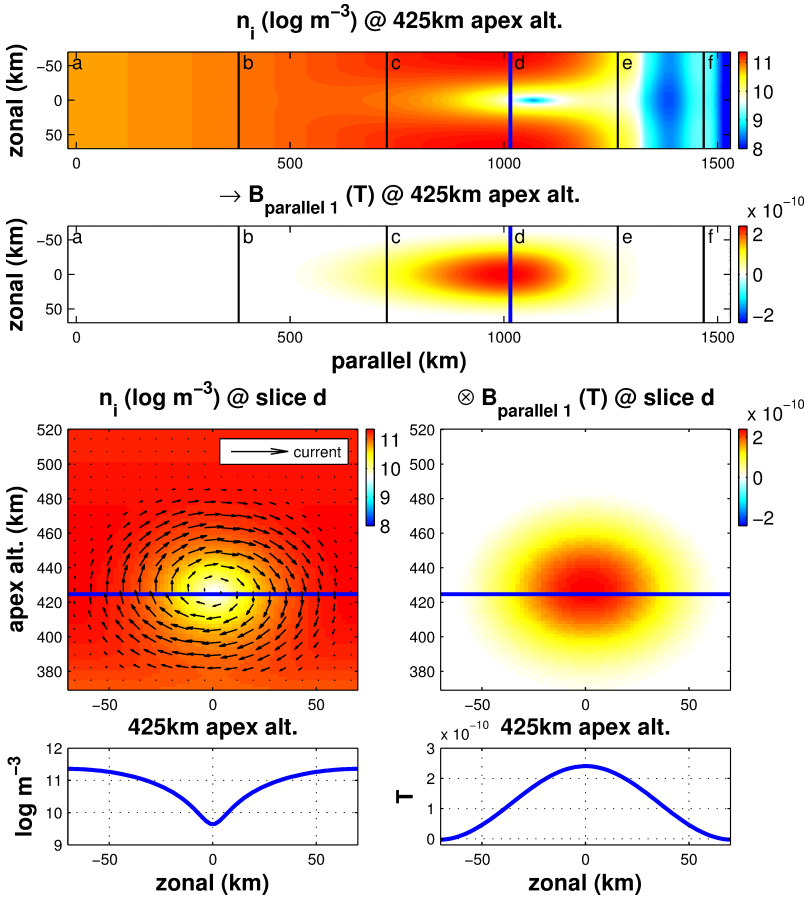

Figure 8.3: Electrostatic diamagnetic currents. The top two subplots plot n_i and B_{y1} for field lines at 425 km apex altitude. The left and right columns present n_i and B_{y1} at perpendicular slice d. Diamagnetic currents are overlayed on n_i, showing the current flow along the bubble's walls. Slices a through f correspond to the slice key in Figure 7.1.

The 0.2 nT B_{y1} enhancement inside the density bubble due to diamagnetic currents is completely consistent with the first-order approximation derived by *Lühr et al.* (2003), that the parallel perturbation magnetic field can be calculated as

$$B_{y1} = -n_{i1} k_b \left(T_i + T_e\right) \frac{\mu_0}{B_0}, \tag{8.1}$$

where k_b is the Boltzmann constant. For the simulated conditions where $n_{i1} \approx 2 \times 10^{11} m^{-3}$ and $T_i + T_e \approx 2000k$, equation (8.1) also results in 0.2 nT. EMI simulations verify Lühr's approximation as well as the conclusion made by *Stolle et al.* (2006) attributing CHAMP-observed B_{y1} to diamagnetic currents around equatorial bubbles. The CHAMP satellite observations in Figure 1.3 exhibits similar anti-correlation between n_{i1} and B_{y1} as in Figure 8.3. As first suggested by *Stolle et al.* (2006), measuring B_{y1} is a viable method for detecting equatorial density bubbles (as long as the magnetometer has at least ~ 0.1 nT precision).

8.4 Ambipolar current circulation

In this section, we present the electrostatic state of a simulation with the same initial conditions as in Sections 7.1, 8.1, and 8.3. However, we turn on parallel pressure forces and turn off both perpendicular pressure forces and gravity. Under this condition, ambipolar electric fields form. The associated current flow resulting from the density perturbation is simulated and shown in Figure 8.4. Note that only features resulting from the ion density perturbation are presented and that the effects of background ambipolar fields are not included. The maximum electric field is on the order order of 10^{-5} V/m. The maximum magnetic field is on the order of 10^{-3} nT.

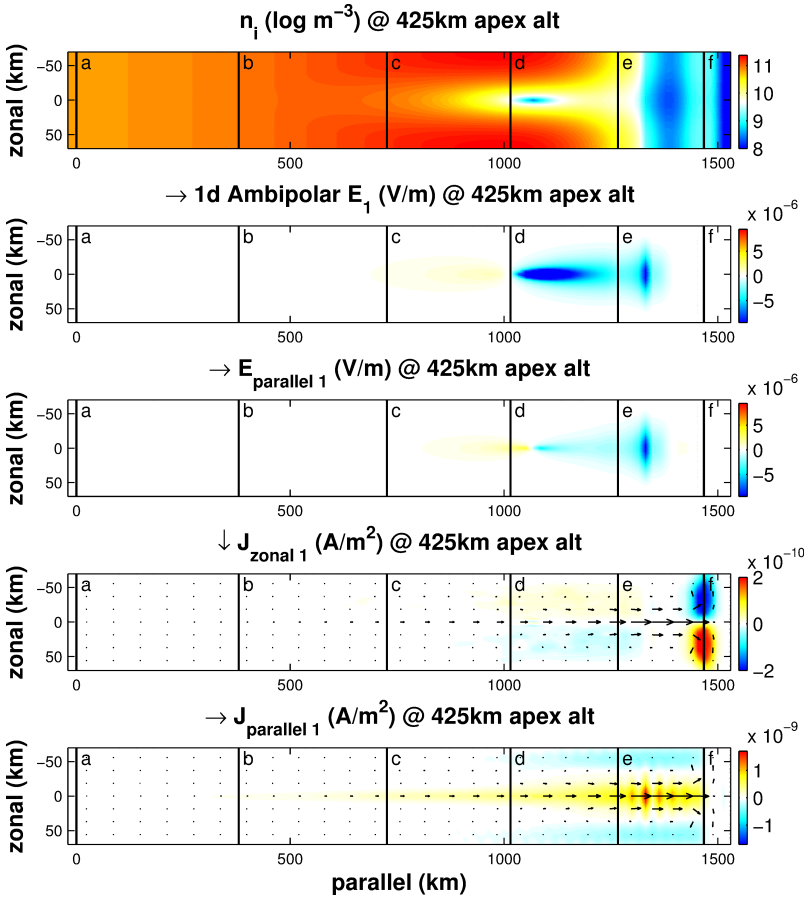

Figure 8.4: Electrostatic ambipolar currents. From top to bottom: A bird's eye view of n_i, theoretical 1-D ambipolar E_{y1}, simulated 3-D E_{y1}, J_{x1}, and J_{y1} on field lines at 425 km apex altitude. Note that the color scale of the 1-D ambipolar E_{y1} is clipped at 0.01 mV/m where the maximum between slices d and e is actually 0.2 mV/m between slices d and e. For J_{x1} and J_{y1}, arrows are overlayed, indicating the current circulation. Slices a through f correspond to the slice key in Figure 7.1. The simulated E_{y1} is less than 1-D theory predicts.

Each panel plots parameters at 425 km apex altitude. Plotted from top to bottom are n_i, theoretical one-dimensional (1-D) ambipolar E_{y1}, simulated 3-D E_{y1}, J_{x1}, and J_{y1}. Note that for the theoretical 1-D ambipolar E_{y1} in Figure 8.4, the color scale is clipped at 0.01 mV/m where the maximum between slices d and e is actually 0.2 mV/m, differing from the 3-D results by an order

of magnitude. The theoretical 1-D ambipolar electric field is computed as

$$E_{y1} = -\nabla_{\parallel} p_e / e n_e, \tag{8.2}$$

as derived in Section 2.7 by solving for the electric field after setting the ion velocity equal to the electron velocity to maintain quasi-neutrality in 1-D. The limitation to this 1-D ambipolar electric field is that larger electric fields build up because the electrons are only free to move in one dimension. In 3-D, electrons can flow in current loops to maintain quasi-neutrality and do not require such large ambipolar electric fields to maintain quasi-neutrality. Hence, 3-D ambipolar electric fields will be less than 1-D ambipolar electric fields, as seen by comparing the two in the second and third panels of Figure 8.4.

Note that the current flow and associated electric fields are dominated by the density gradient on the poleward side of the bubble because there is less electron density where electron pressure forces play the biggest role, as seen in equation (3.8). The electrons diffuse equatorward faster than the ions driving poleward currents. Via perpendicular conductivity, this current draws electrons from the outside of the bubble where the current flows equatorward. The faint blue and yellow zonal currents near slice d in the 4th panel show the drawing of current from outside the bubble to the inside of the bubble. The dark blue and dark red zonal currents at slice f show where current flows out of the bubble, completing the current loop. The current circulation flows poleward within the bubble, driving a toroidal current flow that circulates current from outside the bubble.

One of the implications of this simulation is that care must be taken in interpreting ambipolar electric fields observed experimentally. Although it is relatively easy to calculate in 1-D, the ambipolar electric field is lower with three degrees of freedom than with only one degree of freedom. In the simulation presented in Figure 8.4, they differed by 20 times. To estimate the parallel density gradient from E_{y1}, one cannot rely on 1-D theory, despite its simplicity. In solving the 1-D ambipolar electric field equation (8.2) for the parallel density gradient, we could erroneously calculate the

density gradient as $\nabla_{\parallel} n_e = -E_{y1}/en_e k_b T_e$. However, since 1-D theory overestimates 3-D ambipolar electric fields, 1-D theory only gives an upper bound ($\left|\nabla_{\parallel} n_e\right| \leq |E_{y1}/en_e k_b T_e|$), which is not very useful, considering that the gradient can be 20 times less than the upper bound.

In the context of simulating ionospheric physics, a consequence of 1-D overestimation of ambipolar electric fields is that there will be greater ambipolar diffusion and subsequently different plasma morphology. However, keep in mind that the discrepancy between 1-D and 3-D ambipolar electric fields likely decreases with increasing perpendicular scale lengths. Increasing scale lengths in any two dimensions eventually approaches a 1-D limit. What scale lengths 1-D ambipolar electric fields are valid is worth investigating in the future.

8.5 The invalidity of equipotential field lines

Due to simplicity, spread F theory has often assumed equipotential field lines due to the high parallel conductivity parallel to **B** (*Haerendel*, 1973; *Perkins*, 1973; *Sultan*, 1996; *Dao et al.*, 2012). We stress that field lines being equipotential is only an approximation. Electric fields do not map perfectly and finite parallel conductivity can be significant.

Asymmetry about the equator as simulated in Section 8.2 best illustrates the shortfalls of the equipotential approximation of Earth's magnetic field lines. By the electric field mapping equation for equipotential magnetic dipole field lines (B.1),

$$E_x = \frac{1}{\cos^3\theta} \cdot E_x|_{\theta=0}, \tag{8.3}$$

$$E_z = \frac{\sqrt{1+3\sin^2\theta}}{\cos^3\theta} \cdot E_z|_{\theta=0}, \tag{8.4}$$

which implies two properties. Firstly, the electric field is mirrored about the equator. Secondly, for low latitudes ($\theta \sim 0$), $\mathbf{E}_{\perp}$ is approximately equal along the whole field line. However, it can

be seen in Figures 7.4a and 7.4b, that the field lines are far from equipotential; the electric field is neither symmetric nor does it remain roughly equal along the whole field line. For the simulation in Figure 7.4a, there is an order of magnitude difference between the maximum zonal electric field in the northern hemisphere (0.28 mV/m) and the zonal electric field at the complimentary point in the southern hemisphere (0.02 mV/m). For the simulation in Figure 7.4b, there is an order of magnitude difference between the maximum zonal electric field in the northern hemisphere (0.36 mV/m) and the zonal electric field at the complimentary point in the southern hemisphere (0.03 mV/m). In Figure 8.5, we plot the electrostatic electric field from Figure 7.4a with a solid line and superimposed the polarization electric field derived assuming equipotential field lines (expressed by equation 2.44) with a dashed line. With the dashed-dotted line, we also plot the equipotential polarization fields using the Cowling conductivity, σ_c, instead of the Pedersen conductivity, σ_p. Neither equipotential polarization fields match the more realistic polarization field. Figure 8.5 illustrates the difference when assuming equipotential-field-lines when deriving the polarization electric fields. The equipotential-field-lines approximation at best yields zeroth-order accurate polarization fields.

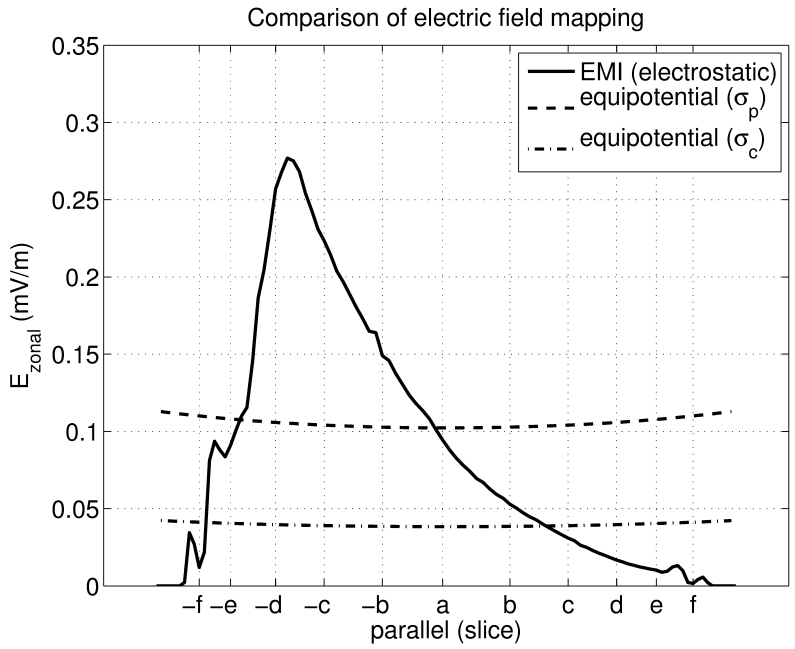

Figure 8.5: Electric field mapping.

There are several implications of the imperfect mapping of electric fields along Earth's magnetic field lines. Firstly, the $\mathbf{E} \times \mathbf{B}_0$ drift speed is not approximately uniform along the field line and remains localized to the bubble (to a certain extent). Truly equipotential field lines would impose approximately equal $\mathbf{E} \times \mathbf{B}_0$ drift speeds in both hemispheres. Given a roughly symmetric background ionosphere, only bubble pairs can grow symmetrically about the equator under the equipotential approximation since the integral of the continuity equation (2.28) would also be symmetric about the equator. When the electric field remains partially localized in one hemisphere due to imperfect mapping, the Rayleigh-Taylor mode also remains partially localized and allows for a single bubble to appear in one hemisphere without a paired bubble mirrored in the complimentary hemisphere. In fact, despite the carrying of information throughout the whole system via Alfvén waves, we can speculate that it is very unlikely for symmetric bubble pairs to form considering both the imperfection of electric field mapping and the asymmetry of the background ionosphere.

8.6 The effects of neutral winds on the Rayleigh-Taylor mode

In Section 2.3, the effects of wind on the Rayleigh-Taylor mode are discussed. In this section, we present two simulations with the same setup as Figure 7.3a with a plasma depletion in the southern hemisphere. One simulation simulates only gravitational currents and zero neutral winds. The other simulation simulates gravitational currents with 100 m/s zonal neutral winds across the bubble. However, one cannot just consider zonal neutral winds and neglect the background electric field. The meridional currents (that zonal winds produce) develop a background anti-meridional electric field reducing the meridional current (*Rishbeth*, 1971). By *Rishbeth* (1971), the zonal drift resulting from the anti-zonal polarization field is approximately 0.8 times the velocity of the neutral wind at night. Hence, the effects of neutral winds is effectively reduced by 80%. To model 100 m/s zonal wind we reduce its efficiency by 80 % to include the approximate effects of a polarization electric field resulting from zonal winds. The electric field signatures with no winds are presented in Figure 8.6a. The electric field signatures with winds are presented in Figure 8.6b. In the F region (slices $-e$ to e), it can be seen in Figure 8.6a that the gravitational Rayleigh Taylor mode purely develops zonal electric fields. With the addition of a zonal wind simulated and presented in Figure 8.6b, meridional polarization fields develop in addition to the gravitational polarization fields, resulting in tilted $\mathbf{E}_{\perp 1}$.

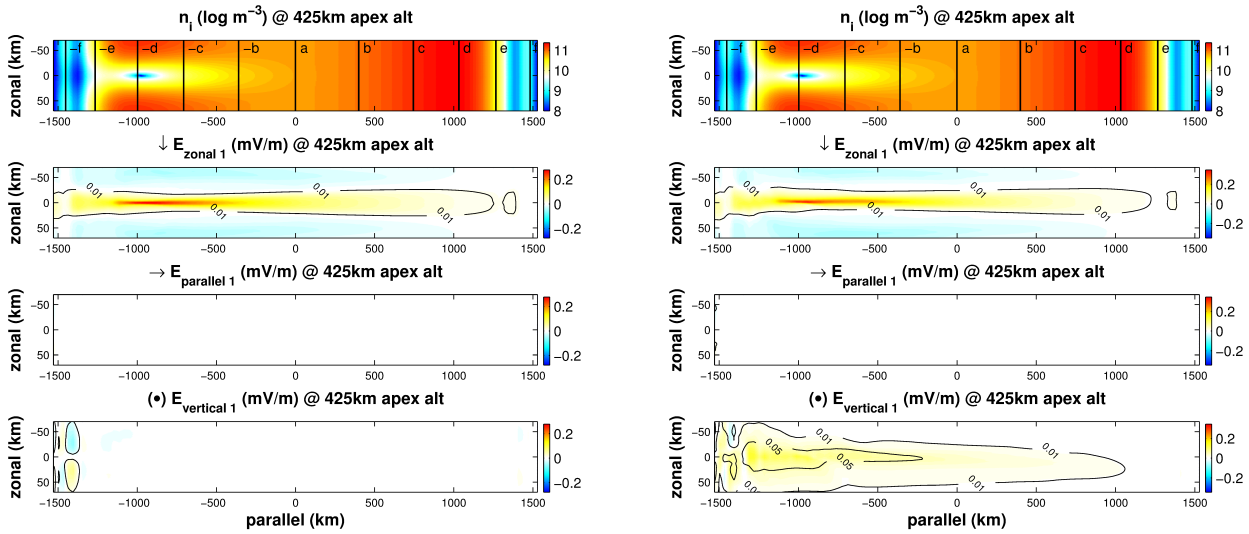

(a) Without wind

(b) With wind

Figure 8.6: Electric field signatures of Rayleigh-Taylor mode without and with zonal winds across the bubble

In Figure 8.7a, presented are developed magnetic field signatures of the purely gravitational Rayleigh Taylor mode. It can be seen that there are strong meridional magnetic field signatures, but insignificant zonal magnetic field (except in the E region where the parallel currents close off). When zonal winds are included as presented in Figure 8.7b, zonal magnetic fields develop, resulting in tilted $\mathbf{B}_{\perp 1}$ consistent with those observed in nature.

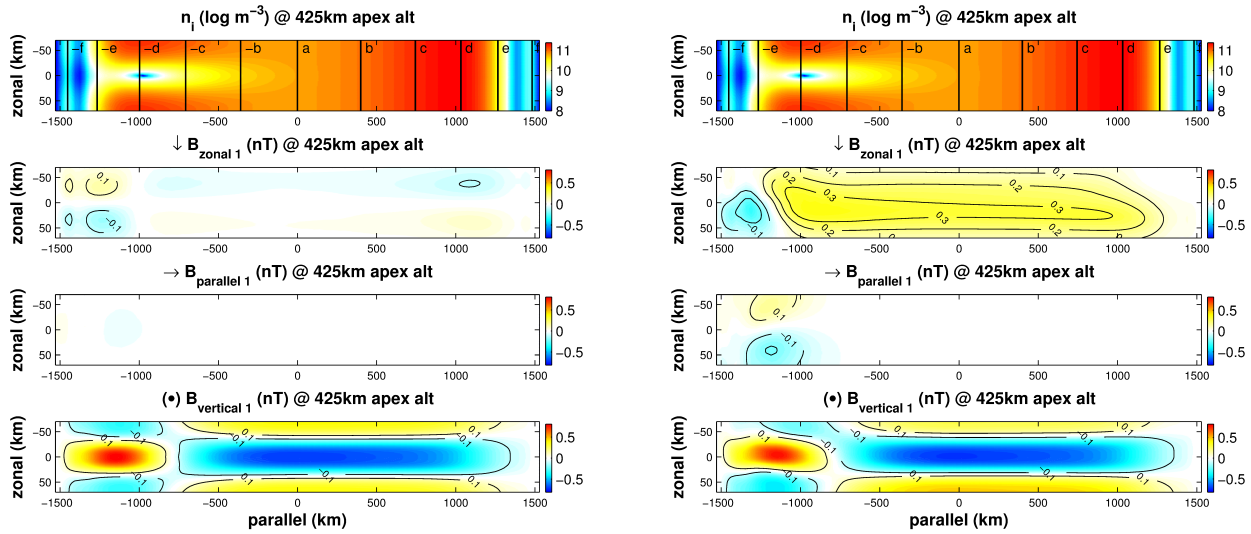

(a) Without wind

(b) With wind

Figure 8.7: Magnetic field signatures of Rayleigh-Taylor mode with and without zonal winds across the bubble.

These simulations may explain the major discrepancies between the gravitational Rayleigh-Taylor mode (presented in Subsections 7.1, 8.1, 7.2, and 8.2) and observed electric field measurements such as the ones shown Figure 1.2. The perpendicular electric fields are observed as tilted (has both zonal and meridional fields), whereas the gravitational Rayleigh-Taylor mode primarily produces just zonal electric fields. When browsing through the whole database of C/NOFS VEFI measurements, perturbation electric fields are often tilted and are rarely purely zonal. In Figure 8.8, from the first to third panel, we plot normalized density fluctuations (n_{i1}/n_{i0}) as measured by CNOFS' PLP, zonal electric field perturbations (E_{x1}) as measured by CNOFS' VEFI, and meridional electric field perturbations (E_{z1}) as measured by CNOFS' VEFI during June 1, 2008. It can be seen that electric field fluctuations correspond to plasma irregularities, but are not purely zonal. In the fourth panel, for $|\mathbf{E}_\perp| > .5$ mV/m, we plot the probability distribution function of $\tan^{-1}(E_{z1}/E_{x1})$, the tilt angle between $\mathbf{E}_{\perp 1}$ and the zonal direction. It can be seen most of $\mathbf{E}_{\perp 1}$

has a positive tilt angle corresponding to upward and westward drifts, which *McClure et al.* (1977) also observed using the Atmosphere Explorer satellite AE-C. There are also similar discrepancies between the gravitational Rayleigh-Taylor mode's magnetic fields and observed magnetic fields such as the CHAMP observations presented in Figure 1.3. The perpendicular magnetic field is observed as tilted, whereas the gravitational Rayleigh-Taylor mode only produces meridional magnetic fields (for example Figure 8.7a), except in the E region where meridional Hall currents flow. With the gravitational Rayleigh-Taylor modes, plasma depletions only result in anti-zonal current divergence, resulting in zonal polarization electric fields and meridional magnetic fields. The observed tilted electric and magnetic fields suggest that they must have not been purely driven by gravitational currents. Keep in mind that the tilted fields cannot be rectified by diamagnetic currents or ambipolar currents, either. Diamagnetic currents are non-divergent and don't produce polarization electric fields as discussed in Section 2.6. The electric fields resulting from ambipolar currents are far less than the mV/m magnitudes observed and do not run across the bubble in the perpendicular plane.

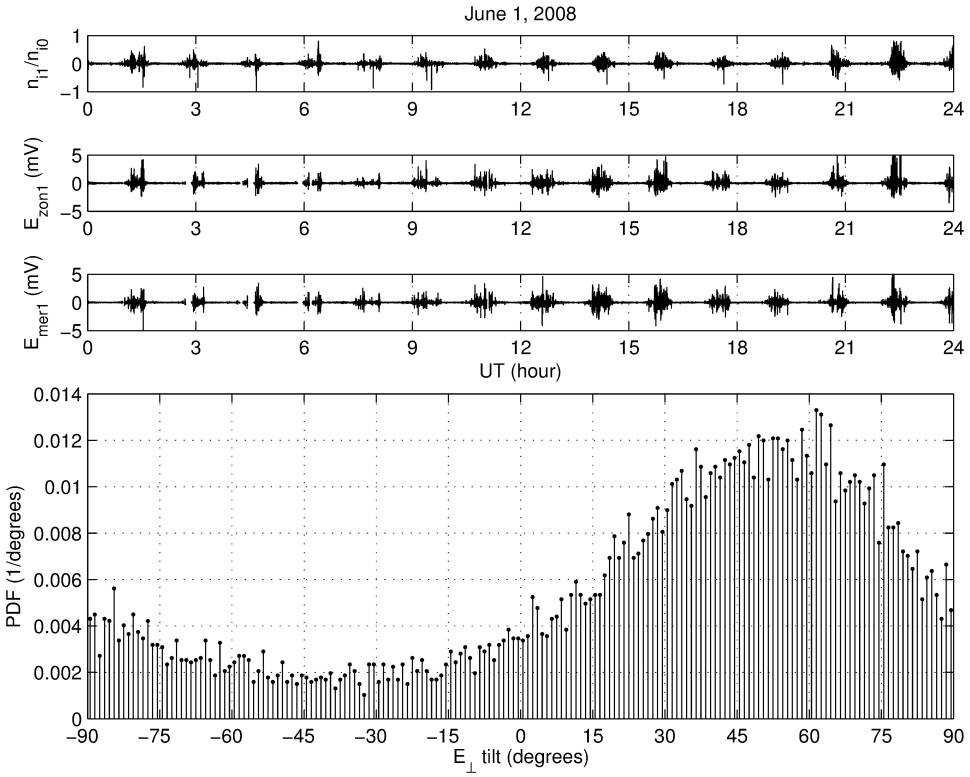

Figure 8.8: The first three panels starting from the top: ion density, zonal electric field, and meridional electric field fluctuations. The fourth panel plots the probability distribution function of the angle between the perpendicular electric field and the zonal direction.

Chapter 9

Alfvén wave resonator

The simulations presented in Chapter 7 show that the generalized Rayleigh-Taylor mode can take tens of seconds to reach an approximately electrostatic state. These electrodynamic time scales will, of course, vary with the ion mass density as well as the length of the magnetic field line on which the ion density bubble resides. Regardless, the electrodynamic time scales are virtually instantaneous compared to the Raleigh-Taylor growth rates, which are typically tens of minutes. However, plasma bubbles often move with background drifts while Earth's magnetic field lines remain fixed. In the tens of seconds it takes Alfvén waves to map electric fields along a set of magnetic field lines, a bubble may move significantly. Alfvénic time delays may introduce positive and negative interference and may play an important role in mode selection.

Previously, Alfvén resonance has been analyzed for high-latitudes (e.g. *Atkinson*, 1970; *Trakhtengertz and Feldstein*, 1984; *Lysak*, 1986, 1991; *Cosgrove and Doe*, 2010). In this chapter we explore Alfvén wave resonance in the context of low-latitude plasma irregularities. We present two simplified scenarios illustrating the idea of Alfvén resonance in the context of low-latitude plasma irregularities. In the first scenario, we show how zonally stationary waves encounter negative interference from negatively reflecting Alfvén waves. In the second scenario, we show that when drifting zonally

at the right speed, positive interference and Alfvén wave resonance may occur. After illustrating the concept of Alfvén resonance, several simulation results will be presented, showing the Alfvén resonance phenomenon.

Consider a density perturbation wave along the magnetic equator, as illustrated in Figure 9.1. In the first frame on the left, negative density perturbations (which we will denote as $-\Delta n_i$) emit positive zonal electric fields (which we will denote as $+E$) parallel to Earth's magnetic field line. On the other hand, positive density perturbations ($+\Delta n_i$) emit negative zonal electric fields ($-E$). As time progresses, these transmitted $+E$ and $-E$ reach the E region via Alfvén waves. The transverse conductive load is much larger in the E region, thus it negatively reflects the Alfvén waves back towards the bubbles (see Section 6.2), as illustrated in the middle frame. These negative reflections transmit back from the bubble they originated. For zonally stationary bubbles, these negative reflections negatively interfere with the bubbles. Negative perturbation bubbles,$-\Delta n_i$, receive a negative zonal electric field, $-E$. Positive perturbation bubbles, $+\Delta n_i$, receive positive zonal electric field, $+E$. These received negative reflections hinder Rayleigh-Taylor growth rate.

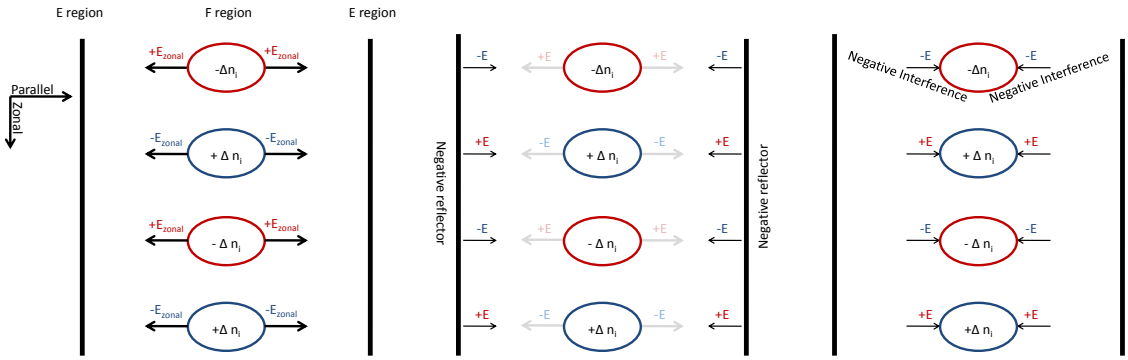

Figure 9.1: A diagram illustrating stationary density waves transmitting electric fields towards the E region and receiving negative reflections that negatively interfere.

Now consider a zonal drift that moves the density wave half a wave length in the time takes for transmitted electric fields to reflect back, as illustrated in Figure 9.2. Like in the first scenario, in the

first frame on the left, $-\Delta n_i$ emit $+E$ parallel to Earth's magnetic field line while $+\Delta n_i$ emit $-E$. As time progresses, these $+E$ and $-E$ reach the E region via Alfvén waves negatively reflect back towards the bubbles, as illustrated in the middle frame. However, the bubbles are drifting unlike in the first scenario. These negative reflections transmit back from where they originated, but at a half wave length away from the bubble the originated from. Negative deviation bubbles,$-\Delta n_i$, receive a positive zonal electric field, $+E$. Positive bubbles, $+\Delta n_i$, receives negative zonal electric field, $-E$, as illustrated in the third frame. These received reflections increase Rayleigh-Taylor growth rate.

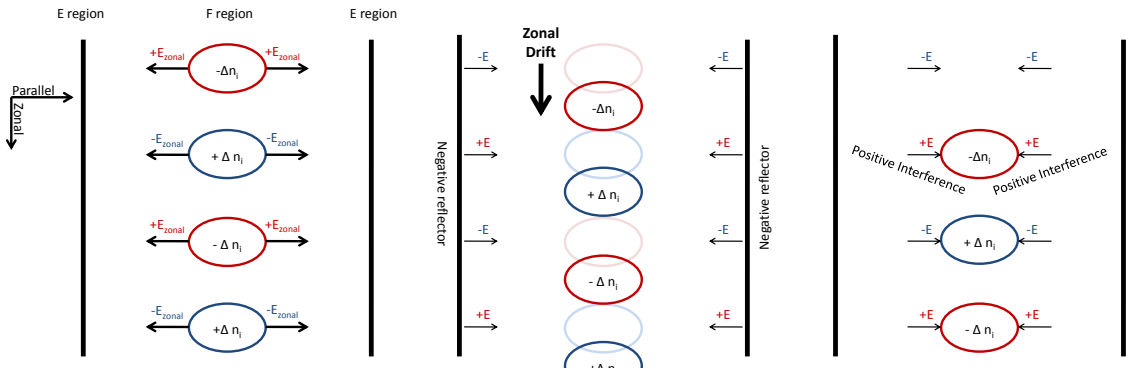

Figure 9.2: A diagram illustrating that drifting density waves transmitting electric fields towards the E region and receiving negative reflections can positively interfere if the bubble drifts at a certain speed.

In order to investigate this Alfvén resonance, we numerically simulate the electromagnetic fields for a periodic two-dimensional density wave as shown in figure 9.3 on the right. The plasma density wave has a 100 km zonal wavelength. On the left is the background ion density for the simulation. For several constant zonal drift speeds, the electromagnetic dynamics are simulated until an equilibrium is met after approximately ten virtual seconds. The total magnitude of perturbation zonal electric fields in the system is recorded for each constant zonal speed and plotted in Figure 9.4, illustrating that at the right drift speed, certain wavelengths will resonate. On the x-axis is the ratio of the density zonal wavelength to the zonal drift speed. The right shows the response for

slower drifts. On the y-axis is the total magnitude of perturbed zonal electric fields normalized by the total for a stationary bubble. There is a speed that yields a maximum zonal electric magnitude when the ratio of the wavelength to drift speed is about 10 seconds, which is also the timescale at which electromagnetic waves travel along magnetic field lines in this case. To the right of the resonance, zonal electric fields decrease and reach a limit where waves are effectively stationary. This diminished zonal electric field is due to the negative interference illustrated in Figure 9.1.

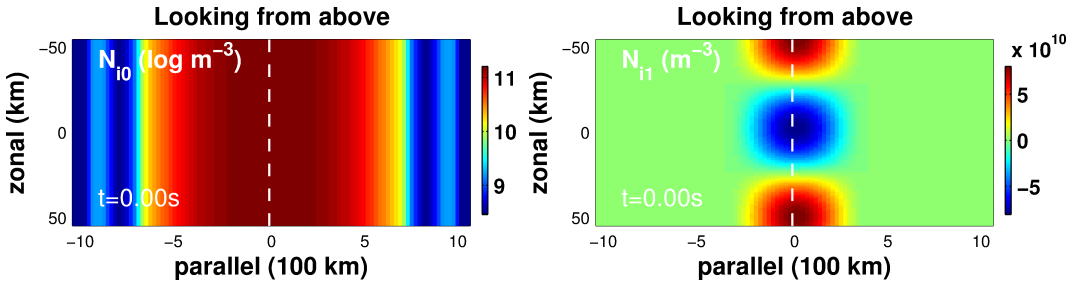

Figure 9.3: On the left, the background ionosphere (log m^{-3}). On the right, the density perturbation (m^{-3}) with zonal periodicity and a wavelength of 100 km. During the simulations, the perturbation drifts zonally at a constant speed.

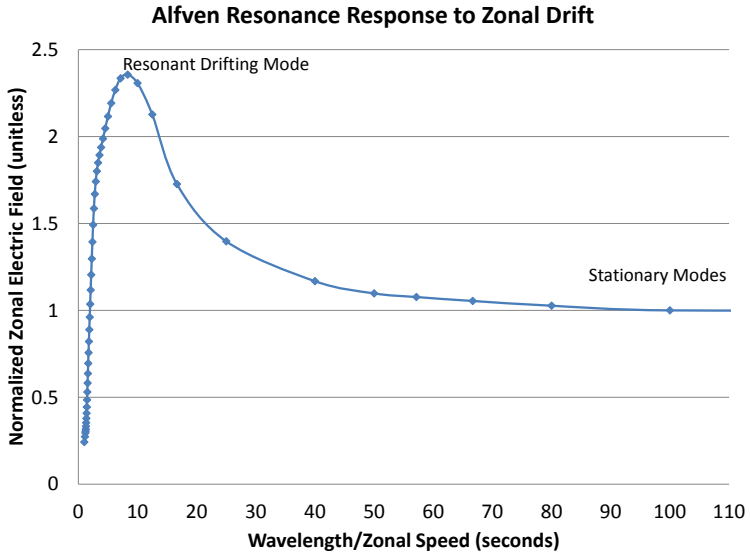

Figure 9.4: Zonal electric field response to zonal drifts.

Note that although Alfvén resonance is an interesting problem, it is probably very rare in nature. In this case, for a zonal wavelength of 100 km, the zonal drift speeds associated with resonance is 10^4 m/s, an extremely fast drift speed. Typically, maximum drift speeds are on the order of 100 m/s. Given 100 m/s zonal drifts, resonance would occur for a 1 km wavelength wave. However, these shorter wavelength waves do not map along Earth's magnetic field lines as efficiently as longer wave lengths (*Farley*, 1960). Hence, we do no expect Alfvén resonance to play a major role for typical low-latitude plasma irregularities. However, a more thorough investigation of Alfvén resonance for different wavelengths could be worth pursuing in future studies.

Chapter 10

Supersonic bubble

Inspired by *Aggson et al.* (1992), this chapter will explore the electrodynamics of a supersonic bubble. It has already been established, in Chapter 7, that Alfvénic timescales are on the order of 10s of seconds. A bubble rising at supersonic speeds of kilometers per second would rise tens of kilometers within Alfvénic timescales. Hence, a significant portion of a supersonic bubble is inherently electrodynamic, making supersonic bubbles a class of bubbles that only a dynamic electromagnetic model can accurately model.

In order to impose supersonic vertical drift speeds on the order of 1 km/s (faster than the speed of sound), we set the effective gravity (that drives the Rayleigh-Taylor mode) to 100 times greater than that of Earth. In nature, this effective gravity can be achieved in several ways (see Section 2.3). Whether the increase of effective gravity is caused by strong background drifts or neutral winds, we simply mimic the higher effective gravity by artificially increasing Earth's gravity by 100 times. For initial conditions, an initial perturbation is artificially placed in the system to seed a bubble, after which the bubble dynamics are simulated and the perturbation grows. The ion density, zonal electric field, and meridional magnetic at 0, 30, 60, and 90 seconds are plotted in Figures 10.1, 10.2, 10.3, and 10.4, respectively. For each figure, the first column shows the values of a 2-D cut through

the simulation space at 310 km apex altitude, where the x-axis is the parallel distance from the apex and the y-axis is the zonal distance from the center of the simulation space. The second column shows the values of a 2-D meridional-parallel cut through the simulation space, where the x-axis is the parallel distance from the apex and the y-axis is the apex altitude. The third column shows the values of a 2-D $\perp$ cut through the simulation space, where the x-axis is the zonal distance from the center of the simulation space and the y-axis is the apex altitude. The dashed-lines in each plot indicate where the 2-D cuts are taken.

The dynamics of the bubble growth is similar to that described in Section 2.2, except with the complexities of three dimensions, non-linear effects, and Alfvén dynamics. At $t = 0$, the system is initialized with a small density perturbation at 200 km apex altitude. After this point in time, zonal polarization electric field develops within the bubble to close off anti-zonal current divergence as seen at $t = 30$ s. The zonal electric polarization field imposes a vertical drift that advances the bubble to higher altitudes. At $t = 60$ s, the polarization electric field increases to an order of 10 mV/m and the bubble reaches even higher altitudes. At $t = 90$ s, the bubble pierces to the topside of the F layer. Note the morphology of the top of the bubble. Although the initial perturbation is an ellipsoid-like shape, the bubble evolves a "folded circular cap" reminiscent of bubble evolution in the inertial regime as simulated by *Zargham* (1988). In the strictly collisional regime (where inertia is negligible), the perturbation shape should not change as drastically (*Zargham*, 1988). In other words, without inertial effects, the initial ellipsoid bubble would have maintained its ellipsoid shape. The folded circular cap, signature to inertial effects, shows the importance of ion inertia to the dynamics of supersonic bubbles.

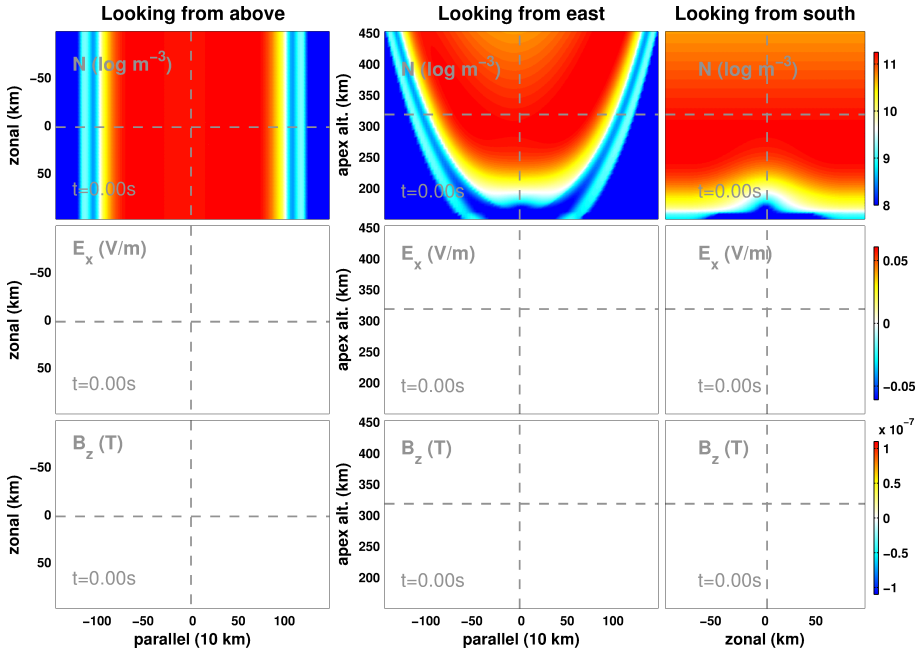

Figure 10.1: Ion density, E_{x1}, and B_{z1} of a growing supersonic bubble at $t = 0$ s.

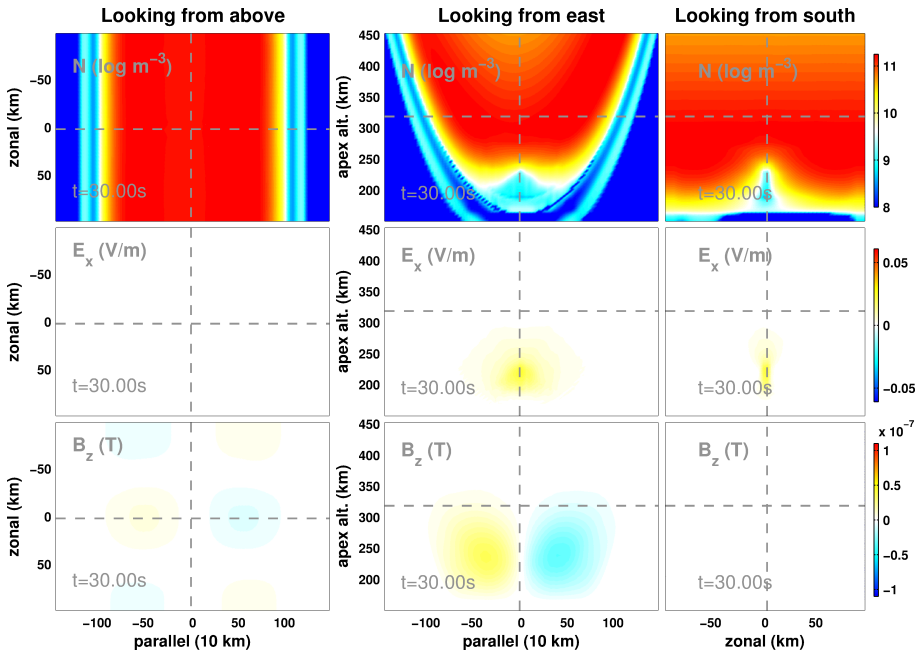

Figure 10.2: Ion density, E_{x1}, and B_{z1} of a growing supersonic bubble at $t = 30$ s.

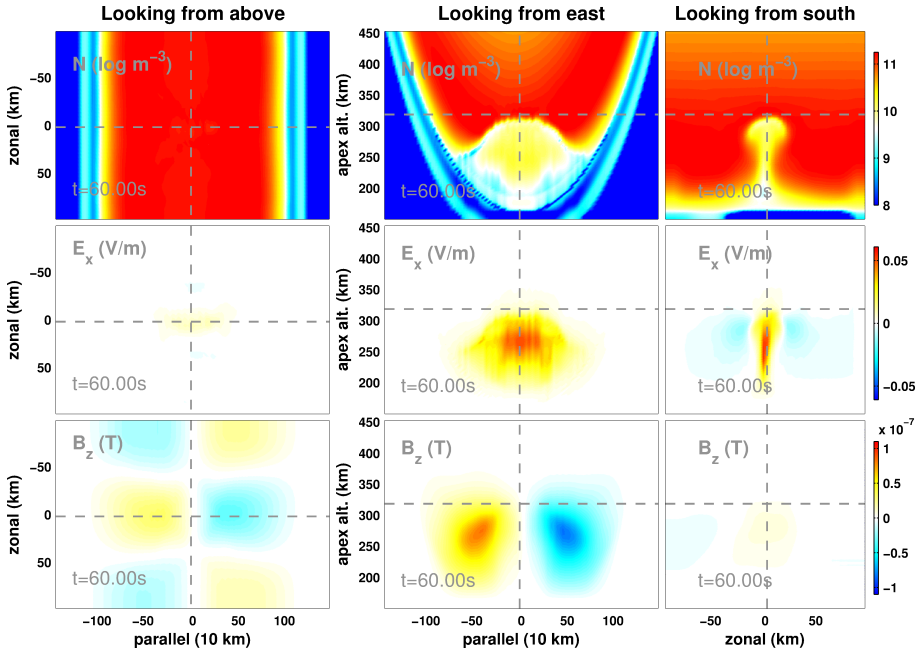

Figure 10.3: Ion density, E_{x1}, and B_{z1} of a growing supersonic bubble at $t = 60$ s.

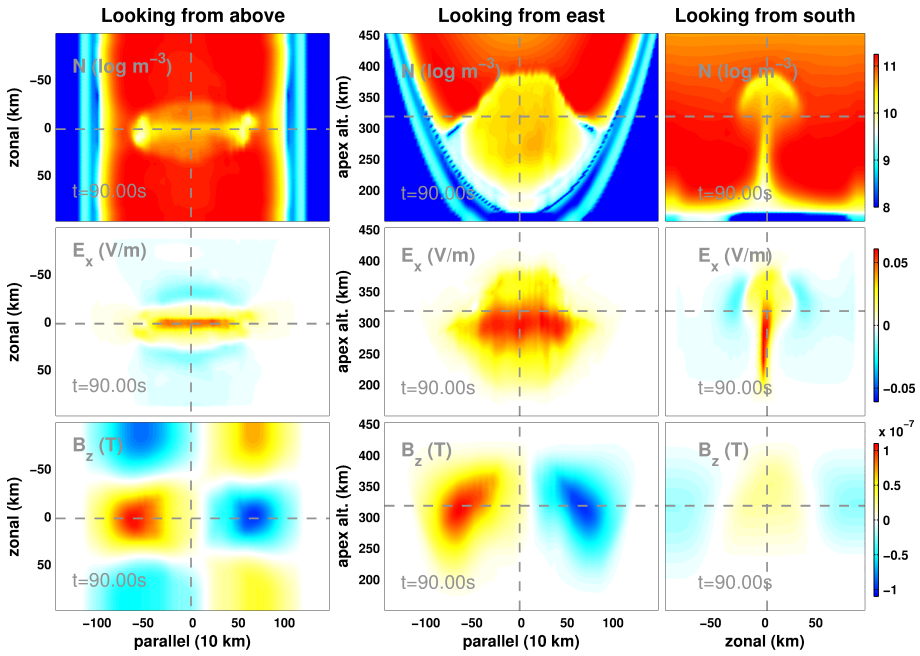

Figure 10.4: Ion density, E_{x1}, and B_{z1} of a growing supersonic bubble at $t = 90$ s.

As seen in Figure 10.4, the signatures of the supersonic bubble is a strong zonal electric field on the order of 10 mV/m, and strong negative and positive meridional magnetic fields on the northern and southern edge of the bubble, respectively, on the order of 100 nT. Both of these characteristics are similar to that observed by *Aggson et al.* (1992). Furthermore, the Poynting flux is consistent with *Aggson et al.*, where $\sim$ mW/m^2 of Poynting flux is directed polewards along Earth's magnetic field lines. The ratio between E_{x1} and B_{z1} at the northern and southern side of bubble is on the order of 10^5 m/s, consistent with the relation,

$$\frac{E_{x1}}{B_{z1}} = V_a \tag{10.1}$$

(*Aggson et al.*, 1992). Although the conditions used in this simulation are unlikely the exact same as those for the supersonic bubbles observed by *Aggson et al.* (1992), the supersonic bubble simulated in this chapter seems to support that *Aggson et al.* did observe a supersonic bubble considering the similarities in electromagnetic characteristics.

Chapter 11

Conclusions

In this dissertation, we developed a self-consistent model for the three-dimensional fluid treatment of ionospheric plasma, including the complete set of electromagnetic fields. The model is capable of time integration of electromagnetic field and plasma evolution with three spatial dimensions because of the efficient algorithm developed in Chapters 3 and 4. Unlike low-latitude ionospheric models that traditionally assume electrostatics, EMI includes electromagnetic dynamics. For the first time in the context of low-latitude ionospheric plasma irregularities, Alfvén waves that carry information throughout the system are modeled (see Chapter 7). Although bubble growth is typically much slower than the electrodynamics associated with bubbles, we explore scenarios that electrostatic physics cannot resolve. These scenarios include Alfvén resonance (see Chapter 9) and supersonic bubbles (see Chapter 10). Complimentary to modeling dynamic electromagnetism, static electromagnetism is also resolved after electrodynamics settle into a steady-state which is explored in Chapter 8. In this chapter we will summarize main results presented in this dissertation.

11.1 Alfvénic dynamics of Rayleigh-Taylor mode

In Chapter 7, the electrodynamics of several bubbles were simulated and analyzed. Polarization electric fields develop within the bubbles and transmit Alfvén waves away from the bubbles parallel and anti-parallel to **B** until an electrostatic state is met. The simulations show that the generalized Rayleigh-Taylor mode can take tens of seconds to reach an approximately electrostatic state. These electrodynamic time scales will, of course, vary with the ion mass density as well as the length of the magnetic field line on which the ion density bubble resides. The F-region ion density presented was modeled for an extremely low f10.7 index of 68.5 where the ion density is much lower than for normal or high solar flux conditions. These low densities result in faster Alfvén speeds and faster electrodynamic time scales. During solar maximum, ion densities may be as much as an order of magnitude greater, resulting in slower Alfvén speeds and slower electrodynamic time scales, by about a factor of three. Even in these conditions, the electrodynamic time scales are virtually instantaneous compared to the Raleigh-Taylor growth rates, which are typically tens of minutes. For phenomena much slower than the 10s of seconds it takes for Alfvén dynamics to reach equilibrium, the electrostatic approximation is valid. However, for scenarios where plasma irregularities can move significantly within the Alfvénic timescales, the electrostatic approximation will fail. Inclusion of electrodynamics is necessary to fully describe the physics of bubbles drifting faster than the bubble length scale of interest divided by the Alfvénic timescales. For example, electrodynamics are needed in the case of Alfvén resonance in Chapter 9 and for simulating a supersonic bubble in Chapter 10.

11.2 Poynting flux

Simulations in Chapter 7 and Section 8.2 demonstrate how one can use electric and sensitive magnetic field measurements to detect remote plasma irregularities that exist somewhere else on the intersecting magnetic field line. The electric field signature of a plasma depletion is zonal electric

field that is transmitted away from the bubble parallel and anti-parallel to $\mathbf{B}$. The magnetic signature of the gravitational Rayleigh-Taylor mode is a B_{z1} on the order of 0.1 nT. This is detectable by sensitive magnetometers on-board satellites. With the combined measurements of E_{x1} and B_{z1}, we can theoretically compute where the signatures are transmitted from. If, at the point of measurement, we measure zero B_{z1}, we can infer that there is equal depletion on both sides of the point or that the point of measurement is within the center of a bubble. Negative B_{z1} indicate signatures transmitted from the south. Positive B_{z1} indicate signatures transmitted from the north. This is useful in pinpointing where a plasma irregularity may be from a single measurement on a magnetic field line. Measuring $\mathbf{E}_1$ at the equator can identify that a plasma irregularity exists somewhere ambiguously along the intersecting magnetic field line. Additionally measuring $\mathbf{B}_1$ can hone in on the irregularity and determine on which side of the measurement point the irregularity exists.

11.3 Diamagnetic signature

In Section 8.3, we simulated electrostatic diamagnetic currents. The signature of diamagnetic currents is a 0.2 nT B_{y1} enhancement inside the density bubble consistent with the first-order approximation derived by *Lühr et al.* (2003). EMI simulations verify Lühr's approximation as well as the conclusion made by *Stolle et al.* (2006) attributing CHAMP-observed B_{y1} to diamagnetic currents around equatorial bubbles. The CHAMP satellite observations in Figure 1.3 exhibits similar anti-correlation between n_{i1} and B_{y1} as in Figure 8.3. As first suggested by *Stolle et al.* (2006), measuring B_{y1} is a viable method for detecting equatorial density bubbles (as long as the magnetometer has at least ~ 0.1 nT precision).

11.4 Three-dimensional ambipolar electric field versus one-dimensional theory

In Section 8.4, electrostatic ambipolar electric fields associated with a low-latitude bubble were simulated. The electromagnetic signature of the ambipolar current circulation is small compared to the signatures of other current systems discussed in this dissertation. However, it was found that 1-D theory greatly overestimate the 3-D ambipolar electric fields. The implications of this discrepancy is that care must be taken in interpreting ambipolar electric fields observed experimentally. Although it is relatively easy to calculate in 1-D, the ambipolar electric field is lower with three degrees of freedom than with only one degree of freedom. In the simulation presented in Figure 8.4, they differed by 20 times. To estimate the parallel density gradient from E_{y1}, one cannot rely on 1-D theory, despite its simplicity. In solving the 1-D ambipolar electric field equation (8.2) for the parallel density gradient, we could erroneously calculate the density gradient as $\nabla_{\parallel} n_e = -E_{y1}/en_e k_b T_e$. However, since 1-D theory overestimates 3-D ambipolar electric fields, 1-D theory only gives an upper bound ($\left|\nabla_{\parallel} n_e\right| \leq |E_{y1}/en_e k_b T_e|$), which is not very useful, considering that the gradient can be 20 times less than the upper bound.

In the context of simulating ionospheric physics, a consequence of 1-D overestimation of ambipolar electric fields is that there will be greater ambipolar diffusion and subsequently different plasma morphology. However, keep in mind that the discrepancy between 1-D and 3-D ambipolar electric fields likely decreases with increasing perpendicular scale lengths. Increasing scale lengths in any two dimensions eventually approaches a 1-D limit. What scale lengths 1-D ambipolar electric fields are valid is worth investigating in the future.

11.5 Tilted electromagnetic fields: evidence of the influence of winds

In Section 8.6, the effects of neutral winds on a low-latitude plasma bubble were simulated. Without winds, the Rayleigh-Taylor mode produces solely zonal polarization electric field. However, the inclusion of zonal winds added meridional polarization electric fields resulting in "tilted" electric field signature; that is, the electric field signature was tilted from the zonal direction. The prevalence of tilted electric field signatures observed in nature suggests the prevalence of the influence of winds on low-latitude plasma irregularities in nature. When modeling low-latitude plasma irregularities, one must consider the effects of winds.

11.6 Alfvén resonance

In Chapter 9, we explore Alfvén resonance in the context of low-latitudes plasma irregularities. Time delays associated with the time it takes Alfvén waves to travel along Earth's magnetic field lines can affect the magnitude of perturbation electric fields that develop with equatorial density bubbles when considering a background drift speed. For the simulations presented in Chapter 9, there was a resonance of electric fields when the ratio of a density wave's zonal wavelength to zonal drift is roughly 10 seconds (roughly equal to the timescale at which electrostatics for a stationary wave is approximately met). Thorough analysis of the Alfvén resonator at low-latitudes may be worth pursuing in future studies. Given zonal background drifts, resonant wavelengths would develop greater polarization electric field and thus grow faster than non-resonant wavelengths. As a result, background zonal drifts may select certain wavelengths of irregularities.

11.7 Supersonic bubble

In Chapter 10, we simulated a supersonic bubble, showing the dynamics of low-latitude equatorial bubbles. Initialized with a density bubble at the bottomside of the F layer, the simulation resulted

in a bubble that pierces the topside of the F region after 90 seconds. The signature of this supersonic bubble was a strong zonal electric field on the order of 10 mV/m, and strong negative and positive meridional magnetic fields on the northern and southern edge of the bubble, respectively, on the order of 100 nT. The observations made by *Aggson et al.* (1992) were consistent with the supersonic bubble simulated.

11.8 Thoughts about EMI computations

The simulations presented in this dissertation are hopefully the first of several EMI simulations to be used in exploring the dynamic and static electromagnetic properties of ionospheric plasmas. As shown, EMI is capable of simulating electrodynamics in 3-D. The code is efficient and parallelizable. Twenty virtual seconds took about a day to simulate on a four-core desktop computer. Recall that, in these simulations, we resolve Alfvénic speeds of up to 10^7 m/s. By the Courant condition (*Courant et al.*, 1967), we must take time steps shorter than the smallest cell wall length (kilometer scale) divided by the fastest speed in the simulation (10^7 m/s). Hence, we take extremely small time steps of 0.1 ms. To simulate one virtual hour requires 36 million iterations, which would take hundreds of years of computational time on a four-core desktop. Thus, it is not viable to simulate both Alfvénic dynamics and bubble growth simultaneously.

However, the time integration of electric and magnetic fields with Maxwell's equations may be a viable way to solve for electrostatic fields, which can be used to integrate bubble growth at much longer time steps. Traditionally, the spread-F problem solves for electrostatic fields by solving for the electric potentials that satisfy $\nabla \cdot \mathbf{J} = 0$ for every time iteration. Because the potential solution is elliptic, it is a challenge to parallelize. However, electromagnetic models such as PERSEUS (*Seyler and Martin*, 2011) and EMI do not directly solve any elliptic equations and are naturally parallelizable. The time integration of each cell point only requires information from neighboring cell points, making it easy to subdivide the simulation space and split the computation in parallel

fashion. Taking advantage of parallel computing makes electromagnetic code very efficient and time integration tractable. The plausibility of using EMI to efficiently simulate fully 3-D bubble growth may be worth exploring in the future.

Appendix A

Types of currents

Here, we derive the currents discussed in this dissertation and classify the different types of currents. First, the motion of ions and electrons can be expressed by the single species ion momentum, and electron momentum equations,

$$\frac{D\mathbf{v}_i}{Dt} = \frac{e}{M}\left(\mathbf{E} + \mathbf{v}_i \times \mathbf{B}\right) + \mathbf{g} - \frac{\nabla p_i}{n_i M} - \nu_{in}\left(\mathbf{v}_i - \mathbf{v}_n\right) - \nu_{ie}\left(\mathbf{v}_i - \mathbf{v}_e\right) \tag{A.1}$$

$$\frac{D\mathbf{v}_e}{Dt} = -\frac{e}{m}\left(\mathbf{E} + \mathbf{v}_e \times \mathbf{B}\right) + \mathbf{g} - \frac{\nabla p_e}{n_e m} - \nu_{en}\left(\mathbf{v}_e - \mathbf{v}_n\right) - \nu_{ei}\left(\mathbf{v}_e - \mathbf{v}_i\right), \tag{A.2}$$

where $\mathbf{v}_i$ is the ion velocity, $\mathbf{v}_e$ is the electron velocity, D/Dt is the advective derivative ($\partial_t + \mathbf{v}_i \cdot \nabla$ for ions and $\partial_t + \mathbf{v}_e \cdot \nabla$ for electrons where ∂_t is the partial time-derivative), e is the electron charge, M is the ion mass, m is the electron mass, $\mathbf{E}$ is the electric field vector, $\mathbf{B}$ is the magnetic field vector, $\mathbf{g}$ is the gravity acceleration vector, p_i is the ion pressure, p_e is the electron pressure, ν_{ie} is the ion-electron collision frequency, ν_{in} is the ion-neutral collision frequency, ν_{ei} is the electron-ion collision frequency, and ν_{en} is the electron-neutral collision frequency. Throughout this dissertation, we deal only with singly charged ions (O^+, H^+, He^+, O_2^+, NO^+) with the implication that $n_i \simeq n_e$

for quasineutrality. Solving equations (A.1) for $\mathbf{v}_i$ and (A.2) for $\mathbf{v}_e$ yields

$$\mathbf{v}_i = \tilde{\mathbf{A}}_i \cdot \left[\frac{e}{M}\mathbf{E} + \mathbf{g} - \frac{\nabla p_i}{n_i M} + \nu_{in}\mathbf{v}_n + \nu_{ie}\mathbf{v}_e - \frac{D\mathbf{v}_i}{Dt} \right] \tag{A.3}$$

$$\mathbf{v}_e = \tilde{\mathbf{A}}_e \cdot \left[-\frac{e}{m}\mathbf{E} + \mathbf{g} - \frac{\nabla p_e}{n_e m} + \nu_{en}\mathbf{v}_n + \nu_{ei}\mathbf{v}_i - \frac{D\mathbf{v}_e}{Dt} \right], \tag{A.4}$$

where $\tilde{\mathbf{A}}_i$ and $\tilde{\mathbf{A}}_e$ are tensors, defined as

$$\tilde{\mathbf{A}}_{(\sigma=i,e)} = \begin{bmatrix} \nu_\sigma & -\Omega_{\sigma z} & \Omega_{\sigma y} \\ \Omega_{\sigma z} & \nu_\sigma & -\Omega_{\sigma x} \\ -\Omega_{\sigma y} & \Omega_{\sigma x} & \nu_\sigma \end{bmatrix}^{-1}, \tag{A.5}$$

where $\nu_i = \nu_{in} + \nu_{ie}$, $\nu_e = \nu_{en} + \nu_{ei}$, and gyrofrequency components are defined as

$$\begin{bmatrix} \Omega_{ix} \\ \Omega_{iy} \\ \Omega_{iz} \end{bmatrix} \equiv \frac{e\mathbf{B}}{M}, \begin{bmatrix} \Omega_{ex} \\ \Omega_{ey} \\ \Omega_{ez} \end{bmatrix} \equiv -\frac{e\mathbf{B}}{m}. \tag{A.6}$$

$\mathbf{J}$ is the current density defined as

$$\mathbf{J} = en_e(\mathbf{v}_i - \mathbf{v}_e). \tag{A.7}$$

Substituting equations (A.3) and (A.4) into (A.7) yields

$$\begin{aligned} \mathbf{J} = {} & en_e\tilde{\mathbf{A}}_i \left(\frac{e}{M}\mathbf{E} + \mathbf{g} - \frac{\nabla p_i}{n_i M} + \nu_{in}\mathbf{v}_n + \nu_{ie}\mathbf{v}_e - \frac{D\mathbf{v}_i}{Dt} \right) \\ & - en_e\tilde{\mathbf{A}}_e \left(-\frac{e}{m}\mathbf{E} + \mathbf{g} - \frac{\nabla p_e}{n_e m} + \nu_{en}\mathbf{v}_n + \nu_{ei}\mathbf{v}_i - \frac{D\mathbf{v}_e}{Dt} \right) \end{aligned} \tag{A.8}$$

We classify five different contributions to the current density, $\mathbf{J}$, by the forces that drive each classification. This appendix overviews currents driven by static electric field, gravity-driven currents, pressure-driven currents, currents driven by neutral winds, and polarization currents.

A.1 Static electric field currents

Currents driven by static electric fields ($\mathbf{E}$) can expressed as

$$\mathbf{J}_E = en_e\tilde{\mathbf{A}}_i\left(\frac{e}{M}\mathbf{E}\right) - en_e\tilde{\mathbf{A}}_e\left(-\frac{e}{m}\mathbf{E}\right). \tag{A.9}$$

However, it is convenient to express currents driven by static electric fields by defining a conductivity tensor $\tilde{\boldsymbol{\sigma}} = en_e\left(\tilde{\mathbf{A}}_i e/M + \tilde{\mathbf{A}}_e e/M\right)$ so that we can express $\mathbf{J}_E$ simply as

$$\mathbf{J}_E = \tilde{\boldsymbol{\sigma}}\mathbf{E}, \tag{A.10}$$

where

$$\begin{aligned}
\tilde{\boldsymbol{\sigma}} &= \begin{bmatrix} \sigma_p & 0 & \sigma_h \\ 0 & \sigma_0 & 0 \\ -\sigma_h & 0 & \sigma_p \end{bmatrix} \\
\sigma_0 &= e^2 n_e\left(\frac{1}{m\nu_e} + \frac{1}{M\nu_i}\right) \\
\sigma_p &= e^2 n_e\left(\frac{\nu_e}{m\left(\nu_e^2+\Omega_e^2\right)} + \frac{\nu_i}{M\left(\nu_i^2+\Omega_i^2\right)}\right) \\
\sigma_h &= e^2 n_e\left(\frac{|\Omega_e|}{m\left(\nu_e^2+\Omega_e^2\right)} - \frac{\Omega_i}{M\left(\nu_i^2+\Omega_i^2\right)}\right),
\end{aligned} \tag{A.11}$$

for a coordinate system where $\hat{\mathbf{y}}$ is parallel to $\mathbf{B}$. The conductivities σ_0, σ_p and σ_h are commonly referred to as the parallel, Pedersen, and Hall conductivities, respectively.

A.2 Gravity-driven currents

Gravity-driven currents are defined as

$$\mathbf{J}_{gravity} = en_e\tilde{\mathbf{A}}_i\mathbf{g} - en_e\tilde{\mathbf{A}}_e\mathbf{g}. \tag{A.12}$$

In weakly collisional plasmas ($\Omega_i^2 \gg \nu_i^2$ and $\Omega_e \gg \nu_e$) the expression for gravity-driven currents can be reduced to

$$\mathbf{J}_{gravity} = \frac{(M+m)\, n_e}{B^2}\mathbf{g} \times \mathbf{B} \simeq \frac{M n_e}{B^2}\mathbf{g} \times \mathbf{B}, \tag{A.13}$$

where the approximation is made considering that $M \gg m$.

A.3 Pressure-driven currents

Pressure-driven currents are defined as

$$\mathbf{J}_{pressure} = e n_e \tilde{\mathbf{A}}_i \left(-\frac{\nabla p_i}{n_i M}\right) - e n_e \tilde{\mathbf{A}}_e \left(-\frac{\nabla p_e}{n_e m}\right). \tag{A.14}$$

In weakly collisional plasmas ($\Omega_i^2 \gg \nu_i^2$ and $\Omega_e \gg \nu_e$) the expression for pressure-driven perpendicular to $\mathbf{B}$ can be reduced to

$$\mathbf{J}_{\perp pressure} = \frac{-\left(\nabla p_i + \nabla p_e\right) \times \mathbf{B}}{B^2}. \tag{A.15}$$

A.4 Wind-driven currents

Wind-driven currents are defined as

$$\mathbf{J}_{wind} = e n_e \tilde{\mathbf{A}}_i \left(\nu_{in}\mathbf{v}_n\right) - e n_e \tilde{\mathbf{A}}_e \left(\nu_{en}\mathbf{v}_n\right) \backsimeq e n_e \tilde{\mathbf{A}}_i \left(\nu_{in}\mathbf{v}_n\right), \tag{A.16}$$

where the currents are driven by neutral winds colliding with ion and electrons. Note that the electron-neutral collision rate is negligible and $\Omega_e \gg \nu_e$. Hence, $\mathbf{J}_{wind}$ is primarily driven by ion-neutral interaction. In weakly collisional plasma ($\Omega_i^2 \gg \nu_i^2$ and $\Omega_e \gg \nu_e$) the expression for polarization can be reduced to

$$\mathbf{J}_{wind} = \frac{M n_e}{B^2}\left(\nu_{in}\mathbf{v}_n\right) \times \mathbf{B}. \tag{A.17}$$

A.5 Polarization currents

Polarization currents are currents resulting from ion inertia perpendicular to $\mathbf{B}$, $\partial_t \mathbf{v}_{i\perp}$. We derive an expression for polarization currents by first taking the zero order ion velocity as equation (3.9) without ion inertia:

$$\overline{\mathbf{v}}_i = \tilde{\mathbf{A}}_i \left(\frac{e\mathbf{E}}{M} + \mathbf{g} - \frac{\nabla p_i}{n_i M} + \nu_{ie}\mathbf{v}_e + \nu_{in}\mathbf{v}_n \right). \tag{A.18}$$

Making the first-order approximation that $\partial_t \mathbf{v}_{i\perp} \approx \partial_t \overline{\mathbf{v}}_{i\perp}$, we approximate ion inertia by taking the derivative of equation (A.18), which results in

$$\partial_t \mathbf{v}_{i\perp} \approx \tilde{\mathbf{A}}_i \cdot \frac{e}{M} \left(\partial_t \mathbf{E}_\perp \right), \tag{A.19}$$

where we assume gravity, pressure gradients, and collisional terms to be effectively constant ($\partial_t \simeq 0$) compared to the electrodynamics. Subsequently, the polarization current, $\mathbf{J}_{polarization}$, can be expressed as

$$\mathbf{J}_{polarization} = e n_e \tilde{\mathbf{A}}_i \left(-\partial_t \mathbf{v}_{i\perp} \right) = -\frac{e^2 n_e}{M} \tilde{\mathbf{A}}_i^2 \cdot \left(\partial_t \mathbf{E}_\perp \right), \tag{A.20}$$

where we substitute $\partial_t \mathbf{v}_{i\perp}$ with equation (A.19). For weakly collisional plasma ($\Omega_i^2 \gg \nu_i^2$ and $\Omega_e \gg \nu_e$) the polarization current can be expressed as

$$\mathbf{J}_{polarization} = \frac{M n_e}{B^2} \partial_t \mathbf{E}_\perp. \tag{A.21}$$

Appendix B

Electric field mapping for equipotential magnetic dipole field lines

While magnetic field lines are approximately equipotential, the distance between field lines does vary. Approximating the Earth's magnetic field as a dipole magnetic field, $r = R_0 \cos^2\theta$ where r is the distance from the center of the Earth, R_0 is the r of the field line at the magnetic equator, and θ is the magnetic latitude. The zonal (x direction) electric field along a field line can be formulated as

$$\begin{aligned} E_x &= -\frac{d\Phi}{dx} = -\frac{d\Phi}{r\cos\theta d\lambda}, \\ E_x &= -\frac{d\Phi}{R_0\cos^3\theta d\lambda}, \\ E_x &= \frac{1}{\cos^3\theta} \cdot E_x|_{\theta=0}, \end{aligned} \tag{B.1}$$

where Φ is the potential, λ is magnetic longitude, and $E_x|_{\theta=0}$ is the zonal electric field at the equator. Using the magnetic dipole identity, $\sin D = dz/\left(r \cdot d\theta\right)$, the derivative of R_0 with respect to magnetic latitude $dR_0/d\theta = 2r\sin\theta/\cos^3\theta$, and the dipole relationship $sinD = 2\sin\theta/\sqrt{1+3\sin^2\theta}$ where D is the angle between the Earth's magnetic field and the horizon, the meridional (z-direction)

electric field along a field line is formulated as

$$
\begin{aligned}
E_z &= -\frac{d\Phi}{dz} = -\frac{d\Phi}{r \cdot d\theta \sin D}, \\
E_z &= -d\Phi \frac{1}{r} \frac{2r \sin\theta}{dR_0 \cos^3\theta} \frac{\sqrt{1+3\sin^2\theta}}{2\sin\theta}, \\
E_z &= \frac{-d\Phi}{dR_0} \frac{\sqrt{1+3\sin^2\theta}}{\cos^3\theta}, \\
E_z &= \frac{\sqrt{1+3\sin^2\theta}}{\cos^3\theta} \cdot E_z|_{\theta=0},
\end{aligned}
\tag{B.2}
$$

where $E_z|_{\theta=0}$ is the meridional electric field at the equator. Both (B.1) and (B.2) are equivalent to expressions in *Mozer* (1970), generalized for an arbitrary point on a field line instead of strictly where the field lines intersect the Earth's surface.

Appendix C

Alfvén wave reflections off a change in Alfvén speeds

When a propagating Alfvén wave encounters a change in Alfvén speed, a reflection results. Let us consider an Alfvén wave propagating in a medium with $V_a = c_1$ and encountering a medium with $V_a = c_2$ as illustrated in Figure C.1. This problem is described by an initial wave incident to the boundary that splits into a reflected wave and transmitted wave.

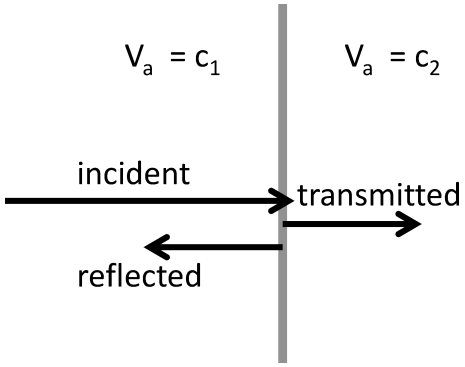

Figure C.1: Diagram of an incident wave interacting with a change in Alfvén speed.

By Faraday's law,

$$\frac{E}{B} = \frac{\omega}{k}, \tag{C.1}$$

where ω is the wave frequency, k is the wave-number, and ω/k is the wave phase speed. Here, we pick a coordinate system where the x-dimension is parallel to $\mathbf{E}_1$, the y-dimension is parallel to $\mathbf{B}_1$, and the z-dimension is parallel to the direction of the wave propagation. For Alfvén waves, ω/k is equal to the Alfvén speed. Hence, we can express the E/B for the incident, reflected, and transmitted waves as

$$\frac{E_{incident}}{B_{incident}} = c_1 \tag{C.2}$$

$$\frac{E_{reflected}}{B_{reflected}} = -c_1 \tag{C.3}$$

$$\frac{E_{transmitted}}{B_{transmitted}} = c_2, \tag{C.4}$$

respectively. Here the incident, reflected, and transmitted components of E and B are denoted in the subscript. Because of the continuity of B at the boundary,

$$B_{incident} + B_{reflected} = B_{transmitted}. \tag{C.5}$$

Substituting the B components with equations (C.2), (C.3), and (C.4) yields

$$\frac{E_{incident} - E_{reflected}}{c_1} = \frac{E_{transmitted}}{c_2}. \tag{C.6}$$

In order to maintain the continuity of E at the boundary, $E_{transmitted} = E_{incident} + E_{reflected}$, thus

$$\frac{E_{incident} - E_{reflected}}{c_1} = \frac{E_{incident} + E_{reflected}}{c_2}, \tag{C.7}$$

which can be rearranged as

$$E_{reflected} = \frac{c_2 - c_1}{c_2 + c_1} \cdot E_{incident}. \tag{C.8}$$

Equation (C.8) describes the E of reflected wave relative to the incident E. For $c_1 < c_2$, the reflected wave is a positive reflection; that is, the E of the reflected wave has the same sign as the incident wave. For $c_1 > c_2$, the reflected wave is a negative reflection; that is, the E of the reflected wave has the opposite sign as the incident wave.

Bibliography

Aggson, T. L., W. J. Burke, N. C. Maynard, W. B. Hanson, P. C. Anderson, J. A. Slavin, W. R. Hoegy, and J. L. Saba (1992), Equatorial bubbles updrafting at supersonic speeds, *J. Geophys. Res.*, *97*(A6), 8581–8590, doi:10.1029/92JA00644.

Alexander, R. (1977), Diagonally implicit runge-kutta methods for stiff ode's, *SIAM Journal on Numerical Analysis*, *14*(6), 1006–1021.

Ascher, U. M., S. J. Ruuth, and R. J. Spiteri (1997), Implicit-explicit runge-kutta methods for time-dependent partial differential equations, *Applied Numerical Mathematics*, *25*(2), 151–167.

Atkinson, G. (1970), Auroral arcs: Result of the interaction of a dynamic magnetosphere with the ionosphere, *Journal of Geophysical Research*, *75*(25), 4746–4755.

Aveiro, H. C., and D. L. Hysell (2010), Three-dimensional numerical simulation of equatorial F region plasma irregularities with bottomside shear flow, *J. Geophys. Res.*, *115*, A11321, doi: 10.1029/2010JA015602.

Aveiro, H. C., and D. L. Hysell (2012), Implications of the equipotential field line approximation for equatorial spread F analysis, *Geophys. Res. Lett.*, *39*, L11106, doi:10.1029/2012GL051971.

Balsley, B. B., G. Haerendel, and R. A. Greenwald (1972), Equatorial spread f: Recent observations and a new interpretation, *Journal of Geophysical Research*, *77*(28), 5625–5628, doi: 10.1029/JA077i028p05625.

Basu, B. (2005), Characteristics of electromagnetic Rayleigh-Taylor modes in nighttime equatorial plasma, *J. Geophys. Res.*, *110*, A02303, doi:10.1029/2004JA010659.

Berger, M., M. Aftosmis, and S. Murman (2005), Analysis of slope limiters on irregular grids, *AIAA paper*, *490*, 2005.

Bhattacharyya, A., and W. J. Burke (2000), A transmission line analogy for the development of equatorial ionospheric bubbles, *J. Geophys. Res.*, *105*, 24,941–24,950, doi:10.1029/1999JA000458.

Bilitza, D., and B. W. Reinisch (2008), International Reference Ionosphere 2007: Improvements and new parameters, *Adv. Space Res.*, *42*, 599–609, doi:10.1016/j.asr.2007.07.048.

Burke, W. J., L. C. Gentile, S. R. Shomo, P. A. Roddy, and R. F. Pfaff (2012), Images of bottomside irregularities observed at topside altitudes, *J. Geophys. Res.*, *117*, A03332, doi: 10.1029/2011JA017169.

Butcher, J. C. (1987), *The numerical analysis of ordinary differential equations: Runge-Kutta and general linear methods*, Wiley-Interscience, New York, NY, USA.

Cosgrove, R., and R. Doe (2010), Effect of ionospheric depth on the ionospheric feedback instability: cutoff and subsequent $e_{||}$ modes, *Annales Geophysicae*, *28*(9), 1777–1794, doi: 10.5194/angeo-28-1777-2010.

Courant, R., K. Friedrichs, and H. Lewy (1967), On the partial difference equations of mathematical physics, *IBM J. Res. Dev.*, *11*(2), 215–234.

Crouzeix, M. (1976), Sur les methodes de runge kutta pour l'approximation des problemes d'evolution, in *Computing Methods in Applied Sciences and Engineering*, *Lecture Notes in Economics and Mathematical Systems*, vol. 134, edited by R. Glowinski and J. Lions, pp. 206–223, Springer Berlin Heidelberg.

Dao, E., M. C. Kelley, P. Roddy, J. Retterer, J. O. Ballenthin, O. de La Beaujardiere, and Y.-J. Su (2011), Longitudinal and seasonal dependence of nighttime equatorial plasma density irregularities during solar minimum detected on the C/NOFS satellite, *Geophys. Res. Lett.*, *38*, L10104, doi: 10.1029/2011GL047046.

Dao, E., M. C. Kelley, D. L. Hysell, J. M. Retterer, Y.-J. Su, R. F. Pfaff, P. A. Roddy, and J. O. Ballenthin (2012), On the distribution of ion density depletion along magnetic field lines as deduced using C/NOFS, *Radio Sci.*, *47*, RS3001, doi:10.1029/2011RS004967.

de La Beaujardiere, O., et al. (2004), C/NOFS: A mission to forecast scintillations, *J. Atmos. Solar-Terr. Phys.*, *66*, 1573–1591, doi:10.1016/j.jastp.2004.07.030.

Dungey, J. (1956), Convective diffusion in the equatorial F region, *J. Atmos. Terr. Phys.*, *9*, 304–310, doi:http://dx.doi.org/10.1016/0021-9169(56)90148-9.

Farley, D. T. (1960), A theory of electrostatic fields in the ionosphere at nonpolar geomagnetic latitudes, *Journal of Geophysical Research*, *65*(3), 869–877, doi:10.1029/JZ065i003p00869.

Feshbach, H. (1953), Methods of theoretical physics.

Haerendel, G. (1973), Theory of equatorial spread F, Max-Planck Inst. für Phys. und Astrophys., Garching, Germany.

Hanson, W. B., and S. Sanatani (1973), Large ni gradients below the equatorial f peak, *J. Geophys. Res.*, *78*(7), 1167–1173, doi:10.1029/JA078i007p01167.

Huang, C.-S., O. de La Beaujardiere, R. F. Pfaff, J. M. Retterer, P. A. Roddy, D. E. Hunton, Y.-J. Su, S.-Y. Su, and F. J. Rich (2010), Zonal drift of plasma particles inside equatorial plasma bubbles and its relation to the zonal drift of the bubble structure, *J. Geophys. Res.*, *115*(A7), n/a–n/a, doi:10.1029/2010JA015324.

Huba, J. D., G. Joyce, and J. A. Fedder (2000), Sami2 is Another Model of the Ionosphere (SAMI2): A new low-latitude ionosphere model, *J. Geophys. Res.*, *105*, 23,035–23,054, doi: 10.1029/2000JA000035.

Huba, J. D., G. Joyce, and J. Krall (2008), Three-dimensional equatorial spread F modeling, *Geophys. Res. Lett.*, *35*, L10102, doi:10.1029/2008GL033509.

Jin, S., and Z. Xin (1995), The relaxation schemes for systems of conservation laws in arbitrary space dimensions, *Comm. Pure Appl. Math*, *48*, 235–277.

Kelley, M. C. (2009), *The Earth's Ionosphere: Plasma Physics and Electrodynamics*, vol. 96, second ed., Academic Press, Burlington, MA.

Krall, J., J. D. Huba, S. L. Ossakow, G. Joyce, J. J. Makela, E. S. Miller, and M. C. Kelley (2011), Modeling of equatorial plasma bubbles triggered by non-equatorial traveling ionospheric disturbances, *Geophys. Res. Lett.*, *38*, L08103, doi:10.1029/2011GL046890.

LeVeque, R. J. (1998), *Nonlinear conservation laws and finite volume methods for astrophysical fluid flow.*

Lühr, H., M. Rother, S. Maus, W. Mai, and D. Cooke (2003), The diamagnetic effect of the equatorial Appleton anomaly: Its characteristics and impact on geomagnetic field modeling, *Geophys. Res. Lett.*, *30*(17), 1906, doi:10.1029/2003GL017407.

Lysak, R. L. (1986), Coupling of the dynamic ionosphere to auroral flux tubes, *Journal of Geophysical Research*, *91*(A6), 7047–7056.

Lysak, R. L. (1991), Feedback instability of the ionospheric resonant cavity, *Journal of Geophysical Research: Space Physics (1978–2012)*, *96*(A2), 1553–1568.

McClure, J. P., W. B. Hanson, and J. H. Hoffman (1977), Plasma bubbles and irregularities in the equatorial ionosphere, *J. Geophys. Res.*, *82*(19), 2650–2656, doi:10.1029/JA082i019p02650.

Mozer, F. (1970), Electric field mapping in the ionosphere at the equatorial plane, *Planetary and Space Science*, *18*(2), 259–263.

Norsett, S. (1974), One-step methods of hermite type for numerical integration of stiff systems, *BIT Numerical Mathematics*, *14*, 63–77, doi:10.1007/BF01933119.

Orens, J. H., T. R. Young, Jr., E. S. Oran, and T. P. Coffey (1979), Vector operations in a dipole coordinate system, *Tech. rep.*

Pareschi, L., and G. Russo (2000), Implicit-Explicit Runge-Kutta schemes and applications to hyperbolic systems with relaxation, *J. Sci. Comp.*, *3*, 269–287.

Perkins, F. (1973), Spread F and Ionospheric Currents, *J. Geophys. Res.*, *78*, 218–226, doi:10.1029/JA078i001p00218.

Picone, J. M., A. E. Hedin, D. P. Drob, and A. C. Aikin (2002), NRLMSISE-00 empirical model of the atmosphere: Statistical comparisons and scientific issues, *J. Geophys. Res.*, *107*(A12), 1468, doi:10.1029/2002JA009430.

Press, W. H., S. A. Teukolsky, W. T. Vetterling, and B. P. Flannery (2007), *Numerical Recipes 3rd Edition: The Art of Scientific Computing*, 3 ed., Cambridge University Press, New York, NY, USA.

Rappaport, H. L. (1996), Field line integration and localized modes in the equatorial spread f, *Journal of Geophysical Research: Space Physics*, *101*(A11), 24,545–24,551, doi:10.1029/96JA02174.

Reigber, C., H. Lühr, and P. Schwintzer (2002), CHAMP mission status, *Adv. Space Res.*, *30*(2), 129–134, doi:10.1016/S0273-1177(02)00276-4.

Retterer, J. M. (2005), Physics-based forecasts of equatorial radio scintillation for the Communication and Navigation Outage Forecasting System (C/NOFS), *Space Weather*, *3*, S12C03, doi:10.1029/2005SW000146.

Retterer, J. M. (2010), Forecasting low-latitude radio scintillation with 3-D ionospheric plume models: 1. Plume model, *J. Geophys. Res.*, *115*, A03306, doi:10.1029/2008JA013839.

Rishbeth, H. (1971), Polarization fields produced by winds in the equatorial F-region, *Planetary and Space Science*, *19*(3), 357–369.

Rodrigues, F. S., M. C. Kelley, P. A. Roddy, D. E. Hunton, R. F. Pfaff, O. de La Beaujardière, and G. S. Bust (2009), C/NOFS observations of intermediate and transitional scale-size equatorial spread F irregularities, *Geophys. Res. Lett.*, *36*, 0, doi:10.1029/2009GL038905.

Schunk, R. W., and A. F. Nagy (2004), *Ionospheres: Physics, Plasma Physics, and Chemistry*, Cambridge University Press, Cambridge, MA.

Seyler, C. E. (1990), A mathematical model of the structure and evolution of small-scale discrete auroral arcs, *J. Geophys. Res.*, *95*, 17,199–17,215, doi:10.1029/JA095iA10p17199.

Seyler, C. E., and M. R. Martin (2011), Relaxation model for extended magnetohydrodynamics: Comparison to magnetohydrodynamics for dense Z-pinches, *Phys. Plasmas*, *18*(1), 012,703, doi:10.1063/1.3543799.

Stolle, C., H. Lühr, M. Rother, and G. Balasis (2006), Magnetic signatures of equatorial spread F as observed by the CHAMP satellite, *J. Geophys. Res.*, *111*, A02304, doi:10.1029/2005JA011184.

Strang, G. (1968), On the construction and comparison of difference schemes, *SIAM J. Num. Anal.*, *5*(3), 506–517.

Sultan, P. J. (1996), Linear theory and modeling of the Rayleigh-Taylor instability leading to the occurrence of equatorial spread F, *J. Geophys. Res.*, *101*, 26,875–26,892, doi:10.1029/96JA00682.

Toth, G. (2000), The div b=0 constraint in shock-capturing magnetohydrodynamics codes, *J. Comp. Phys.*, *161*, 605–652, doi:10.1006/jcph.2000.6519.

Trac, H., and U.-L. Pen (2002), A primer on eulerian computational fluid dynamics for astrophysics, *Publ. Astron. Soc. Pac.*, *115*(805), 303–321, doi:10.1086/367747.

Trakhtengertz, V. Y., and A. Y. Feldstein (1984), Quiet auroral arcs: Ionosphere effect of magnetospheric convection stratification, *Planetary and space science*, *32*(2), 127–134.

Tsunoda, R. T., R. C. Livingston, J. P. McClure, and W. B. Hanson (1982), Equatorial plasma bubbles - Vertically elongated wedges from the bottomside F layer, *J. Geophys. Res.*, *87*, 9171–9180, doi:10.1029/JA087iA11p09171.

Van Leer, B. (1974), Towards the ultimate conservative difference scheme. ii. monotonicity and conservation combined in a second-order scheme, *J. Comput. Phys.*, *14*(4), 361–370.

Van Leer, B. (1979), Towards the ultimate conservative difference scheme. v. a second-order sequel to godunov's method, *J. Comput. Phys.*, *32*(1), 101–136.

Yokoyama, T., R. F. Pfaff, P. A. Roddy, M. Yamamoto, and Y. Otsuka (2011), On postmidnight low-latitude ionospheric irregularities during solar minimum: 2. c/nofs observations and comparisons with the equatorial atmosphere radar, *J. Geophys. Res.*, *116*(A11), doi:10.1029/2011JA016798.

Zargham, S. (1988), Numerical simulations of the ionospheric interchange instability., Ph.D. thesis.